



Article

Comprehension of the Synergistic Effect between m&t-BiVO₄/TiO₂-NTAs Nano-Heterostructures and Oxygen Vacancy for Elevated Charge Transfer and Enhanced Photoelectrochemical Performances

Zhufeng Shao ^{1,*} , Jianyong Cheng ¹, Yonglong Zhang ¹, Yajing Peng ¹, Libin Shi ¹ and Min Zhong ²¹ College of Physical Science and Technology, Bohai University, Jinzhou 121000, China² College of Chemistry and Materials Engineering, Bohai University, Jinzhou 121000, China

* Correspondence: jinhaiyuan@126.com

Abstract: Through the utilization of a facile procedure combined with anodization and hydrothermal synthesis, highly ordered alignment TiO₂ nanotube arrays (TiO₂-NTAs) were decorated with BiVO₄ with distinctive crystallization phases of monoclinic scheelite (m-BiVO₄) and tetragonal zircon (t-BiVO₄), favorably constructing different molar ratios and concentrations of oxygen vacancies (V_o) for m&t-BiVO₄/TiO₂-NTAs heterostructured nanohybrids. Simultaneously, the m&t-BiVO₄/TiO₂-NTAs nanocomposites significantly promoted photoelectrochemical (PEC) activity, tested under UV-visible light irradiation, through photocurrent density testing and electrochemical impedance spectra, which were derived from the positive synergistic effect between nanohetero-interfaces and V_o defects induced energetic charge transfer (CT). In addition, a proposed self-consistent interfacial CT mechanism and a convincing quantitative dynamic process (i.e., rate constant of CT) for m&t-BiVO₄/TiO₂-NTAs nanoheterojunctions are supported by time-resolved photoluminescence and nanosecond time-resolved transient photoluminescence spectra, respectively. Based on the scheme, the m&t-BiVO₄/TiO₂-NTAs-10 nanohybrids exhibited a photodegradation rate of 97% toward degradation of methyl orange irradiated by UV-visible light, 1.14- and 1.04-fold that of m&t-BiVO₄/TiO₂-NTAs-5 and m&t-BiVO₄/TiO₂-NTAs-20, respectively. Furthermore, the m&t-BiVO₄/TiO₂-NTAs-10 nanohybrids showed excellent PEC biosensing performance with a detection limit of 2.6 μM and a sensitivity of 960 mA cm⁻² M⁻¹ for the detection of glutathione. Additionally, the gas-sensing performance of m&t-BiVO₄/TiO₂-NTAs-10 is distinctly superior to that of m&t-BiVO₄/TiO₂-NTAs-5 and m&t-BiVO₄/TiO₂-NTAs-20 in terms of sensitivity and response speed.



Citation: Shao, Z.; Cheng, J.; Zhang, Y.; Peng, Y.; Shi, L.; Zhong, M. Comprehension of the Synergistic Effect between m&t-BiVO₄/TiO₂-NTAs Nano-Heterostructures and Oxygen Vacancy for Elevated Charge Transfer and Enhanced Photoelectrochemical Performances. *Nanomaterials* **2022**, *12*, 4042. <https://doi.org/10.3390/nano12224042>

Academic Editor: Cameron Shearer

Received: 15 October 2022

Accepted: 9 November 2022

Published: 17 November 2022

Publisher's Note: MDPI stays neutral with regard to jurisdictional claims in published maps and institutional affiliations.



Copyright: © 2022 by the authors. Licensee MDPI, Basel, Switzerland. This article is an open access article distributed under the terms and conditions of the Creative Commons Attribution (CC BY) license (<https://creativecommons.org/licenses/by/4.0/>).

Keywords: m&t-BiVO₄/TiO₂-NTAs nanoheterojunctions; oxygen vacancy defects; charge transfer; photodegradation; biosensing and gas-sensing application

1. Introduction

With the continuous development of globalization and the spread of infectious viruses (such as COVID-19) encroaching on human health, the sustainable utilization of energy and the protection of the natural environment have become issues of substantial concern worldwide. A promising avenue is photoelectrochemicals (PEC), which, due to the pioneering work of Fujishima and Honda, have received a great deal of attention for a variety of potential applications, including water-splitting hydrogen generation, rechargeable solar cells, photocatalytic fuel cells, organic pollutant photodegradation, and biosensing [1–3]. TiO₂ is credited as among the most promising and well-documented PEC materials, as it possesses an appropriate energy-band position towards the redox reaction of water splitting, has excellent chemical stability, is abundantly available, and is environmentally friendly. At present, powder suspensions and thin films are the two representative types of TiO₂-related photocatalysts [4]. Notably, powdered TiO₂-based PEC materials have been

adopted because they have a fully available surface area, lower requirements in terms of cleaning, and they can be conveniently manipulated [5]. Nevertheless, the practical application of TiO₂-related powdered photocatalysts is still under restrictions due to the poor PEC performance, low reusability, and low recyclability [6]. Compared with the PEC nanomaterials of particulates, thin-film TiO₂-related photocatalysts have gained more attention owing to the following reasons: (i) with valid and appropriate light absorption, abundant free electrons are generated; (ii) the thin-film form demonstrates maximum activity, with the activity up to an order of magnitude higher compared with the powder form; (iii) the operating cost and recycling reuse of thin-film-based panels are expected to be substantially lower compared with powder-like samples without mechanical stirring; (iv) more efficient electron transfer occurs in thin-film PEC nanosystems through the underlying conductive layer, and therefore, the thin-film system can substantially improve the PEC activity compared with powder suspension processes; (v) they are well suited to efficient large-scale applications [7,8]. Furthermore, the self-organized TiO₂ nanotube array films (NTAs) prepared by the Ti foil anodic oxidation process and vertically oriented on Ti-metal substrates are outstanding nanoscale thin-film architectures for boosting the PEC and biosensing performances [9,10]. TiO₂ NTAs with highly ordered nanoporous surfaces possess unique characteristics, which are summarized as follows: (i) an enhanced active adsorption area for redox target compounds [11]; (ii) ordered-array architectures, which not only enable charge transfer (CT) along the axial direction, but also enable the segregation of the photoexcited charge carriers [12]; (iii) band modification to improve the light absorption and reduce the charge recombination [13]. Although the profitable properties of TiO₂ NTAs are evident, the intrinsic features of TiO₂ remain, which mainly include the UV-activated wide band-gap energy ($E_g \sim 3.2$ eV), and the rapid charge recombination rate that results in a sluggish rate of charge separation [14], which inherently conflicts with the aim of PEC-related practical applications under visible-light irradiation. To circumvent the abovementioned obstacles, researchers have demonstrated that doping with metals (e.g., Au, Ag, and Cu) or nonmetals (e.g., C, N, and S) is a valid route for elevating the visible-light-harvesting capacity of TiO₂ NTAs [15]. Metallic elements, when deposited on TiO₂ NTAs, can induce a suitable band-gap shift and act as light gatherers, prolongating the wavelength absorption scope and enhancing the PEC activity in the visible-light region. Nevertheless, the method is hampered by several drawbacks, as noble-metal nanoparticles (NPs) are quite toxic in nature, the reaction setup is costly and cumbersome, and photocorrosion is inevitable during the PEC process. Likewise, using nonmetal ions instead of metals to dope TiO₂-NTAs photoanode materials is an alternative viable approach for exploring visible-light-active photocatalysts. Nonmetallic element doping could introduce mid-gap energy levels above the valence band (VB) of TiO₂ NTAs and act as a trapping center for the photoexcited electrons, which achieve the expected purposes for the photoresponse of the narrow band gap and suppress the recombination of photogenerated species. The decrease in the electronegativity of PEC materials that leads to a reduced PEC-related capacity due to the introduction of new energy states is an unavoidable issue [16]. Considering the trend of practical application, visible-light-active PEC nanosystems with striking CT abilities are more advantageous because a smaller percentage (5%) of the solar spectrum is emitted in the UV region. Within this frame, the construction of TiO₂-NTAs-based nano-heterojunctions not only substantially broadens the light-harvesting window, but it can also help increase the speed of the charge carrier separation.

Bismuth vanadate (BiVO₄) is an intrinsic n-type direct band-gap ternary oxide semiconductor, and it has been proposed as a promising alternative to visible-light-active PEC materials owing to its high stability, nontoxicity, and appropriate band position [17]. The PEC performances of BiVO₄ are intensely affected by the prepared morphology and crystallographic structure. BiVO₄ appears in three main crystalline phases based on different synthesized methods: monoclinic scheelite (ms-BiVO₄), tetragonal scheelite (ts-BiVO₄), and tetragonal zircon (tz-BiVO₄), with E_g values of 2.4 eV, 2.4 eV, and 2.9 eV [18,19], re-

spectively. Among them, state-of-the-art ms-BiVO₄ is the most stable and has the best photocatalytic activity, delivering a remarkable stability above 1000 h. The theoretical photocurrent density was 7.5 mA cm⁻² with a solar-to-hydrogen conversion efficiency of 9.2% under AM 1.5 G illumination [20], which is mainly attributed to the transition from the VB to the conduction band (CB) caused by the orbital mixing of Bi 6s and O 2p, which leads to the narrowed band gap and the sufficient oxidation potential of the VB (ca. +2.79 eV vs. NHE) to oxidize various organic compounds [21]. Moreover, ts-BiVO₄ has similar crystal and energy structures to those of ms-BiVO₄, which have rarely been studied, while the crystal phase of tz-BiVO₄ exhibits the lowest photocatalytic performance owing to its wide bandgap, which restricts the widespread photodegradation and water-splitting application in visible-light regions. Based on conclusive experiments [22], researchers have verified that an inferior carrier mobility (0.044 cm² V⁻¹ s⁻¹), short carrier diffusion length (~70 nm), and sluggish electron transfer kinetics are the intrinsic drawbacks of the pristine ms-BiVO₄, which result in unsatisfactory photocurrent densities. Moreover, Wang et al. [23] stressed that the reduction in the capability of electrons on the CB of pure ms-BiVO₄ (+0.04 eV vs. NHE) was weak, even though the holes on the VB of BiVO₄ possessed strong oxidation capability, which resulted in its inability to reduce the oxygen molecule (O₂) to a superoxide radical (O₂⁻, -0.33 eV vs. NHE) by trapping the electrons on the CB, as well as weak surface adsorption properties [24], which stemmed from the more negative O₂/O₂⁻ potential than the CB of ms-BiVO₄, and incurring a disappointing PEC conversion efficiency. In the single ms-BiVO₄ phototrigger system, the tradeoff between an adequate redox potential and the generation of plenty of energetic photoexcited carriers according to the bandgap limits improves the PEC performances. The redox reaction on a photoelectrode is an integral whole, and it only takes place when there is an excess of photogenerated e⁻ and h⁺ on the surface. Too many free movable phototriggered carriers accumulated on the surface of the semiconductor causes deficiency in the powerful in-built electric field for efficacious delivery, which is inevitably unfavorable for PEC reactions, and the carriers are more inclined to recombine in the interiors of photocatalysts. The construction of ms-BiVO₄/tz-BiVO₄ (m/t-BiVO₄) hetero-nanostructures is an alternative strategy to ameliorate the charge kinetics of ms-BiVO₄ alone, and in particular, to facilitate the charge separation, as researchers have recently demonstrated [25]. However, the m/t-BiVO₄ heterogeneous PEC materials are not only under harsh synthesis conditions, but they are also incapable of presenting an improvement in the energy-band-matching level to speed up the photoinduced charge segregation compared with ms-BiVO₄/TiO₂ and tz-BiVO₄/TiO₂ (m&t-BiVO₄/TiO₂) nano-heterostructures. Energy-band-matching m&t-BiVO₄/TiO₂-NTAs nano-heterojunctions with rich intrinsic oxygen vacancy (V_o) defects exhibit an impressive catalytic activity owing to the synergistic effect between the heterojunction interface effect and vacancy effect [26]. Furthermore, researchers have extensively unveiled the intrinsic correlation between the boosted PEC-related performances and the expedited CT dynamic process associated with the V_o in m&t-BiVO₄/TiO₂-NTAs nanocomplexes. The details of the contributions of the V_o defects are summarized as follows [23,27–29]: (I) V_o defects can function as electron donors that increase the majority carrier density and photovoltage; (II) V_o could provide shallow trapping sites to promote electron-hole (e⁻-h⁺) pair segregation and restrain the recombination of the charge carrier; (III) the electronic structure can be overlapped and delocalized by V_o defects, which leads to an enlarged light-absorption edge; (IV) the abundant surface V_o defects, which are positively charged, can serve as PEC reaction centers to adsorb adequate photodegradable active group species, including O₂⁻ and hydroxyl radicals (OH); (V) V_o sites contribute to the upward shift (more negative) in the Fermi level (E_F) and the CB of BiVO₄, and they can act as active sites to elevate the charge injection efficiency, benefitting from the favorable band-energy offset between the m&t-BiVO₄/TiO₂-NTAs nano-heterojunctions, which is instigated to enhance the frustrating reduction kinetics.

Contrasted with other preparation methods, hydrothermal synthesis is a preferable approach for the formation of nano-heteroarchitectures between the m&t-BiVO₄ and TiO₂

NTAs. Its suitability for large-scale industrial production is due to the simple process, environmental friendliness, and low cost [30]. The pH value of the precursor solution has a substantial impact on the molar ratios of the crystalline phase and the concentration of the surface defect states for *ms*-BiVO₄ and *tz*-BiVO₄ [25,31], which could also have a striking impact on the energy band position and the efficiency of the interfacial CT in the heterojunction. According to the relevant research, the timescale for the interfacial CT and recombination ultrafast kinetic process of *m&t*-BiVO₄/TiO₂-NTAs nano hybrids is of a nanosecond (ns) magnitude [32], involving the rate-determining step of the surface redox reactions and making it exceedingly challenging to comprehend. The timescale is much greater than the timescale of the photoexcited e⁻-h⁺ pair transition from VB to CB (viz., the femtosecond (fs) level) [33]. Simultaneously, it is possible to integrate the probing technique of an ultrafast fs laser triggered with time-resolved photoluminescence (PL) spectroscopy into an instrument that is capable of measuring transient PL on nanosecond timescales, providing the verifiable quantitative and qualitative information on the charge carrier dynamics for the intermediate states in nano-heterostructures associated with the V_o intrinsic defects, including the transient PL intensity of the time-dependent photoexcited carrier lifetime, and the rate constant of the CT [34,35], which plays a decisive role in improving the PEC-related performances. Logically, by utilizing the positive synergetic effects between *m&t*-BiVO₄ and TiO₂ NTAs, we can obtain an improved PEC efficiency and highly sensitive PEC aptasensor [36,37]. However, to the best of our knowledge, the qualitative interfacial CT mechanism and quantitative charge injection dynamic process associated with V_o defects by taking advantage of transient-PL kinetics probing have not been comprehensively explored. Moreover, the inherent physical connection between the pH values of the precursor solution, different crystalline-phase molar ratios, and number of V_o defects are rarely referred to.

First, we fabricated tidy and smooth TiO₂ NTAs with highly ordered alignment top surfaces through the anodization approach, facilitating easy access for the uniform deposition of *m&t*-BiVO₄ NPs via a convenient hydrothermal method, which we used to construct *m&t*-BiVO₄/TiO₂ NTA type-II heterostructure nano hybrids with different crystalline-phase molar ratios and the expected concentration of V_o defects. Moreover, the photoinduced carriers are dramatically separated and transferred at the interface between the *m&t*-BiVO₄ and TiO₂ NTAs, benefiting from the synergistic effects between the elevated band offset in staggered heterostructures and the increased exposed reaction active sites induced by the V_o defects, which are responsible for the boosted PEC-related performances. Additionally, we can use the unique combination of nanosecond-time-resolved transient PL (NTRT-PL) and time-resolved PL (TRPL) spectroscopy to independently track the charge carrier dynamics between the donor and acceptor energy levels, qualitative and quantitative extrapolating the CT process at the interfaces between the *m&t*-BiVO₄ and TiO₂ NTAs, which allows for the acquisition of the CT rate coefficient and charge carrier lifetime. Moreover, the established correlations between the PEC degradation performance, biosensing and gas-sensing sensitivity, and the crystalline structural feature of the *m&t*-BiVO₄/TiO₂ NTA nano-heterostructures provide insight into the expected interfacial energy band alignment related to the V_o defect concentration, which elevates the ultrafast injection of the free carriers from BiVO₄ into TiO₂ NTAs. Furthermore, the research highlights the importance and novelty of probing interfacial CT kinetic processes modulated by V_o surface defects for understanding the mechanisms of PEC conversion in *m&t*-BiVO₄/TiO₂-NTAs nanocomplexes. We hope that the investigation can provide practical experiences and in-depth comprehension for the design of PEC-related devices with substantially superior performances.

2. Experimental Section

2.1. Preparation of TiO₂-NTAs Substrates via Anodization

We bought all the reagents and solvents from commercial sources, and we used them without any further purification. We prepared the TiO₂ NTAs by anodizing Ti foils in an

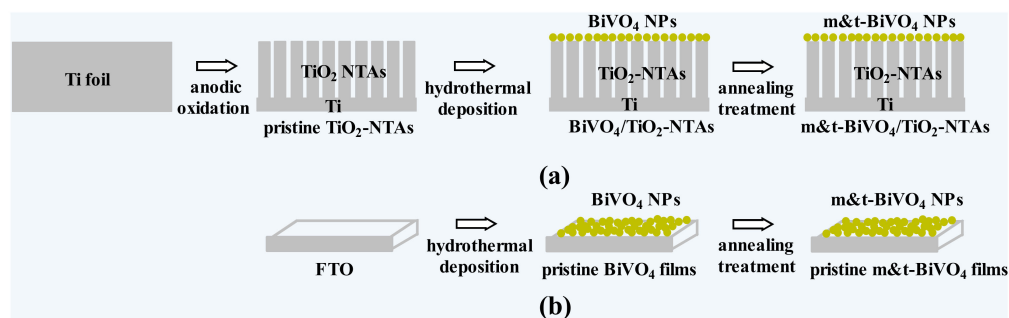
electrolyte containing NH_4F (0.45 wt.%) and ethanediol (98 vol.%). This process resulted in the formation of TiO_2 NTAs on the surface of the Ti foils, which researchers described in a previous report [35].

2.2. Fabrication of $m\&t\text{-BiVO}_4/\text{TiO}_2\text{-NTAs}$ Heterostructure Nanohybrids

The BiVO_4 NPs were deposited onto the surface of the fabricated TiO_2 NTAs via a facile low-temperature hydrothermal method. In brief, we sequentially dissolved a 2 mL concentration of 0.1 M of $\text{Bi}(\text{NO}_3)_3 \cdot 5\text{H}_2\text{O}$ and a 2 mL concentration of 0.1 M of NH_4VO_3 in 19 mL of ethylene glycol, and we then added a 1 mL concentration of 2.0 M of HNO_3 to form a precursor solution. Adding HNO_3 aqueous solution can help dissolve other reagents and render the resulting solution more acidic. We adjusted the mixture to a certain pH value (2, 5, or 8) by slowly adding ammonia with a magnetic stirrer to obtain different crystalline-phase molar ratios of $m\&t\text{-BiVO}_4$. We transferred the orange transparent precursor into a Teflon-lined stainless-steel autoclave (50 mL) after vigorous stirring for 30 min, and we maintained it at $100\text{ }^\circ\text{C}$ with different hydrothermal deposition times (5 h, 10 h, and 20 h). We vertically placed the preprepared highly ordered TiO_2 NTAs in the autoclave in advance through a home-built Teflon sample holder.

As a reference for characterizing the optical and PEC performances, we prepared the pristine BiVO_4 films by the hydrothermal route. Briefly, we methodically dissolved 0.2 mmol of $\text{Bi}(\text{NO}_3)_3 \cdot 5\text{H}_2\text{O}$, 0.2 mmol of NH_4VO_3 , and 1 mL of 2.0 M HNO_3 in 19 mL of ethylene glycol. We adjusted the pH value of the sample suspension to 5 with ammonia, and then vertically placed the prearranged clean FTO conductive glass substrate into the mixed solution and maintained it at $100\text{ }^\circ\text{C}$ for 10 h.

After we rinsed the as-prepared specimens with deionized water, we dried them with a nitrogen gas flow. For facilitating the generation of intrinsic defects and the expected crystalline phases, we annealed the as-obtained specimens in a furnace in dry air. The annealing temperature was $450\text{ }^\circ\text{C}$, and the time was 30 min. The heating rate was $10\text{ }^\circ\text{C}/\text{min}$, and the cooling rate was $10\text{ }^\circ\text{C}/\text{min}$. The choice of the annealing temperature was deliberate to avoid the transformation of the crystal structure of $t\text{-BiVO}_4$ into $m\text{-BiVO}_4$ during the annealing process (annealing temperature $> 500\text{ }^\circ\text{C}$) [38]. We present the details on the process of incorporating modified BiVO_4 NPs onto FTO and TiO_2 NTA surfaces with the same area size ($1\text{ cm} \times 1.5\text{ cm}$) in Scheme 1.



Scheme 1. Preparation process of $m\&t\text{-BiVO}_4/\text{TiO}_2\text{-NTAs}$ nanocomplex (a), and pristine BiVO_4 films (b).

2.3. Characterization

We characterized the microstructures of the as-prepared nano-heterostructures by scanning electron microscopy (SEM) (Hitachi S4200) and transmission electron microscopy (TEM) (JEOL JEM-2100). We performed the UV–visible diffuse reflectance spectrometry (UV–vis DRS) measurements using a UV–vis spectrophotometer (UV-1800, Shimadzu). We characterized the phase purity of the prepared specimens by an X-ray diffractometer (XRD) (Shimadzu XRD-600). We used micro-Raman spectroscopy to investigate the crystal structure and chemical bonding states of the nanocomposites, equipped with a confocal microscope with an Ar^+ laser operating at 532 nm (Horiba JY-HR800). We investigated

the oxidation states of the as-formed samples by X-ray photoelectron spectroscopy (XPS) (ESCALAB 250). We determined the instrument's resolution to be 1.0 eV from the Ag 3d_{5/2} peak's full width at half maximum. We calibrated the XPS energy scale by aligning the Ag 3d_{5/2} line on clean silver with the E_F, which we set at 368.3 eV. The XPS spectra energy axis shifted due to the specimen charging that takes place during X-ray irradiation. Consequently, we set the C1s binding energy line to 285.0 eV, which is the standard hydrocarbon energy used to reference the charging effect.

We used CHI660E equipment (Chenhua) to perform the PEC-related performance tests. We performed the transient photocurrent density curve (transient I–t curve) measurements via frontside illumination under AM 1.5G (SS150A, ZOLIX) at a constant applied potential of 0 V in a 0.1 M Na₂SO₄ solution. The 0.2 M Na₂SO₄ solution acted as the electrolyte for the electrochemical impedance spectra (EIS) analysis. We constructed Mott–Schottky plots at 1 kHz to examine the relationship between the voltage and capacitance in the 0.5 M Na₂SO₄ solution. We adopted the following equation for the NHE potentials: E_{NHE} = E_{Ag/AgCl} + 0.1976 V, where E_{Ag/AgCl} is the Ag/AgCl electrode.

We excited the NTRT-PL using a Ti:sapphire femtosecond (fs) laser system (Spectra-Physics). We present the schematic diagram of the experimental setup in Figure 1. We collected the data for the TRPL using a custom-built single-photon-counting system, and the excitation source wavelength was 375 nm. We dispersed the signals of the PL emission for Vo defects (λ_{em} = 2.9 eV) by means of a grating spectrometer, and we detected them by a high-speed photomultiplier tube conjunction with a single-photon-counting card.

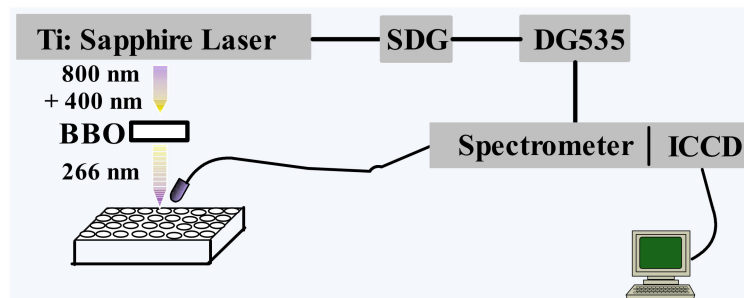


Figure 1. Schematic of experiment setup for NTRT-PL measurements.

2.4. Performance of MO Photodegradation, PEC Biosensing, and Gas-Sensing Measurements

We assessed the photocatalytic activities of the as-prepared nano-heterojunctions using the photodegradation of MO under UV–visible light irradiation. We used the UV–vis spectrophotometer to assess the concentration of the MO solution (10 mg/L) every 20 min. We monitored the intensity change in the characteristic absorption peak at 465 nm in order to determine the concentration of the MO solution. We used a concentration of 2 mM methanol solution, isopropanol (IPA) as holes (h⁺), and hydroxyl radicals (OH) scavengers to detect the reactive species [39].

We measured the PEC biosensing performance by the electrochemical workstation (CHI660E). Simultaneously, the supporting electrolyte was a 0.1 M solution of phosphate-buffered saline (PBS) (pH = 7.0) We determined the detection limit to be 0.5 V by observing the lowest value that could be distinguished from the background signal. We investigated the gas-sensing properties of the as-synthesized nanohybrids by a home-built test chamber (1 L). We used a nanoamperemeter (GT8230) to document the measuring current as a function of the exposure time by applying a sweep voltage (5V) under 100 ppm of NH₃.

3. Results and Discussions

We used SEM and TEM to characterize the surface morphology and cross-sectional arrangement of the pure TiO₂ NTAs, referenced pristine BiVO₄ films, and binary BiVO₄/TiO₂-NTAs nanohybrids with different BiVO₄ NP hydrothermal synthesis times (5 h, 10 h, and 20 h), as displayed in Figure 2. We prepared the BiVO₄ NPs with uniform size and reg-

ular spherical-shaped distribution on the FTO conductive surface by the hydrothermal method, and the average particle size of the BiVO_4 NPs was about 50 nm. Moreover, we found spherical-form BiVO_4 NPs with agglomeration in some places, which enhance the specific surface area, which increases the active surface area for the redox reactions [40]. Simultaneously, we manufactured the TiO_2 NTAs with smooth and uniform top surfaces on the Ti substrate, and the average pore diameter and wall thickness are about 100 nm and 10 nm, respectively, as depicted in Figure 2b. The inset in Figure 2b is the TEM image of a single nanotube, illustrating that the outer diameter and length are separately ca. 100 nm and 5 μm , respectively, which accord well with the top-view SEM observation. We present the typical SEM images for the vertical-view morphologies of the $\text{BiVO}_4/\text{TiO}_2$ -NTAs nanohybrids for increasing the BiVO_4 NP hydrodeposition times from 5 h to 20 h with a precursor solution with pH values successively equal to 2, 5, and 8 after annealing at 450 °C in Figure 2c–e. We observed distinctly different nanotopographies (from dispersed or aggregated spherical-shaped NPs to clustered nanosheets) after the decoration of BiVO_4 onto the surfaces of the TiO_2 NTAs. We present the SEM image for the $\text{BiVO}_4/\text{TiO}_2$ -NTAs nanocomposites with a BiVO_4 NP hydrothermal preparation time of 5 h ($\text{BiVO}_4/\text{TiO}_2$ -NTAs-5) in Figure 2c, which we could use to precisely examine the discrete distribution of BiVO_4 NPs with an average size of nearly 30 nm, which embrace upon opening and infill the interstices of TiO_2 NTAs. Furthermore, we present the overhead-view SEM image of $\text{BiVO}_4/\text{TiO}_2$ -NTA-10 in Figure 2d. The BiVO_4 NPs with a mean size of ca. 50 nm are evenly distributed on the top surface of the nanotube, as well as in the intertube space, and they also fill the interior of the nanotubes, connecting them together. The skeleton of the TiO_2 NTAs remains unchanged. BiVO_4 nanosheets (NSs) formed in some areas on the surfaces of the TiO_2 NTAs. The top-view SEM image of the $\text{BiVO}_4/\text{TiO}_2$ -NTAs nanocomposites with a BiVO_4 hydrothermal reaction time of 20 h, labeled as $\text{BiVO}_4/\text{TiO}_2$ -NTAs-20, are exhibited in Figure 2e. The result further verified that the synthetic reaction time and pH value for the preparation of BiVO_4 are essential factors, as they have a tendency to aggregate together by forming NS clusters, randomly distributed on the top surfaces of the nanotubes, with a length and width of approximately 120 nm and 100 nm, respectively, which are in good agreement with the published article in terms of the occurrence of the introduction of foreign species at the surface, which usually block the nanotube openings [41].

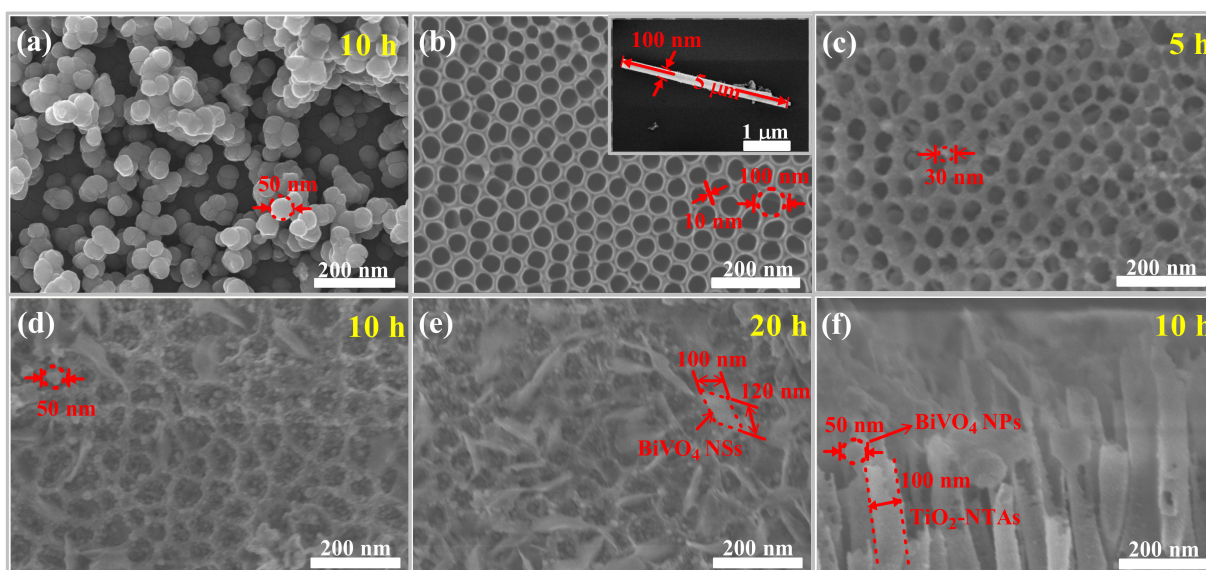


Figure 2. SEM pictures of (a,b) top-view for as-formed pristine BiVO_4 films and pure TiO_2 -NTAs, and low-resolution TEM picture for individual nanotube of TiO_2 inset in figure (b). (c–e) Top-view SEM images of $\text{BiVO}_4/\text{TiO}_2$ -NTAs with BiVO_4 hydrothermal-deposition times of 5 h, 10 h, and 20 h, respectively. (f) SEM picture with cross-section for as-obtained $\text{BiVO}_4/\text{TiO}_2$ -NTAs nanoheterostructures with BiVO_4 nanoparticles (NPs) deposited time 10 h.

To definitively illustrate the formation of $\text{BiVO}_4/\text{TiO}_2$ -NTAs nano-heterostructures, we performed a cross-sectional SEM characterization on a representative specimen of $\text{BiVO}_4/\text{TiO}_2$ -NTAs-10, as presented in Figure 2f. The incorporation of BiVO_4 NPs led to an increase in the surface roughness of the $\text{BiVO}_4/\text{TiO}_2$ -NTAs-10 nano-hybrids, which indicated that the particle size of the BiVO_4 and the outer diameter of the individual TiO_2 nanotube were about 50 nm and 100 nm, respectively, which coincide with the results of Figure 2b,d. Most notably, the deposited BiVO_4 NPs screened the entrances of the TiO_2 NTAs, successfully preparing the $\text{BiVO}_4/\text{TiO}_2$ -NTAs nano-heterostructures.

We examined the crystalline structures and phase compositions of the as-prepared films in depth by XRD. We present the XRD patterns of the pristine TiO_2 NTAs, pure BiVO_4 films, and $\text{BiVO}_4/\text{TiO}_2$ -NTAs binary nano-heterojunctions in Figure 3. The $\text{BiVO}_4/\text{TiO}_2$ -NTAs dual nano-heterostructures with various thermal depositing times (5 h, 10 h, and 20 h) correlate with the different pH values (2, 5, and 8, respectively) of the precursor solutions. Evidently, all the specimens had narrowed and sharpened peaks under the hydrothermal crystallization conditions, proving that the as-fabricated products were crystalline, as expected, which is consistent with a previous report [42]. As shown in Figure 3a, there are five diffraction peaks of the untampered TiO_2 NTAs (labeled with a '▼' mark), with diffraction 2θ angles located at 37.88° , 48.12° , 53.97° , 55.10° , and 62.74° , which are indexed to the (004), (200), (105), (211), and (204) diffraction planes, respectively. These results suggest that the sample is anatase TiO_2 (Card No. 21-1272). The anatase TiO_2 , in particular, has a better PEC performance than the other crystal phases, resulting from the smaller effective mass and longer carrier lifetime, which result in a faster migration rate and higher generation of active species for PEC reactions [43]. We present the XRD patterns of the as-obtained BiVO_4 films with pH values equal to 5 of the precursor solution annealing at 450°C in Figure 3b, in which it can be seen that the locations of the diffraction peaks coincide with the tz- BiVO_4 and ms- BiVO_4 phases, according to the standard JCPDS files, which proves the successful fabrication of the m/t- BiVO_4 isotype crystal-phase heterojunctions. Specifically, the prominent peaks sited at 18.3° , 24.4° , 32.7° , 34.7° , 43.8° , and 50.7° typically correspond to the (101), (200), (112), (220), (103), and (213) crystal planes (labeled with a '■' mark) of the tz- BiVO_4 (Card No. 14-0133), respectively. Simultaneously, the ms- BiVO_4 sample displays the characteristic diffraction profiles at 28.8° , 30.5° , 35.2° , 39.7° , 42.5° , 46.7° , 58.0° , and 59.2° (denoted by "◆" mark), corresponding to the (121), (040), (002), (211), (051), (240), (170), and (123) crystal planes, which is in good accordance with Card No. 14-0688. We probed the crystallinities of the hydrothermally precipitated BiVO_4 NPs decorated on the TiO_2 NTAs with various deposition amounts (from 5 h to 20 h) in different pH values (from 2 to 8) of the precursor solution by XRD, as presented in Figure 3c–e.

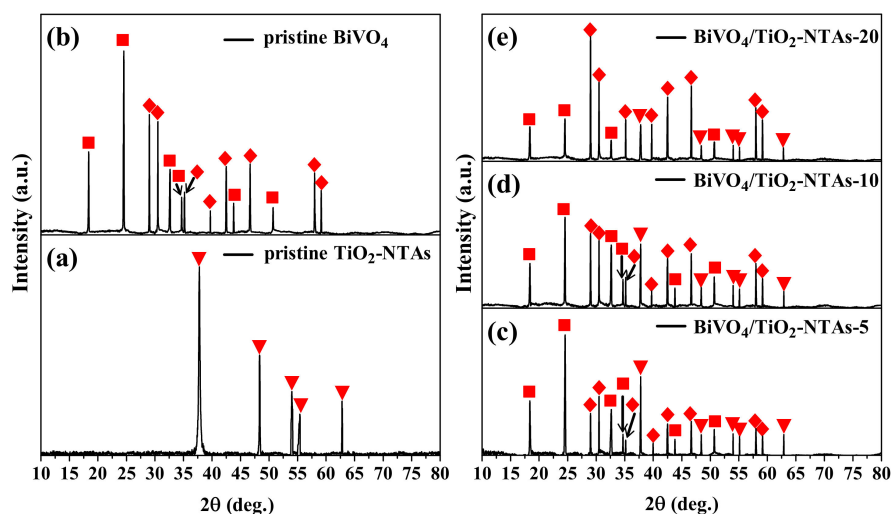


Figure 3. XRD of pristine TiO_2 -NTAs (a,b) pure BiVO_4 films, and (c–e) $\text{BiVO}_4/\text{TiO}_2$ -NTAs nano-hybrids with different hydrothermal deposited amounts, respectively.

Compared with the diffraction peak positions of Figure 3a,b, the XRD patterns for Figure 3c–e vividly imply the lack of impurity peaks, except in the crystal phases of the TiO₂ NTAs, ms-BiVO₄, and tz-BiVO₄ in the BiVO₄/TiO₂-NTAs samples, demonstrating the high purity of the hydrothermal treatment and the prospective achievement of binary m&t-BiVO₄/TiO₂-NTAs heterostructure nanocomposites (i.e., ms-BiVO₄/TiO₂-NTAs and tz-BiVO₄/TiO₂-NTAs nano-heterojunctions). Simultaneously, the XRD patterns of the m&t-BiVO₄/TiO₂-NTA nanohybrids show all the diffraction peaks of the anatase phase TiO₂, which means that the original structure of the TiO₂-NTAs was maintained during the BiVO₄ coating process. The intensities of the diffraction profiles for the TiO₂-NTAs in the patterns of pristine TiO₂-NTAs and m&t-BiVO₄/TiO₂-NTAs nano-heterojunctions decreased with the increasing hydrothermal BiVO₄ deposition times from 0 h to 20 h, mainly owing to the blocking effect of the heterogeneous interface between the m&t-BiVO₄ and TiO₂-NTAs [44], which gradually weakens the XRD signal strength of the anatase TiO₂-NTAs substrates with the increasing deposition amount of BiVO₄. For the as-prepared samples of the BiVO₄/TiO₂-NTAs activated at 450 °C, we probed the mixed heterogeneous phases of the m&t-BiVO₄/TiO₂-NTAs, and the research data are in agreement with the achievement reported by Parida et al., who demonstrated the coexistence of m&t-BiVO₄, as the samples were annealed from 300 °C to 600 °C [45]. More notably, when the pH values for the precursor solution increased successively from 2 to 8, the diffraction peak intensities of (121) and (040) progressively increased for the ms-BiVO₄/TiO₂-NTAs nano-heterostructures, while those of (101) and (200) gradually declined for the tz-BiVO₄/TiO₂-NTAs nano-heterojunctions, as plotted in Figure 3c–e. To quantitatively evaluate the proportions of tz-BiVO₄ ($\eta_{\text{tz-B/T}}$) and ms-BiVO₄ ($\eta_{\text{ms-B/T}}$) in the specimens of pristine BiVO₄, BiVO₄/TiO₂-NTAs-5, BiVO₄/TiO₂-NTAs-10, and BiVO₄/TiO₂-NTAs-20, we made the estimates using Equations (1) and (2) [46,47]. $I_{\text{tz-B/T}}$ and $I_{\text{ms-B/T}}$ refer to the relative intensities of the diffraction profiles for the tetragonal phase (i.e., (101) and (200)) and monoclinic phase (i.e., (121) and (040)), respectively. We present the details on the percentage compositions of the $\eta_{\text{tz-B/T}}$ and $\eta_{\text{ms-B/T}}$ in the single and dual nano-semiconductors in Table 1.

$$\eta_{\text{tz-B/T}} (\%) = (I_{\text{tz-B/T}} \times 100\%) / (I_{\text{tz-B/T}} + I_{\text{ms-B/T}}) \quad (1)$$

$$\eta_{\text{ms-B/T}} (\%) = (I_{\text{ms-B/T}} \times 100\%) / (I_{\text{tz-B/T}} + I_{\text{ms-B/T}}) \quad (2)$$

Table 1. The percentage composition of tetragonal and monoclinic phases of BiVO₄ in pure BiVO₄ and m&t-BiVO₄/TiO₂-NTAs nanoheterojunctions (determined by Equations (1) and (2)) under different pH values of precursor.

as-Formed Samples	pH Value of Precursor	ms-BiVO ₄ ($\eta_{\text{ms-B/T}}$, %)	tz-BiVO ₄ ($\eta_{\text{tz-B/T}}$, %)
pristine BiVO ₄ films	5	46.7	53.3
BiVO ₄ /TiO ₂ -NTAs-5	2	36.8	63.2
BiVO ₄ /TiO ₂ -NTAs-10	5	48.4	51.6
BiVO ₄ /TiO ₂ -NTAs-20	8	71.9	28.1

Table 1 indicates that the fractions of $\eta_{\text{ms-B/T}}$ (or $\eta_{\text{tz-B/T}}$) in the m&t-BiVO₄/TiO₂-NTAs binary nano-heterojunction samples increased (or decreased) with the increasing pH values of the precursor solution, and vice versa, manifesting the efficacious construction of the different ratios of m&t-BiVO₄/TiO₂-NTAs nanohybrids, which was achieved by controlling the pH values, which was entirely in agreement with the results reported by Huang et al. [25]. We believe that the increased pH values for the precursor inhibit the crystal growth of the tz-BiVO₄ due to the enlargement of ms-BiVO₄. The proportion composition of ms-BiVO₄ and tz-BiVO₄ in the individual BiVO₄ films is approximately equal to that in the BiVO₄/TiO₂-NTAs-10 specimen, which verifies the formation of ms/tz-BiVO₄ heterojunctions in BiVO₄ films alone, and further validates the crucial role of the pH value in mediating the heterostructure ratio for m&t-BiVO₄/TiO₂-NTAs nanocomplexes under the determined annealing temperature.

As represented in Figure 4, we performed UV–vis DRS measurements and derived Tauc plots to evaluate the optical absorption intrinsic properties and bandgap values of the as-obtained specimens for unitary and binary semiconductors, respectively, which are indispensable characterization instruments for constructing superior photoresponse nanohybrids. We present the UV–vis DRS detection by a wavelength-dependent absorbance between 350 nm and 700 nm for the pristine TiO₂-NTAs, pure BiVO₄ films, and m&t-BiVO₄/TiO₂-NTAs binary nano-heterojunctions with varying BiVO₄ NP hydrothermal preparation times (5 h, 10 h, and 20 h) in Figure 4a. The absorption edges of the TiO₂-NTAs alone are nearly identical at 393 nm, which is due to the transition of the near band edge (NBE) [48]. The UV–vis DRS spectrum pattern for the pristine BiVO₄ films is perceptibly redshifted compared with that of the single TiO₂-NTAs in Figure 4a, exhibiting the characteristic spectrum related to 496 nm, which is between the intrinsic absorption band edges of ms-BiVO₄ (517 nm) and tz-BiVO₄ (428 nm). Furthermore, as illustrated in the traces of UV–vis DRS for m&t-BiVO₄/TiO₂-NTAs nano-heterostructures, the absorption edges of the dual nanohybrids are substantially transparent to longer wavelength regions in comparison with the pure TiO₂ NTAs, which indicates that the incorporation of BiVO₄ elevates the absorption ability and facilitates the transport of photogenerated electrons, which is the result of the synergistic effect of the heterostructure between m&t-BiVO₄ and TiO₂ NTAs. Evidently, with the increase in the hydrothermal times from m&t-BiVO₄/TiO₂-NTAs-5 to m&t-BiVO₄/TiO₂-NTAs-20, there is a gradual shift of the absorbance boundary to a larger wavelength, which indicates that the bandgap is reducing, and the material is becoming more sensitive to visible light. Simultaneously, all the absorption patterns of the m&t-BiVO₄/TiO₂ NTAs with various amount of BiVO₄, and especially for m&t-BiVO₄/TiO₂-NTAs-10, present conspicuous forward saddle-backing shapes in the visible region (i.e., labeled as area I), which are probably traceable to the increased average atomic distance induced by the V_o defects in BiVO₄ [27]. Additionally, the absorption peaks located at 497 nm, labeled as area II, are ascribed to the absorption of the V_o defects in TiO₂ NTAs [49]. The corresponding E_g values of the as-prepared specimens can subsequently be determined using Tauc plots, as exhibited in Figure 4b. The (αhv)^{1/n} against the photon energy (hv) curves are plotted basing on the following classic Tauc equation [50]:

$$(\alpha hv)^{1/n} = A(hv - E_g) \quad (3)$$

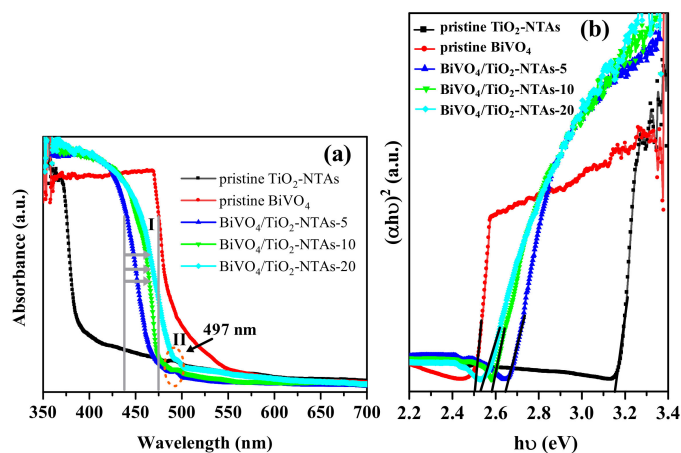


Figure 4. UV-vis DRS spectra (a,b) showed band-gap energy of pure TiO₂-NTAs, pristine BiVO₄ films, and BiVO₄/TiO₂-NTAs nanoheterostructure compositions with different BiVO₄ hydrothermal-deposited amounts, respectively.

The absorption coefficient, Planck's constant, incident light frequency, proportionality constant, bandgap energy, and characteristic integer are denoted by α , h , ν , A , E_g , and n , respectively. The n value depends on the nature of the optical transition and because of the characteristic direct transitions of BiVO₄ and TiO₂, the value of n is 1/2 [51]. Logically,

by extrapolating the linear portion of $(\alpha h\nu)^2$ to zero, we can estimate the E_g for the as-formed samples. The predicted E_g values for the pristine TiO_2 NTAs, bare BiVO_4 films, m&t- $\text{BiVO}_4/\text{TiO}_2$ -NTAs-5, m&t- $\text{BiVO}_4/\text{TiO}_2$ -NTAs-10, and m&t- $\text{BiVO}_4/\text{TiO}_2$ -NTAs-20 are about 3.15 eV, 2.50 eV, 2.65 eV, 2.58 eV, and 2.52 eV, respectively. In order to further evaluate the validity of the calculated E_g values for the m&t- $\text{BiVO}_4/\text{TiO}_2$ -NTAs under different hydrothermal-synthesis conditions, we can use the alternative bandgap prediction method associated with the weighting of the m&t- BiVO_4 content, as follows:

$$E_{g-W} = E_{g-ms} \times \eta_{ms-B/T} (\%) + E_{g-tz} \times \eta_{tz-B/T} (\%) \quad (4)$$

where E_{g-W} , E_{g-ms} , E_{g-tz} , $\eta_{ms-B/T}$, and $\eta_{tz-B/T}$ are the bandgap energies for the weighted contents. The E_g for ms- BiVO_4 is 2.4 eV, while the E_g for tz- BiVO_4 is 2.9 eV, which are the percentages of the monoclinic and tetragonal phases of BiVO_4 in m&t- $\text{BiVO}_4/\text{TiO}_2$ -NTAs nano-heterojunctions, respectively. For convenience, we list the detailed comparison results in Table 2. By stripping out the impact of the TiO_2 -NTAs substrates for the energy-band structures of the m&t- $\text{BiVO}_4/\text{TiO}_2$ -NTAs with different preparation conditions, the obtained E_g from the Tauc formula and valuated E_{g-W} are essentially consistent, as expected, which reinforces the assumption that the presence of BiVO_4 associated with V_o provides a synergistic enhancement in the visible-light absorption, which, in turn, promotes the energy coupling between photons and excitons. The difference in the E_g values between pristine BiVO_4 and m&t- $\text{BiVO}_4/\text{TiO}_2$ -NTAs-10 under the same hydrothermal manufactured environment probably derives from the discrepancy in the thickness of the photoactive layer between them [52].

Table 2. Comparative data of E_g for Tauc and E_{g-W} for weighted contents towards m&t- $\text{BiVO}_4/\text{TiO}_2$ -NTAs dual nano-hybrids with different fabrication conditions.

as-Prepared Samples	Calculated E_g for Tauc (eV)	Predicted E_{g-W} (eV)
m&t- $\text{BiVO}_4/\text{TiO}_2$ -NTAs-5	2.65	2.66
m&t- $\text{BiVO}_4/\text{TiO}_2$ -NTAs-10	2.58	2.59
m&t- $\text{BiVO}_4/\text{TiO}_2$ -NTAs-20	2.52	2.54

In order to further intuitively unveil the synergistic effect of BiVO_4 and TiO_2 NTAs on the surface defects, which profoundly influence the CT process and the performance of PECs, we analyzed the chemical components and bonding configurations of the as-prepared nano-heterojunctions using XPS, as exhibited in Figure 5.

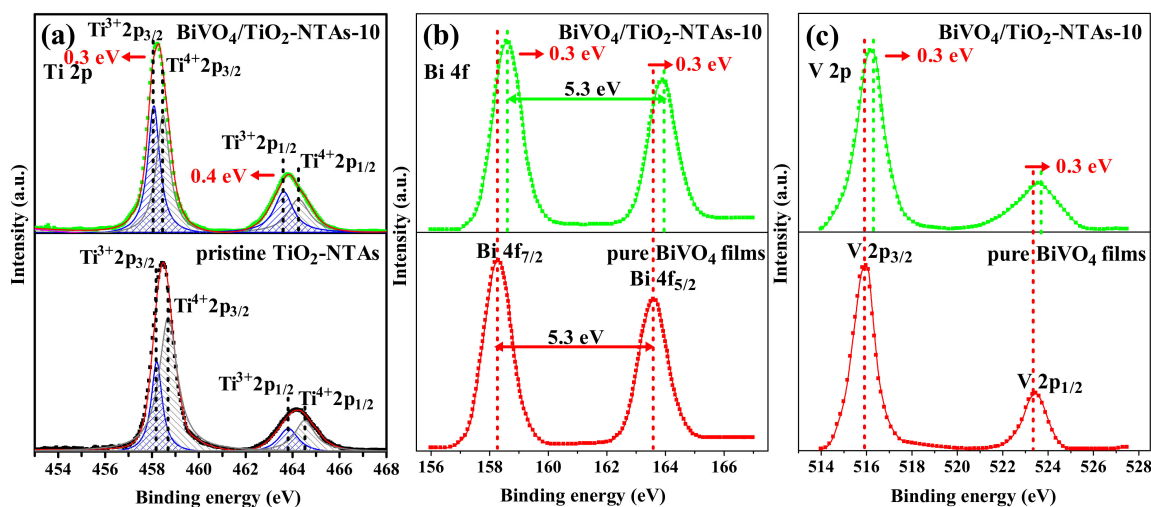


Figure 5. High-resolution X-ray photoelectron spectroscopy characterizations of (a) Ti 2p, (b) Bi 4f, and (c) V 2p core level for pure TiO_2 -NTAs, pristine BiVO_4 films, and m&t- $\text{BiVO}_4/\text{TiO}_2$ -NTA-10, respectively.

Specifically, in Figure 5a, we plot the high-resolution XPS spectra (HR-XPS) of the Ti 2p core level for the pristine TiO₂-NTAs and BiVO₄/TiO₂-NTAs-10 dual nanocomposites. We fit the experimental data points (black and green dots) with a curve (red solid line) using a mixed Gaussian–Lorentzian function. We chose this function because it provided the optimized fit to the data points, as determined by the nonlinear least-squares fitting algorithm, including Ti³⁺2p_{3/2}, Ti⁴⁺2p_{3/2}, Ti³⁺2p_{1/2}, and Ti⁴⁺2p_{1/2}, which originated from the core levels of Ti³⁺ and Ti⁴⁺. The two intense peaks in the pure TiO₂ NTAs at the binding energies (BEs) sited at 458.5 eV and 464.2 eV represent Ti 2p_{3/2} and Ti 2p_{1/2} [53], respectively. Moreover, the BE of the Ti 2p core level for the referenced BiVO₄/TiO₂-NTAs-10 centered at 458.2 eV and 463.8 eV are assigned to Ti 2p_{3/2} and Ti 2p_{1/2} [54], respectively. Additionally, the BE values of the different oxidation states of the Ti atoms are distinct. The BE peaks located at 458.7 eV, 464.5 eV, 458.5 eV, and 464.3 eV are attributed to the Ti⁴⁺ valence state [55], and the BE peaks positioned at 458.1 eV, 463.6 eV, 458.2 eV, and 463.9 eV are attributed to the Ti³⁺ valence state and V_o defects in the TiO₂ NTAs [54,56,57]. We present the surface atomic Ti³⁺/Ti⁴⁺ ratios of the pristine TiO₂-NTAs specimens and binary m&t-BiVO₄/TiO₂-NTAs-10 nano-heterojunctions in Table 3, which we obtained by calculating the integral fitting of the peak areas for the concentration of the spin-orbit-splitting Ti 2p_{1/2} and Ti 2p_{3/2} core levels in the Ti 2p XPS spectra, which directly correspond to the concentrations of the V_o defects (Ti³⁺) and Ti⁴⁺ [58]. We found an explicit shift of 0.3–0.4 eV to a low BE (redshift) in the peak positions of Ti 2p for m&t-BiVO₄/TiO₂-NTAs-10 compared with the pristine TiO₂ NTAs, which mainly derived from the CT from the BiVO₄ to TiO₂ after the formation of the heterostructures [59], which increased the electron density and V_o defect concentration in the TiO₂ NTAs [60].

Table 3. Surface atomic ratios Ti³⁺/Ti⁴⁺ of Ti 2p XPS spectra for spin-orbit splitting doublets Ti 2p_{1/2} and Ti 2p_{3/2} towards to the samples of pristine TiO₂-NTAs and BiVO₄/TiO₂-NTAs-10, respectively.

as-Prepared Samples	Assignment	Binding Energy (eV)	Surface Atomic Ratio Ti ³⁺ /Ti ⁴⁺
pristine TiO ₂ -NTAs	Ti 2p _{3/2}	458.5	0.543
	Ti ³⁺ 2p _{3/2}	458.2	
	Ti ⁴⁺ 2p _{3/2}	458.7	
	Ti 2p _{1/2}	464.2	
	Ti ³⁺ 2p _{1/2}	463.9	
	Ti ⁴⁺ 2p _{1/2}	464.5	
m&t-BiVO ₄ /TiO ₂ -NTAs-10	Ti 2p _{3/2}	458.2	0.988
	Ti ³⁺ 2p _{3/2}	458.1	
	Ti ⁴⁺ 2p _{3/2}	458.8	
	Ti 2p _{1/2}	463.8	
	Ti ³⁺ 2p _{1/2}	463.6	
	Ti ⁴⁺ 2p _{1/2}	464.8	

As can be observed in Figure 5b, the HR-XPS of the Bi 4f core level in the pure BiVO₄ films reveals two peaks at 158.3 eV and 163.6 eV, which index to the orbits of Bi 4f_{7/2} and Bi 4f_{5/2} [61], respectively. In contrast, the spin-orbit splitting of Bi 4f (158.6 eV and 163.9 eV) for BiVO₄/TiO₂-NTAs-10 shift to a higher BE by approximately 0.3 eV, relative to its values for pristine BiVO₄ films. The separation between the splitting of the two spin orbits of Bi 4f is 5.3 eV for both the BiVO₄ films alone and BiVO₄/TiO₂-NTAs-10, which is attributed to the expected oxidation state of Bi³⁺ in BiVO₄ [62]. As plotted in Figure 5c, two spin-orbit-splitting peaks of V 2p are centered at 515.9 eV and 523.4 eV for the pure BiVO₄ films, assigned to V 2p_{3/2} and V 2p_{1/2}, respectively, and certifying the existence of the V⁵⁺ oxidation state in BiVO₄ [63]. Compared with that of bare BiVO₄, the V 2p spin-orbit peaks of BiVO₄/TiO₂-NTA-10 (i.e., V 2p_{3/2} and V 2p_{1/2}) shifted to the higher BE at around 0.3 eV of 516.2 eV and 523.7 eV, respectively. The phenomenon of the BE shift to greater values for the Bi 4f and V 2p core levels for BiVO₄/TiO₂-NTAs-10 than pure BiVO₄ are indicative of the electron migration from BiVO₄ to TiO₂ between the different components in the interface of the nanocomposites, which suggests the weakened electron

screening effect because of the decrease in the electron density for the BiVO_4 [64], which is consistent with the aforementioned XPS analysis of Ti 2p for $\text{BiVO}_4/\text{TiO}_2$ -NTAs-10.

We applied XPS detection to further certify the influence of the various pH values of the precursor (2, 5, 8) on the surface valence states and V_o defect concentration of the interface in the as-prepared nano-heterostructures of $m\&t\text{-BiVO}_4/\text{TiO}_2$ -NTAs with different hydrodeposition times (5 h, 10 h, and 20 h). We present the Bi 4f-core-level high-resolution XPS spectra of the $m\&t\text{-BiVO}_4/\text{TiO}_2$ -NTA nano-heterojunctions with precipitation times of 5 h, 10 h, and 20 h in Figure 6a. The split BE peaks of Bi 4f appear at 158.6 eV–158.9 eV and 163.9 eV–164.3 eV for Bi 4f_{7/2} and Bi 4f_{5/2}, respectively, which are characteristics of the trivalent oxidation state of Bi element species [61,65,66]. Compared with the $m\&t\text{-BiVO}_4/\text{TiO}_2$ -NTAs-5 sample (158.9 eV and 164.3 eV for Bi 4f_{7/2} and Bi 4f_{5/2}, respectively), the spin-orbit splitting of the Bi 4f_{7/2} and Bi 4f_{5/2} signals for $\text{BiVO}_4/\text{TiO}_2$ -NTA-20 (158.7 eV and 164.1 eV, respectively), and $\text{BiVO}_4/\text{TiO}_2$ -NTAs-10 (158.6 eV and 163.9 eV, respectively) slightly shift towards lower BE values by 0.2 eV and 0.3 eV, respectively, sufficiently attesting to the interfacial interaction that is formed in a typical $m\&t\text{-BiVO}_4/\text{TiO}_2$ -NTAs heterojunction sample. We present the core level XPS spectra of the V 2p for $m\&t\text{-BiVO}_4/\text{TiO}_2$ -NTAs nano-hybrids with deposition times of 5 h, 10 h, and 20 h in Figure 6b. Two asymmetric BE peaks are centered at 516.5 eV and 524.2 eV for the V 2p of $m\&t\text{-BiVO}_4/\text{TiO}_2$ -NTAs-5, which are ascribed to the characteristic spin-orbit signals of V 2p_{3/2} and V 2p_{1/2} [67], respectively, while the broad V 2p XPS spectra of $m\&t\text{-BiVO}_4/\text{TiO}_2$ -NTAs-10 and $m\&t\text{-BiVO}_4/\text{TiO}_2$ -NTAs-20 exhibited characteristic splitting BE peaks at 516.2–516.3 eV and 523.7–524.0 eV, respectively, which can be assigned to the V 2p_{3/2} and V 2p_{1/2} spin-orbit signals [68,69], respectively. Coincidentally, besides the core level XPS spectra of Bi 4f, we distinctly observed a slight shift to the lower BE values in the core-level signals of V 2p for the $m\&t\text{-BiVO}_4/\text{TiO}_2$ -NTAs-10 and $m\&t\text{-BiVO}_4/\text{TiO}_2$ -NTAs-20 samples compared with that of $m\&t\text{-BiVO}_4/\text{TiO}_2$ -NTAs-5, which is evidence of the existence of V^{4+} in $\text{BiVO}_4/\text{TiO}_2$ -NTAs nano-heterostructures. Based on previous research reports [59,70], we are inclined to accept that the lower shift in the BE value for the XPS peak has an inevitable relationship with the presence of V_o defects, which is due to the changes in their local coordination environments and the increase in the electron density of the Bi and V atoms after introducing the V_o . The further deconvolution of each asymmetric V 2p-core-level peak of all the specimens using Gaussian distribution peaks produces two doublets: the high-intensity doublet observed at the higher BE values, which was assigned to the V^{5+} state, and the low-intensity doublet at lower BE values, which indicated the presence of V^{4+} related to V_o defects in BiVO_4 [71]. As demonstrated in Figure 6b, for the $m\&t\text{-BiVO}_4/\text{TiO}_2$ -NTAs-5 sample, besides the signals at 516.5 eV and 524.1 eV that index to the V 2p_{3/2} and V 2p_{1/2} peaks of V^{5+} [32], the signals sited at 516.2 eV and 523.4 eV confirm the presence of the V^{4+} valence state [72]. To further deconvolute the V 2p lines of the $m\&t\text{-BiVO}_4/\text{TiO}_2$ -NTAs-10 sample, the profiles of the V 2p_{3/2} doublet at the BE values of 515.5 eV and 516.3 eV can be assigned to the V^{4+} 2p_{3/2} and V^{5+} 2p_{3/2}, respectively, and the peak of the V 2p_{1/2} core level has two components: V^{5+} 2p_{1/2} and V^{4+} 2p_{1/2}, with the latter appearing at lower BE values, located at 523.8 eV and 523.1 eV [73,74], respectively. Eventually, each V 2p core-level signal for the $m\&t\text{-BiVO}_4/\text{TiO}_2$ -NTAs-20 sample is decomposed into V^{4+} and V^{5+} doublet peaks, exhibiting the V^{4+} 2p_{3/2} and V^{4+} 2p_{1/2} peaks centered at the BE values of 515.8 eV and 523.3 eV, respectively, and showing the V^{5+} 2p_{3/2} and V^{5+} 2p_{1/2} peaks at the BE values of 516.4 eV and 524.0 eV, respectively, which correspond to the V^{4+} and V^{5+} cations in BiVO_4 [75,76], respectively. Additionally, the $m\&t\text{-BiVO}_4/\text{TiO}_2$ -NTAs nano-heterojunctions are oxygen-deficient through the electroneutrality principle, and the V^{4+}/V^{5+} molar ratios dictate the amount of nonstoichiometric oxygen, which is proportional to the ratio of the peak area of V^{4+}/V^{5+} [77]. As depicted in Table 4, the calculated surface molar ratio of $m\&t\text{-BiVO}_4/\text{TiO}_4$ -NTA-10 had a higher ratio of V^{4+}/V^{5+} (0.587) than that for $\text{BiVO}_4/\text{TiO}_4$ -NTA-20 (0.491), and the lowest ratio was for $\text{BiVO}_4/\text{TiO}_4$ -NTA-5 (0.436).

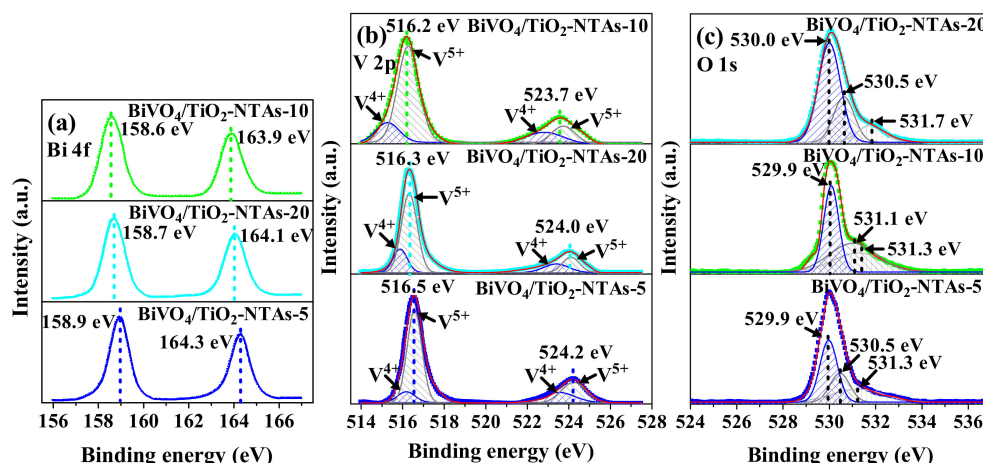


Figure 6. HR-XPS spectroscopy characterizations of (a) Bi 4f, (b) V 2p, and (c) O 1s core levels for m&t-BiVO₄/TiO₂-NTAs heterojunctions nanohybrids with different hydrothermal-synthesis times 5 h, 10 h, and 20 h, respectively.

Table 4. Surface molar ratios V⁴⁺/V⁵⁺ of V 2p XPS spectra for spin-orbit splitting doublets V 2p_{1/2} and V 2p_{3/2} as to the specimens of m&t-BiVO₄/TiO₂-NTAs with different hydrothermal synthesis times, respectively.

as-Prepared Samples	Assignment	Binding Energy (eV)	Surface Atomic Ratio V ⁴⁺ /V ⁵⁺
m&t-BiVO ₄ /TiO ₂ -NTAs-5	V ⁴⁺ 2p _{3/2}	516.2	0.436
	V ⁵⁺ 2p _{3/2}	516.5	
	V ⁴⁺ 2p _{1/2}	523.4	
	V ⁵⁺ 2p _{1/2}	524.1	
m&t-BiVO ₄ /TiO ₂ -NTAs-10	V ⁴⁺ 2p _{3/2}	515.5	0.587
	V ⁵⁺ 2p _{3/2}	516.3	
	V ⁴⁺ 2p _{1/2}	523.1	
	V ⁵⁺ 2p _{1/2}	523.8	
m&t-BiVO ₄ /TiO ₂ -NTAs-20	V ⁴⁺ 2p _{3/2}	515.8	0.491
	V ⁵⁺ 2p _{3/2}	516.4	
	V ⁴⁺ 2p _{1/2}	523.3	
	V ⁵⁺ 2p _{1/2}	524.0	

To further verify the existence of V_o defects in the surface region of the as-prepared m&t-BiVO₄/TiO₂-NTAs nano-heterostructures, we analyzed the HR-XPS spectra of the O 1s core-level signals, and we present the results in Figure 6c. We deconvoluted all of the specimens into three components by Gaussian function fitting, indexing to three oxygen species: lattice oxygen (L_o), V_o, and adsorbed oxygen (A_o), which was evidenced by the corresponding characteristic peaks at 529.9–530.0 eV, 530.5–531.1 eV, and 531.3–531.7 eV [78–81], respectively. In order to intuitively unveil the influence of the hydrothermal preparation environment on the number of V_o defects, we summarize the estimated V_o/(L_o + A_o) and A_o/(L_o + V_o) molar ratios of the O 1s XPS spectra for the m&t-BiVO₄/TiO₂-NTAs specimens with various hydrothermal synthesis times (5 h, 10 h, and 20 h) in Table 5, with the ratios of the peak area decomposed into three components: V_o, L_o, and A_o. The maximal molar ratio value of V_o/(L_o + A_o) for m&t-BiVO₄/TiO₂-NTAs-10 is 0.571, followed by 0.402 for m&t-BiVO₄/TiO₂-NTAs-20, and the minimal value of 0.361 for m&t-BiVO₄/TiO₂-NTAs-5. Simultaneously, the molar ratio values of A_o/(L_o + V_o) evinced a similar varied trend, with that of V_o/(L_o + A_o) for the TiO₂-NTAs hydrothermal precipitation BiVO₄ NPs with times of 5 h, 10 h, and 20 h equaling 0.336, 0.423, and 0.396, respectively, which substantiates the amount of A_o species directly proportional to the V_o levels. According to a synthetic comparison of the above results, the higher surface V⁴⁺/V⁵⁺ molar ratio for the as-formed m&t-BiVO₄/TiO₂-NTAs samples contain a higher amount of V_o defects,

and we observed a greater lower shift in the XPS peak, which was also confirmed by the molar ratio of $A_o/(L_o + V_o)$ for the as-prepared samples, which mainly resulted from the chemisorption of the A_o species at the surface V_o defects of $BiVO_4$ [81]. As expected, the concentration of V_o defects in the dual m&t- $BiVO_4/TiO_2$ -NTAs heterostructure nanosystem was mediated by the synergistic effect of the precipitating time and pH value of the precursor. With the increase in the hydrothermal reaction time from 5 h to 20 h, the number of V_o defects gradually increased and then decreased, instead of showing nonlinear variation, and we found the maximal content of V_o defects in m&t- $BiVO_4/TiO_2$ -NTAs-10. Hence, we conclude that the pH value of the precursor primarily controls the concentration of the V_o defects in the m&t- $BiVO_4/TiO_2$ -NTAs heterostructure nanosystem.

Table 5. Surface $V_o/(L_o + A_o)$, and $A_o/(L_o + V_o)$ molar ratios of O 1s XPS spectra for the specimens of m&t- $BiVO_4/TiO_2$ -NTAs with different hydrothermal synthesis times (5 h, 10 h, and 20 h), respectively.

as-Prepared Samples	Assignment	Binding Energy (eV)	$V_o/(L_o + A_o)$, and $A_o/(L_o + V_o)$
m&t- $BiVO_4/TiO_2$ -NTAs-5	L_o	529.9	0.361 and 0.336
	V_o	530.5	
	A_o	531.3	
m&t- $BiVO_4/TiO_2$ -NTAs-10	L_o	529.9	0.571 and 0.423
	V_o	531.1	
	A_o	531.3	
m&t- $BiVO_4/TiO_2$ -NTAs-20	L_o	530.0	0.402 and 0.396
	V_o	530.5	
	A_o	531.7	

Raman spectroscopy is a powerful technique that can detect vibrational transitions, the bounding states in crystals, and the local structure distortions of inorganic materials. Accordingly, we obtained Raman spectra to evaluate the detailed structural and composition insights for the m&t- $BiVO_4/TiO_2$ -NTAs nanohybrids synthesized by the hydrothermal-precipitation method with various reactive times using a green laser (532 nm), as sketched in Figure 7.

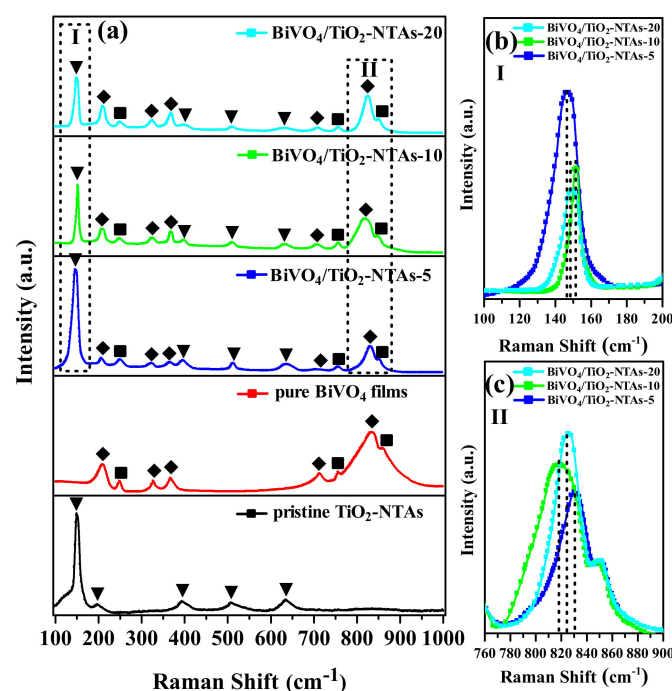


Figure 7. Raman spectra of (a) pristine TiO_2 -NTAs, pure $BiVO_4$ films, and m&t- $BiVO_4/TiO_2$ -NTAs nanoheterostructures with different $BiVO_4$ hydrothermal depositing contents; (b) magnified spectra of the $100\text{--}200\text{ cm}^{-1}$ region, and (c) enlarged view of the $760\text{--}900\text{ cm}^{-1}$ range, respectively.

In Figure 7a, we depict the Raman patterns of the selected samples, the peaks of which are located within the scope of 100–1000 cm^{-1} . In the given Raman spectrum of the pristine TiO_2 -NTAs, we identified a dramatically strong Raman peak at 149.6 cm^{-1} , which corresponded to the E_{1g} vibrational mode, and a lower intense peak around 197.7 cm^{-1} , which indexed to the main E_{1g} active mode of TiO_2 . We could assign the other three medium-intensity peaks located at 397.8 cm^{-1} , 513.8 cm^{-1} , and 639.0 cm^{-1} to the B_{1g} ($A_{1g} + B_{1g}$) and E_{1g} vibrational modes [82], respectively. Anatase phase TiO_2 was indicated by the presence of these Raman peaks, labeled by the symbol “▼”, which is consistent with the XRD analysis. The Raman spectrum analysis of the pure BiVO_4 film as a reference exhibited the presence of eight typical vibrational bands at 210.9 cm^{-1} ; 248.6 cm^{-1} ; 326.5 cm^{-1} ; 367.3 cm^{-1} ; 711.2 cm^{-1} ; 758.3 cm^{-1} ; 821.7 cm^{-1} ; 855.6 cm^{-1} , which are characteristic of mixed BiVO_4 phases with ms- BiVO_4 (marked as “◆”) and tz- BiVO_4 (denoted with “■”), and which confirm the XRD results [83]. Specifically, we observed the external twisting vibrational modes in the pure BiVO_4 at 210.9 cm^{-1} and 248.6 cm^{-1} , corresponding to the formation of monoclinic and tetragonal phases, respectively, which are assigned to the translation/rotation and the Bi–O stretching modes, respectively, while those at 326.5 cm^{-1} and 367.3 cm^{-1} could be ascribed to the asymmetric (B_g symmetry mode) and symmetric (A_g symmetry mode) bending modes of the V–O bond in the VO_4 units for the ms- BiVO_4 phase [37], respectively. Likewise, the pure BiVO_4 materials exhibited Raman bands at 711.2 cm^{-1} and 821.7 cm^{-1} and were assigned to antisymmetric stretching (B_g symmetry mode) and symmetric stretching (A_g symmetric mode) of the two sets of the V–O vibration bond of the monoclinic BiVO_4 phase, respectively. Furthermore, the B_g stretching mode of V–O for the Raman peak sited at 711.2 cm^{-1} is related to the V_o defects [84], which is in good agreement with the UV–vis DRS test. The antisymmetric stretching vibration mode and symmetric bending vibration mode of the V–O bond in the tetragonal phase are indicated by the Raman bands at 758.3 cm^{-1} and 855.6 cm^{-1} , respectively [83]. The Raman spectra of the hydrothermal-synthesized m&t- $\text{BiVO}_4/\text{TiO}_2$ -NTAs nano-heterojunctions adopted the TiO_2 -NTAs decorated with various BiVO_4 deposition times (5 h, 10 h, and 20 h) (Figure 7), which can be distinctly observed in the differences in the Raman patterns between them, which we categorized into four main groups, as follows: (I) Besides the monoclinic and tetragonal phases of BiVO_4 , we observed the Raman characteristic peaks of the anatase TiO_2 -NTAs in all three selected specimens, validating the predictions for the m&t- $\text{BiVO}_4/\text{TiO}_2$ -NTAs mixed-phase nano-heterostructures, which coincide with the UV–vis DRS and XRD experiments. However, the intensities of the Raman peaks for the anatase TiO_2 NTAs located at 149.6 cm^{-1} , 397.8 cm^{-1} , 513.8 cm^{-1} , and 639.0 cm^{-1} gradually decrease when increasing the hydrothermal-reactive times from 5 h to 20 h, which is possibly because the deposited BiVO_4 NPs attenuated the Raman signal of the underlying TiO_2 -NTAs [35]. (II) The peak intensities of the monoclinic phase (i.e., 210.9 cm^{-1} , 326.5 cm^{-1} , 367.3 cm^{-1} , and 821.7 cm^{-1}) increased with the increase in the pH values of the precursor from 2 to 8, while the intensities of the weak peaks for the tetragonal phase decreased with increasing pH values, which demonstrates that the content of m- BiVO_4 increases with the increase in the pH value, and the variation trend of that for t- BiVO_4 is the opposite, which corroborates that the pH value of the precursor has a substantial influence on the m- BiVO_4 and t- BiVO_4 contents in m&t- $\text{BiVO}_4/\text{TiO}_2$ -NTAs nanocomposites, and which is in accordance with the results of the XRD detection. (III) As shown in Figure 7b, the enlarged view of the E_{1g} active vibration peaks of the anatase TiO_2 (corresponding to Region I) centered at 147.2 cm^{-1} , 151.5 cm^{-1} , and 148.6 cm^{-1} for the m&t- $\text{BiVO}_4/\text{TiO}_2$ -NTAs-5, m&t- $\text{BiVO}_4/\text{TiO}_2$ -NTAs-10, and m&t- $\text{BiVO}_4/\text{TiO}_2$ -NTAs-20 specimens, respectively, allow us to discern that the increased deposition of BiVO_4 results in varied shift values to higher wavenumbers in comparison with m&t- $\text{BiVO}_4/\text{TiO}_2$ -NTAs-5, and especially for the m&t- $\text{BiVO}_4/\text{TiO}_2$ -NTAs-10 with the maximum value, which originates from the generation of V_o defects in BiVO_4 caused by the deformation of the TiO_2 lattice after its modification following the introduction of BiVO_4 NPs [85]. (III) Additionally, Figure 7c is the magnified view of Region II in Figure 7a, and the range is between 760 cm^{-1} and

900 cm^{-1} . It explicitly portrays that the Raman peaks of the A_g symmetric stretching modes for the m&t-BiVO₄/TiO₂-NTAs-10 and m&t-BiVO₄/TiO₂-NTAs-20 specimens are broader and shift to lower wavenumbers in comparison with those of m&t-BiVO₄/TiO₂-NTAs-5, and the shifts observed for m&t-BiVO₄/TiO₂-NTAs-10 are the most pronounced and are ascribed to the increase in the V–O bond length owing to the introduction of V_o in BiVO₄ [86,87], which is completely consistent with the XPS experimental results.

To further evaluate the role of the m&t-BiVO₄ decoration and V_o defects in the charge separation, migration, and recombination of the photoexcited e^-h^+ pairs at the heterointerface between the m&t-BiVO₄/TiO₂-NTAs photoabsorber layer and electrolyte, we assessed the PEC characteristics, including the transient I–t curves and EIS of the primary and binary specimens, to explore the photocatalytic mechanism. We present the data in Figure 8a,b. A comparison of the transient photocurrent magnitude is thus a useful technique to demonstrate the m&t-BiVO₄/TiO₂-NTAs heterojunction photoactivity in response to the hydrothermal treatment under different reactive times. We noted the product's photoresponse switching behavior over the course of nine chopped photoswitching cycles at an interval of 10 s under simulated solar light irradiation, and we present the results in Figure 8a. The photocurrent values of the as-obtained specimens in the order of pristine TiO₂-NTAs < pure BiVO₄ films < m&t-BiVO₄/TiO₂-NTAs-5 < m&t-BiVO₄/TiO₂-NTAs-20 < m&t-BiVO₄/TiO₂-NTAs-10 indicates the higher separation efficiency and longer charge carrier lifetime in the binary hetero-nanohybrids than in the single semiconductor. The pristine TiO₂-NTAs had a weak photocurrent intensity (ca. $0.146\text{ }\mu\text{A cm}^{-2}$) owing to the wide E_g , in which there was a limited photoresponse, while the pure BiVO₄ revealed a higher photocurrent response (ca. $0.243\text{ }\mu\text{A cm}^{-2}$) than the primary TiO₂-NTAs, with the on/off switch benefiting from the narrower E_g corresponding to greater visible-light absorption. The current density dramatically increased once the BiVO₄ and TiO₂ NTAs were fabricated into a heterojunction. The m&t-BiVO₄/TiO₂-NTAs-5 and m&t-BiVO₄/TiO₂-NTAs-20 samples had more sensitive photocurrent responses compared with the pure BiVO₄ and TiO₂-NTAs, approximately equaling $0.349\text{ }\mu\text{A cm}^{-2}$ and $0.503\text{ }\mu\text{A cm}^{-2}$, respectively, which were about 2.4 and 3.4 times more than that of the pure TiO₂-NTAs sample, respectively. The m&t-BiVO₄/TiO₂-NTAs-10 sample expressed the highest photocurrent density, reaching about $0.646\text{ }\mu\text{A cm}^{-2}$, which was about 4.4 times that of the pure TiO₂-NTAs. Simultaneously, according to the study of m&t-BiVO₄/TiO₂-NTAs-10, the light caused a spike in the data, which was due to the transient accumulation of photoinduced charges, which suggests that many carriers are produced in the heterojunctions rather than recombination.

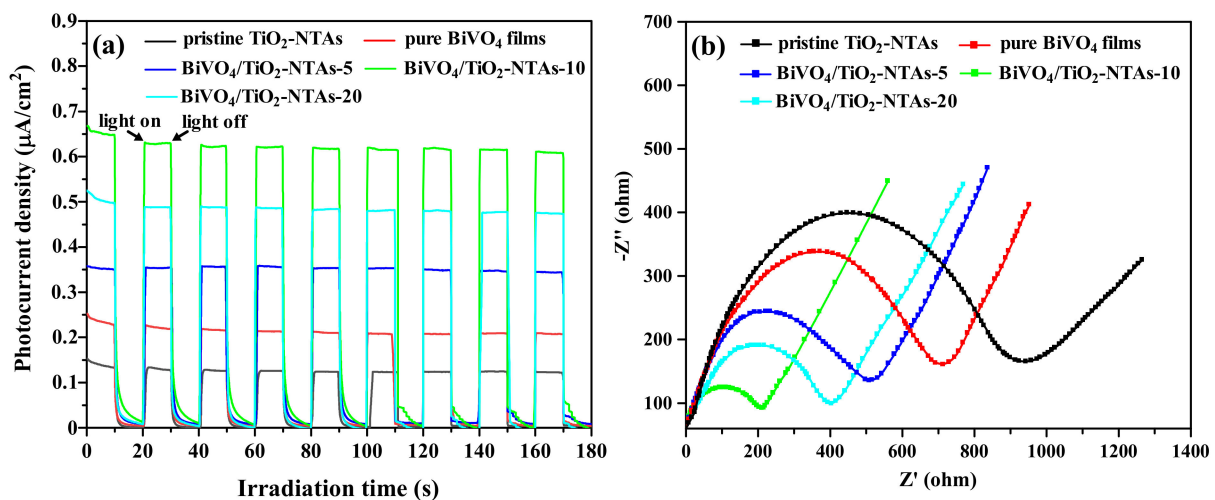


Figure 8. Transient I–t curves for (a,b) EIS of pure TiO₂-NTAs, solely BiVO₄ films, and dual nano-sized m&t-BiVO₄/TiO₂-NTAs nanohybrids deposited BiVO₄ under different prepared times 5 h, 10 h, and 20 h irradiated by AM 1.5G simulated solar light, respectively.

As exhibited in Figure 8b, the Nyquist plot for an EIS measurement typically consists of a series of semicircular arcs at high frequencies, and a linear portion at low frequencies. The resistance to charge separation is represented by the diameter of the semicircle, with a smaller arc radius signifying a greater efficiency of the photoinduced carrier separation. The pristine TiO₂-NTAs sample had the greatest impedance arc radius compared with the other specimens, which suggests the greatest charge transfer resistance in all the selected samples, which is probably due to the poor light sensitivity in the visible-wavelength region for the TiO₂-NTAs, which reduces the electron conduction rate. In comparison with the pure TiO₂-NTAs, the arc radius of the pure BiVO₄ films was further reduced, manifesting the more effective generation and separation of the photogenerated e⁻-h⁺ pairs within the scope of the simulated solar spectrum, which coincides quite well with the results of the UV-vis DRS and transient I-t analyses. The semicircular diameters of all these samples are ranked as follows: pristine TiO₂-NTAs > single BiVO₄ films > m&t-BiVO₄/TiO₂-NTAs-5 > m&t-BiVO₄/TiO₂-NTAs-20 > m&t-BiVO₄/TiO₂-NTAs-10, which is consistent with the variation trend of the abovementioned photocurrent density. The construction of an m&t-BiVO₄/TiO₂-NTAs nano-heterojunction provides an effective way to transport electrons to the charge collector and separate charges at the electrode/electrolyte interfaces. Strikingly, for the m&t-BiVO₄/TiO₂-NTAs nanohybrids, the arc radii of the curves decreased as the amount of BiVO₄ increased (from 5 h to 10 h), and then began to increase when the BiVO₄ deposition time reached 20 h. The smallest radius is seen in the Nyquist curve for BiVO₄/TiO₂-NTAs-10, which indicates the appropriate amount of BiVO₄ NPs required to improve the conductivity and interfacial CT. If too much BiVO₄ is deposited, then this will hinder the CT process for m&t-BiVO₄/TiO₂-NTAs nanocomposites. Hence, the diverse enhancement of the PEC performances are dependent on the different concentrations of V_o defects in m&t-BiVO₄/TiO₂-NTAs nanohybrids, which increases the carrier concentration and the transport of electrons by these channels, which allows for the effective separation of electron-hole pairs, as well as the spontaneous reaction with electrolytes to serve as additional highly reactive sites [88].

Steady-state PL spectroscopy is a broadly acknowledged channel to obtain additional insights into the electronic structure and properties of the active sites on the surfaces or interfaces of BiVO₄/TiO₂-NTAs nano-heterojunctions, whereby information such as the surface V_o and other defects, as well as the efficiency of the charge carrier trapping, migration, and recombination, can be provided. Compared with the change in the absolute intensity for the PL, we focus more on the variations in the steady-state PL spectral weight and features. We present the steady-state PL spectra for the pristine TiO₂-NTAs, pure BiVO₄ films, and binary BiVO₄/TiO₂-NTAs nano-heterojunctions with different BiVO₄ NPs deposition amounts from 5 h to 20 h, excited by a 266 nm fs pulse at an ambient temperature, in Figure 9a,b. When in a steady state, the PL spectrum for pure TiO₂ NTAs exhibits an asymmetric waveband emission plot, consisting of weak strength at 395 nm (3.1 eV) and an intense emission intensity at 489 nm (2.5 eV), which correspond to the NBE radiative transition [89] of the photogenerated carriers and the indirect radiative transition of the self-trapped electrons from V_o defects to holes in the TiO₂-NTAs [90], respectively. Moreover, the steady-state PL pattern for the pure BiVO₄ films were between 300 nm and 800 nm, with two emitted contributions sited at 427 nm (2.9 eV) and 516 nm (2.4 eV). Various authors have associated double emission peaks with the direct radiative recombination of carriers from the CB of V 3d to VB of O 2p and Bi 6s in VO₄³⁻ for t-BiVO₄ and m-BiVO₄ [91,92], respectively. Simultaneously, there are three other successive PL irradiation domains: Region I (from 536 nm to 585 nm), Region II (from 610 nm to 650 nm), and Region III (from 678 nm to 700 nm), which originate from the indirect transition of the self-trapped electrons associated with the V_o defects, surface vanadium vacancies (V_v), and V_o defect states with the holes in the VB of m&t-BiVO₄ [86,93,94], respectively. Additionally, the steady-state PL spectra for the BiVO₄/TiO₂-NTAs binary nano-heterostructures with various BiVO₄ deposition amounts were characterized with an acquisition time of 100 ms, and they also exhibited broad spectral emissions in the scope

from 350 nm to 725 nm (Figure 9b). All the m&t-BiVO₄/TiO₂-NTAs nano-heterosystems expressed three emission peaks located at 395 nm, 427 nm, and 516 nm, which originated from the direct recombination of the carriers between the CB and VB for TiO₂, t-BiVO₄ and m-BiVO₄, respectively, which are identical to the results in Figure 9a. Likewise, according to the differences in the origin of the PL spectra, the visible region can be divided into three parts: Region I (from 536 nm to 585 nm), Region II (from 603 nm to 650 nm), and Region III (from 678 nm to 700 nm), which originated from the indirect transition of the self-trapped carriers with the V_o and V_v defect states in m&t-BiVO₄. Beyond that, we can clearly observe the steady-state PL band in the range of from 447 nm to 509 nm, labeled as Region IIII, which resulted from the indirect radiative transition between the trapped electrons in the V_o defect states and the holes in the VB of the TiO₂-NTAs [95,96]. The PL intensity associated with the V_o defects in the m&t-BiVO₄ increased with the increase in the BiVO₄ deposition times from 5 h to 10 h, and then decreased when the BiVO₄ deposition times were 20 h in Regions I and III, which is in accordance with the characterized results of the concentration for the V_o defects. As expected, the appearance of the PL intensity related to the V_v defects under 450 °C atmospheric annealing conditions without vanadium sources for all the tested [97] specimens manifested the coherent variation trend of the PL intensity for V_o defects, which is mainly attributed to the higher V_o concentration, which leads to a greater carrier density and the promotion of the generation of surface V_v defects ($O_2 + 2V^{5+} + 10e^- \Rightarrow V_v + VO_2$) [98]. The additional V_v defects formed a series of discrete shallow defect levels in the bandgap of the m&t-BiVO₄ photoelectrode, which can trap the photogenerated electrons and promote charge separation, which have positive effects on the PEC performance, as well as on the V_o defects [93,99]. Meanwhile, there was a significant steady-state PL band between 447 nm and 509 nm (Region IIII) that pertained to the photoinduced electron radiative recombination related to the V_o shallow trapping levels in the TiO₂-NTAs [95,96], which is sensitive to the deposition amount of m&t-BiVO₄.

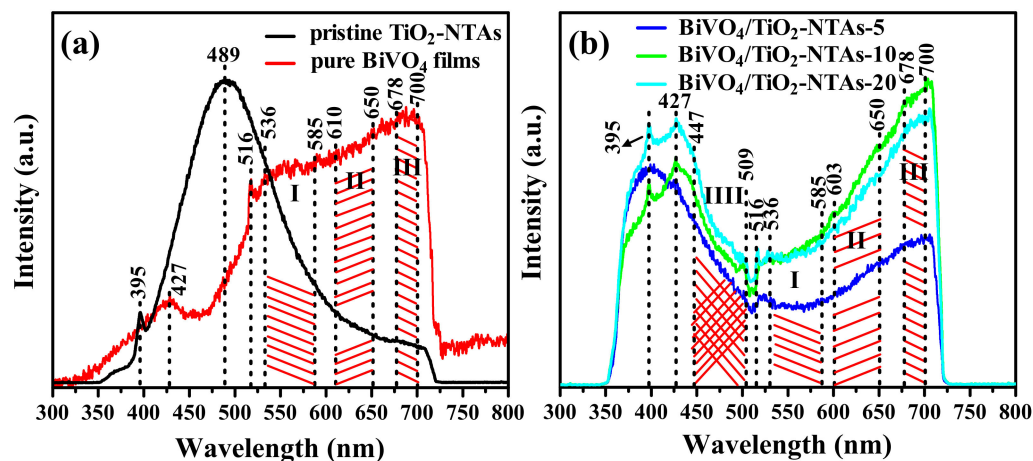


Figure 9. Steady-state PL spectra of bare TiO₂-NTAs and pure BiVO₄ films (a,b) m&t-BiVO₄/TiO₂-NTAs nanoheterojunctions with different depositing times of BiVO₄ excited by 266 nm femtosecond pulse, respectively.

We present the NTRT-PL spectra for the pristine TiO₂-NTAs and pure BiVO₄ film specimens in Figure 10a,b. We irradiated these samples with a monochromatic fs laser wavelength at 266 nm under an atmospheric environment and normal temperature, with an interval time evolution of 1.5 ns.

The NTRT-PL patterns for the bare TiO₂-NTAs sample, as plotted in Figure 10a, express a comparatively low transient PL emitted peak near 395 nm from 0 ns to 3 ns, which is ascribed to the direct radiative transition of the photoinduced carriers between the CB and VB in the TiO₂ NTAs, as stated above [89]. The blueshift phenomenon for the transient PL emission peaks of the pure TiO₂ NTAs emerged at 509 nm, 499 nm, 488 nm, 463 nm, and 447 nm with the increase in the intensities, and then decreased for a time evolution of

0–6 ns, originating from the indirect radiative emissions from the V_o defect levels within the VB of TiO_2 , which is in accordance with the PL earlier reported by other researchers [100]. Simultaneously, we could observe seven transient PL radiative peaks in the pure m&t- $BiVO_4$ film sample, as revealed in Figure 10b, which were centered at 427 nm, 517 nm, 536 nm, 627 nm, 640 nm, 678 nm, and 700 nm, which is consistent with the results of the steady-state PL for the pristine $BiVO_4$ presented in Figure 9a. As described above, we believe that the transient PL emission peaks sited at 427 nm and 516 nm are connected to the NBE direct recombination of t- $BiVO_4$ and m- $BiVO_4$, respectively. Likewise, the other transient PL radiative peaks centered at 536 nm, 627 nm, 640 nm, 678 nm, and 700 nm could be attributed to the indirect transition of the trapping carriers related to the V_o and V_v defects in the pure t&m- $BiVO_4$ films.

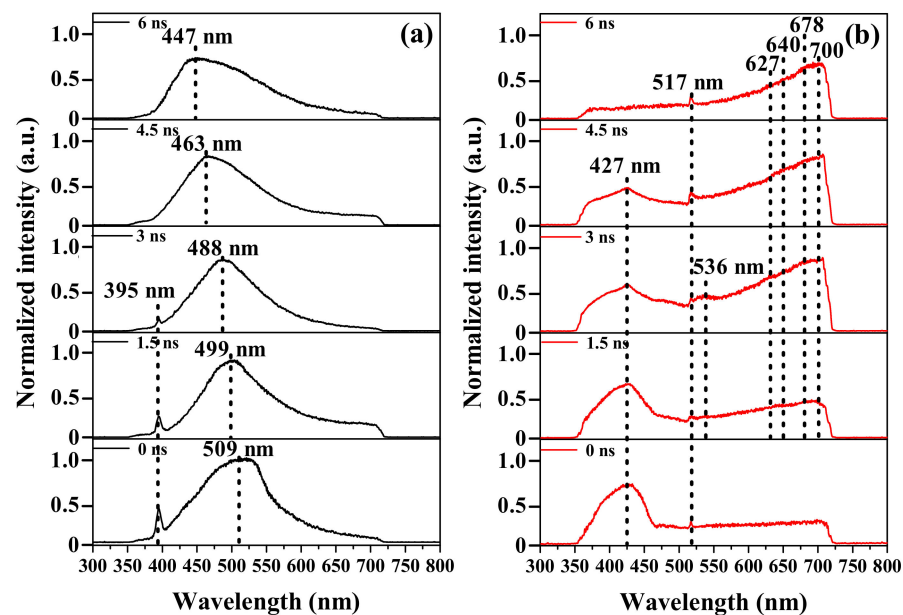


Figure 10. NTRT-PL spectra of the pure TiO_2 -NTAs (a,b) pure $BiVO_4$ films irradiated by fs light with wavelength of 266 nm, respectively.

Ultrafast time-resolved PL spectroscopy is an authoritative indicator tool to track the CT dynamics. Stronger PL intensities represent higher concentrations of defect levels and holes associated with indirect and direct radiative recombination processes, respectively. We present the NTRT-PL spectra of the m&t- $BiVO_4/TiO_2$ -NTAs nano-heterojunctions with various $BiVO_4$ NP hydrothermal preparation times (5 h, 10 h, and 20 h) in Figure 11a–c. For the convenience of discussion, the NTRT-PL-wavelength classified regions agree with the steady-state PL, as discussed above. With the evolution of the time spent recording the spectral, we observed transient PL emission peaks in four different wavelength regions: Region I (from 536 nm to 585 nm); Region II (from 603 nm to 650 nm); Region III (from 678 nm to 700 nm); Region IV (from 447 nm to 503 nm). The as-prepared specimens exhibited Regions I–IV emissions that were unambiguously related to the indirect radiative transitions between the trapped electrons at the V_o and V_v defects in m&t- $BiVO_4$, as well as to the indirect radiative emissions from the V_o defects in the TiO_2 NTAs. These findings were consistent with the steady-state PL spectroscopy in Figure 9b. Additionally, the emitted PL peaks sited at 395 nm, 427 nm, and 518 nm can be assigned to the direct NBE transition of the m&t- $BiVO_4/TiO_2$ -NTAs heterojunctions, which coincide with the results in Figure 10.

The information on the band-gap structure (i.e., CB, VB, and Fermi level (E_F)) is essential to unveiling the interfacial CT mechanism between the m&t- $BiVO_4$ and TiO_2 -NTAs nano-heterojunctions. To further dive into this issue, we subsequently conducted a Mott–Schottky (M–S) analysis on the deliberated pristine TiO_2 NTAs, pure m&t- $BiVO_4$

films, and m&t-BiVO₄/TiO₂-NTAs nanohybrids, as plotted in Figure 12. We used the M-S formula (i.e., $1/C^2 = (2/\epsilon\epsilon_0\epsilon_r N_d)(E-E_{fb}-k_B T/e)$) [101] to assess the flat band potential (E_{fb}) and density of the donor carriers (N_d), where C and e are the differential capacitances of the Helmholtz layer and electron charge (1.602×10^{-19} C), respectively; ϵ_0 is the permittivity of the vacuum (8.85×10^{-12} F m⁻¹); ϵ_r is the relative permittivity (68 for BiVO₄ and 170 for TiO₂); E_{fb} is the hypothetical potential at which the semiconductor bands are flat and the band bending is zero, which is extrapolated from the $1/C^2$ axis in M-S plots; E is the applied electrode potential; k_B and T are the Boltzman constant (1.38×10^{-23} J K⁻¹) and absolute temperature, respectively. Furthermore, we can calculate the N_d value with the following equation [102]: $N_d = (2/\epsilon\epsilon_r\epsilon_0) [d(1/C^2)/dE]^{-1}$. The specimens were of the n type, with positive slopes for the M-S curves of $1/C^2$ versus the potential. We present the calculated values of the N_d , E_{fb} , and CB in Table 6.

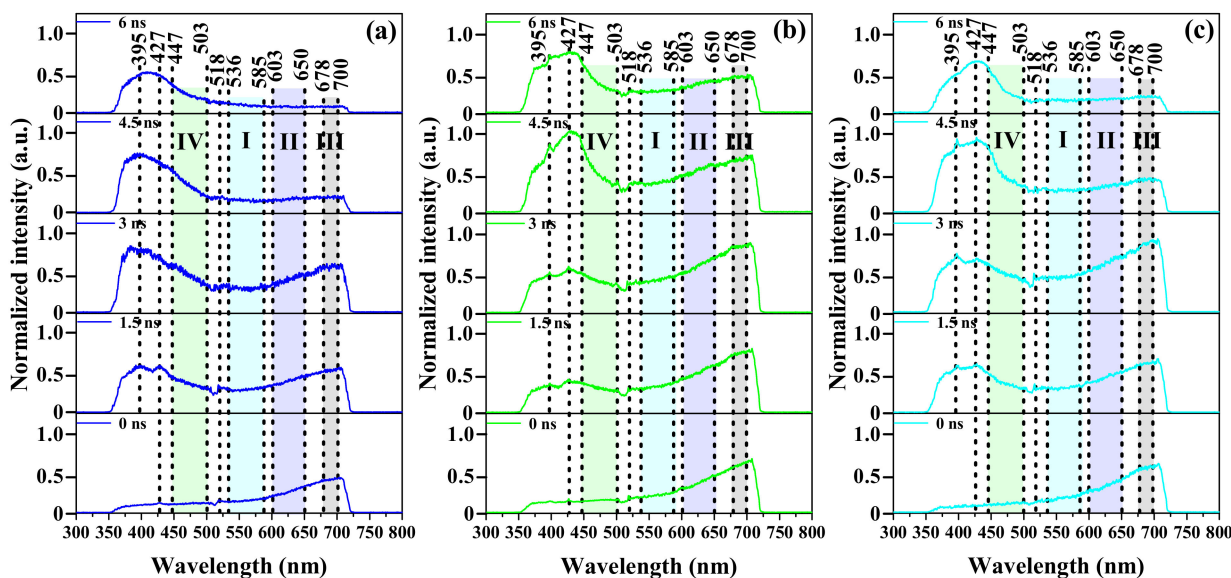


Figure 11. NTRT-PL spectra of the m&t-BiVO₄/TiO₂-NTAs nanoheterojunctions for BiVO₄ NPs with different hydrothermal deposited times: (a) 5 h, (b) 10 h, and (c) 20 h under wavelength of 266 nm irradiation at atmospheric environment, respectively.

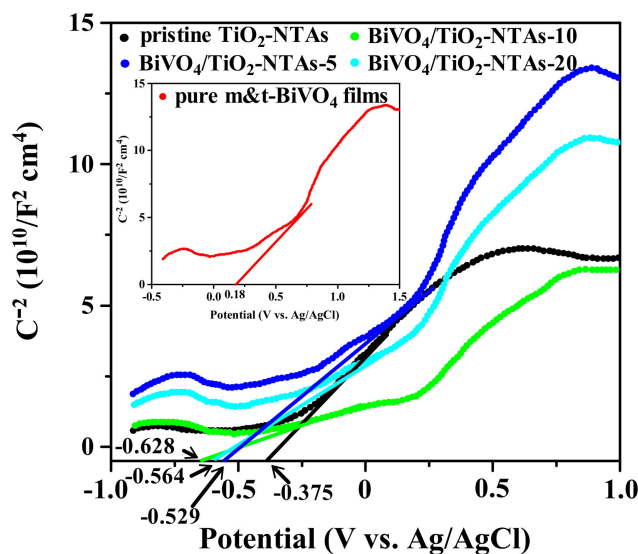


Figure 12. Mott-Schottky plots of the pristine TiO₂-NTAs, pure m&t-BiVO₄ films (inset), and as-obtained BiVO₄/TiO₂-NTAs nanocomposites with different BiVO₄ hydrothermal precipitation times, respectively.

Table 6. The density of donor carriers (N_d), flat band potential (E_{fb}), and position of CB for pure TiO_2 -NTAs, pristine m&t-BiVO₄ films, and m&t-BiVO₄/TiO₂-NTAs nanocomplex with BiVO₄ depositing times 5 h, 10 h, and 20 h, respectively.

Samples	N_d (cm ⁻³)	E_{fb} (vs. NHE)	CB Position (vs. NHE)
pristine TiO ₂ -NTAs	6.2×10^{17}	-0.175	-0.275
Pure BiVO ₄ films	3.3×10^{18}	0.377	0.277
m&t-BiVO ₄ /TiO ₂ -NTAs-5	4.5×10^{18}	-0.329	-0.429
m&t-BiVO ₄ /TiO ₂ -NTAs-10	7.6×10^{18}	-0.428	-0.528
m&t-BiVO ₄ /TiO ₂ -NTAs-20	6.6×10^{18}	-0.364	-0.464

As is evident, the values of the N_d for the samples of bare TiO₂-NTAs, pure m&t-BiVO₄ films, and m&t-BiVO₄/TiO₂-NTAs nano-heterojunctions with different BiVO₄ amounts from 5 h to 20 h are 6.2×10^{17} cm⁻³, 3.3×10^{18} cm⁻³, 4.5×10^{18} cm⁻³, 7.6×10^{18} cm⁻³, and 6.6×10^{18} cm⁻³, respectively. The N_d values for the bare TiO₂-NTAs and pure BiVO₄ films are lower than that of the hydrothermal decorated TiO₂-NTAs with BiVO₄ NPs, which sufficiently validates that the donor density can be improved by a more powerful built-in electric field in the nano-heterojunction. The change trend is also similar to the results of the photocurrent densities and EIS, which substantially reduce the carrier recombination. Furthermore, the N_d values increased with the BiVO₄-NPs hydrothermal reaction times, increasing from 5 h to 10 h, and then decreasing when a more compact BiVO₄-NPs distribution deposition time was applied (20 h), validating that the V_o defects could boost the charge carrier densities and electrical conductivities in the m&t-BiVO₄/TiO₂-NTAs hetero-nanophotoanodes [98]. The number of active sites in BiVO₄ constantly increases as a result of the growing trend of vacancy-state active sites with the increment in the BiVO₄, and it decreases for the excess BiVO₄ deposition mediated by pH values from 2 to 8. Additionally, the E_{fb} of the pristine TiO₂-NTAs, pure m&t-BiVO₄ films, and m&t-BiVO₄/TiO₂-NTAs nano-heterojunctions with different BiVO₄ amounts from 5 h to 20 h are as follows: -0.375 eV, 0.180 eV, -0.529 eV, -0.628 eV, and -0.564 eV vs. Ag/AgCl, respectively. Based on the relationship expression $E_{NHE} = E_{Ag/AgCl} + 0.1976$ (25 °C) [35], they are approximately -0.175 eV, 0.377 eV, -0.329 eV, -0.428 eV and -0.364 eV vs. NHE, respectively. Because the CB potential position (E_{CB}) for the most n-type semiconductors is 0.1 eV higher than that of the E_{fb} [103], the E_{fb} value for the pristine TiO₂ NTAs was -0.175 eV vs. NHE using the M-S plot, which completely coincides with the previously published literature [104]. The calculated value of the E_{CB} for the pure TiO₂ NTAs was -0.275 eV, which is almost consistent with the -0.250 eV of the E_{CB} position reported by other researchers [105]. The V_o defects are thought to function as electron donors, increasing the potential height of the E_{CB} [106]. Moreover, the E_{CB} positions of the m&t-BiVO₄/TiO₂-NTAs heterostructure nano-heterojunctions with different BiVO₄ hydrothermal deposition times (5 h, 10 h, and 20 h) are approximately -0.429 eV, -0.528 eV, and -0.464 eV vs. NHE, respectively. The exposed surface V_o defects in the m&t-BiVO₄ further strengthen the evidence that they act as electron donors, which could promote the electrical conductivity in BiVO₄/TiO₂-NTAs nano-heterojunctions. The presence of V_o defects is especially expected to shift the CB edge of m&t-BiVO₄ towards the VB, resulting in an increase in the bandgap. This effect is caused by the alignment of the E_F between the m&t-BiVO₄ and TiO₂-NTAs, which increases the degree of the band bending at the interface between BiVO₄ and TiO₂-NTAs, which, in turn, facilitates the charge separation and transfer.

On the basis of the above obtained experimental results of the NTRT-PL spectra and M-S plots, we present the mechanisms proposed to interpret the transient CT process for pristine TiO₂ NTAs and pure m&t-BiVO₄ films under fs laser irradiation at a wavelength of 266 nm at room temperature in Figure 13. Due to the absence of CT behavior before the formation of the photoexcited charge carriers, it is likely that the O₂ was spontaneously attached on individual TiO₂ NTAs and m&t-BiVO₄, respectively. Additionally, the E_g for the pristine TiO₂ NTAs is 3.15 eV, employing the aforementioned experimental results for the E_g using the Tauc plots in Figure 4b, and the values of the E_F , E_{CB} , and VB potential

positions (E_{VB}) for the TiO_2 NTAs are -0.10 eV, -0.25 eV, and 2.9 eV versus the potential of normal hydrogen electrode (vs. NHE, E_{NHE}) [105], respectively, which agrees with the M–S analysis and is depicted in Figure 13a. Simultaneously, the values of the E_{CB} and E_F for the $t-BiVO_4$ and $m-BiVO_4$ are 0.24 eV, 1.44 eV, 0.34 eV, and 0.9 eV vs. NHE without photoirradiation conditions, respectively, according to the previously mentioned research [105,107,108], while the E_{VB} edges of the $t-BiVO_4$ and $m-BiVO_4$ are 3.14 eV and 2.74 eV vs. NHE, respectively, using the formula $E_{VB} = E_g - E_{CB}$, and the E_g values for them are 2.9 eV and 2.4 eV, respectively (Figure 13c).

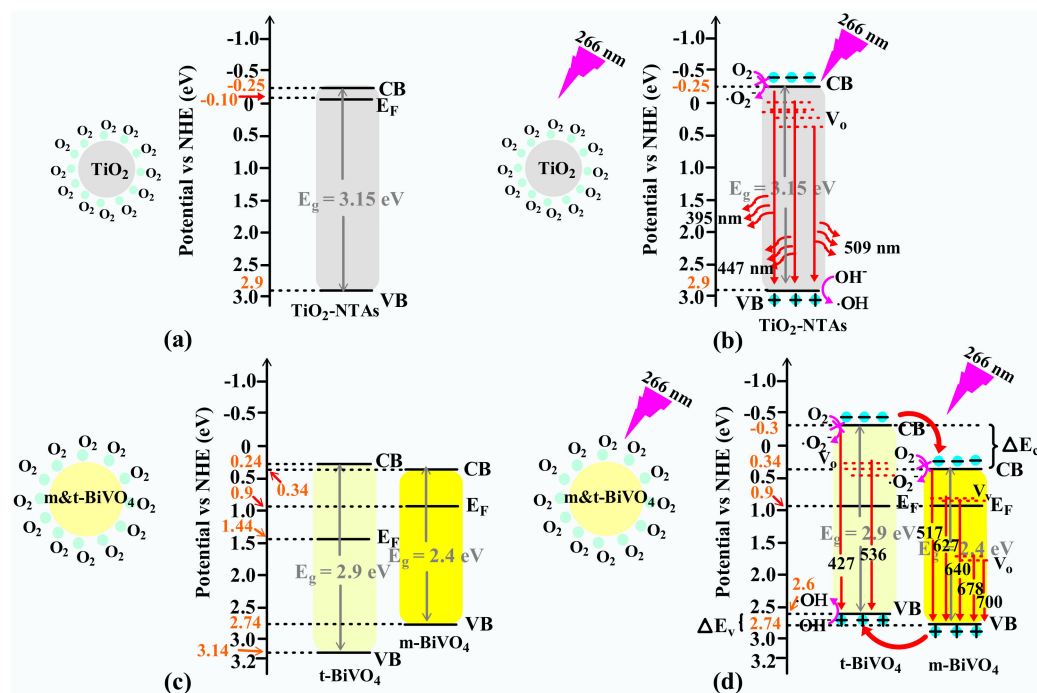


Figure 13. Diagrammatic sketches of (a,c) are CB, VB, and E_F potential positions (vs. NHE) for single TiO_2 -NTAs and $m\&t-BiVO_4$ films before photo-irradiation conditions, respectively; Schematic diagrams (b,d) are photogenerated carriers generated, transferred, and recombination for pristine TiO_2 -NTAs and pure $m\&t-BiVO_4$ films in atmosphere irradiated by UVC light, severally.

In Figure 13b,d, we illustrate the processes of the generation, transfer, and radiative recombination of the photoexcited charge carriers in the TiO_2 NTAs alone and pristine $m\&t-BiVO_4$ when exposed to 266 nm light. For the sample of undecorated TiO_2 NTAs, the large number of electrons in the VB were excited to the CB by the incident photon energy, leaving behind holes in the VB of TiO_2 . This occurs when the photon energy (4.7 eV) is greater than the bandgap energy (3.15 eV) of TiO_2 -NTAs. At the initial time of UVC photoexcitation (denoted as $t = 0$ ns), the concentration of the e^-_{CB} in the CB achieved the maximum value because there was no more generation of charges until the next cycle of light irradiation. We detected two transient PL peaks at 395 nm and 509 nm, which originated from direct and indirect radiative recombination, respectively, as illustrated in Figure 10a. As we have previously investigated [96,106], the V_o defect energy levels consist of a series of discrete levels that act as shallow donor levels slightly below the CB of anatase TiO_2 . The transient PL intensities centered at 499 nm, 488 nm, 463 nm, and 447 nm gradually decreased with the recording time from 1.5 ns to 6 ns, which was accompanied by a similar variation trend for the PL emitted peak centered at 395 nm, which we mainly ascribed to the direct and indirect carrier radiative recombination between the CB, V_o defects, and VB in the TiO_2 NTAs. Based on previous reports [35], we believe that the probability of radiation from a shallow defect level is much greater than from a deep-trapping defect level, resulting in a blueshift of the transient PL peaks, which accords with the gradually decreased amount of e^-_{CB} , as exhibited in Figures 10a and 13b. The atmosphere's oxygen content cannot

trap the CB from the TiO₂-NTAs to generate superoxide radical anions (O_2^-) because the E_{CB} level positions are more positive (-0.25 eV vs. NHE) than the redox potential of O_2/O_2^- (-0.33 eV vs. NHE) [24], which is an essential active oxygen species for impacting the PEC activity. The h^+_{VB} in the VB can oxidize the OH^- into hydroxyl radical (OH) in the atmosphere, which is because the h^+_{VB} level positions ($+2.90$ eV vs. NHE) are more positive than the redox potential of OH/OH^- ($+1.99$ eV vs. NHE) [109].

We present the energy-band diagram of the m-BiVO₄/t-BiVO₄ nano-heterojunction semiconductor after the thermodynamic equilibrium and irradiated by 266 nm fs light in Figure 13d. After the intimate contact between m-BiVO₄ and t-BiVO₄, the E_F of t-BiVO₄ from 1.44 eV is 0.9 eV vs. NHE, and it was the same for the E_F of m-BiVO₄. At the same time, the E_{CB} and E_{VB} of t-BiVO₄ decreases from 0.24 eV to -0.30 eV and from 3.14 eV to 2.60 eV, respectively, and the establishment of an n-n junction at the interface creates an equilibrium electric field, which, in turn, generates an internal electric field. The m-BiVO₄ energy band is decreased while the t-BiVO₄ energy band is increased, which creates an equilibrium state in the nano-system. Hence, the type-II nano-heterojunction bandgap configuration results in a shift in the E_{CB} and E_{VB} of t-BiVO₄ beyond those of m-BiVO₄. The calculated CB offset (ΔE_c) was 0.64 eV, and the VB offset (ΔE_v) was 0.14 eV. When we irradiated the m-BiVO₄/t-BiVO₄ type-II nano-heterojunctions by 266 nm light, the electrons in the VB of the m&t-BiVO₄ were inevitably excited to the CB with simultaneous generated holes in the VB owing to the fact that the radiated photon energy was larger than both the E_g values of the t-BiVO₄ and m-BiVO₄. At the end of fs light irradiation ($t = 0$ ns), the e^-_{CB} concentration of the CB for the m&t-BiVO₄ reached the maximum, spontaneously bringing about the NBE direct radiation recombination processes of the e^-h^+ pairs, which could be responsible for the transient PL peaks sited at 427 nm and 517 nm. Additionally, Dai and Wang et al. [110,111] previously reported that the average lifetime (τ_e) of charge carriers for t-BiVO₄ is shorter than that of m-BiVO₄, demonstrating τ_e values for t-BiVO₄ and m-BiVO₄ of 5.49 ns and 11.22 ns, respectively. The relation between the τ_e and the recombination probability is inversely proportional, and the direct radiative recombination probability for t-BiVO₄ is much greater than that of m-BiVO₄, which means that the NBE radiative PL intensity for t-BiVO₄ ($\lambda_{PL} = 427$ nm) is higher than that of m-BiVO₄ ($\lambda_{PL} = 517$ nm). With the evolution of the spectral recording time from 0 ns to 1.5 ns ($t = 1.5$ ns), the new transient radiative PL peaks emerged at 536 nm, 627 nm, 640 nm, 678 nm, and 700 nm, originating from the indirect radiative PL recombination between the e^-_{CB} in the shallow trapping defect states and the VB of m&t-BiVO₄. The concentration of the e^-_{CB} for t-BiVO₄ decreased when the irradiation time was increased from 1.5 ns to 3 ns ($t = 3$ ns). The ΔE_c should provide a facilitated way for the photogenerated e^-_{CB} injection from the CB of t-BiVO₄ to the CB of m-BiVO₄, and the ΔE_v should promote the photogenerated h^+_{VB} transfer from the VB of m-BiVO₄ to the VB of t-BiVO₄, resulting in an enhanced PL intensity of 536 nm and increased e^-_{CB} concentration for m-BiVO₄, which are responsible for the boosted PL strengths of the emitted wavelength sited at 627 nm, 640 nm, 678 nm, and 700 nm. Afterwards, we observed the gradually decreased transient-PL intensities for all of them with the evolution of the spectral recording time from 4.5 ns to 6 ns ($t = 4.5-6$ ns), which were mainly attributed to the continuous consumption for the e^-_{CB} concentration in t-BiVO₄ and m-BiVO₄. The h^+_{VB} in the VB of m&t-BiVO₄ could convert the OH^- into an OH radical, benefitting from its E_{VB} potential positions that are sufficiently more positive (2.60 eV and 2.74 eV) than the redox potential of OH/OH^- . The trapped O_2 in the CB of m&t-BiVO₄ could not be transformed into O_2^- , which was because the E_{CB} -level positions were lower (-0.30 eV and 0.34 eV) than the redox potential of O_2/O_2^- , as displayed in Figure 13d.

We proposed the plausible kinetic process of interfacial CT in the binary BiVO₄/TiO₂-NTAs nano-heterostructures, which is dependent on the synergistic effect between the content ratio of the m&t-BiVO₄ related to the hydrothermal deposition time and the amount of V_o defects mediated by the pH value, as we schematically illustrate in Figure 14.

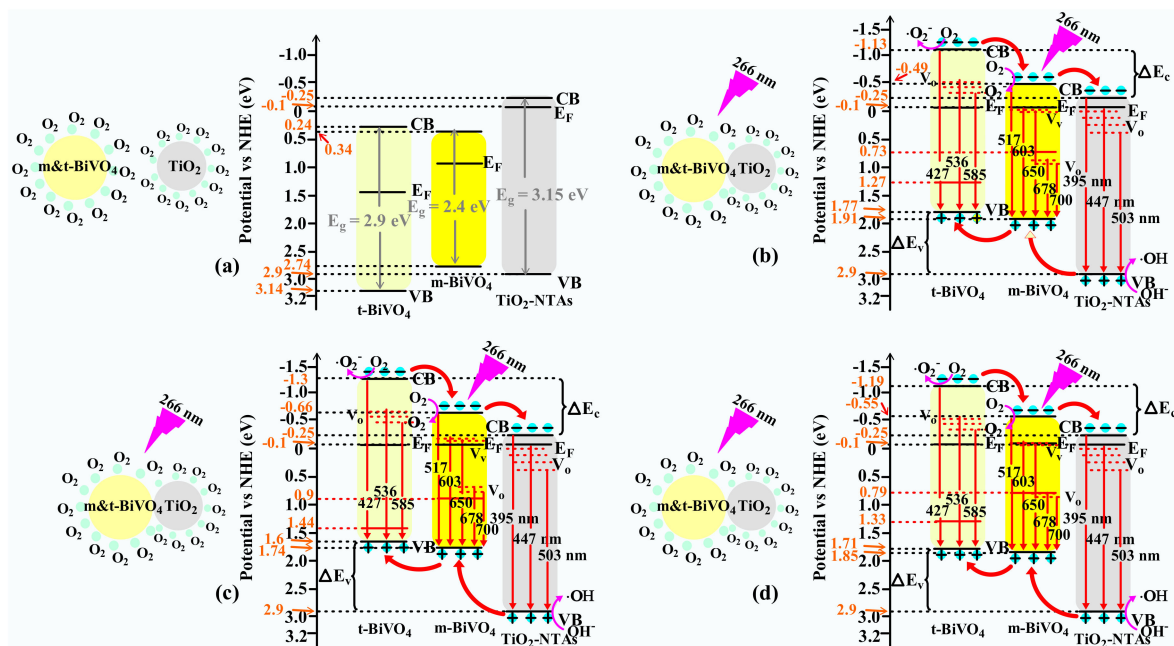


Figure 14. Diagrammatic sketches of (a) CB, VB, and E_F potential positions (vs. NHE) for individual BiVO_4 and TiO_2 -NTAs before contact; (b,c,d) are band-gap structure, charge carriers photo-excited and transient CT for $\text{BiVO}_4/\text{TiO}_2$ -NTAs nanohybrids with various BiVO_4 NPs hydrothermal-deposited amount before and after irradiated by UVC light, respectively.

We present the potential energy positions of the CB, VB, and E_g for the TiO_2 -NTAs and m&t- BiVO_4 against NHE in Figure 14a. The specific potential energy values for these materials are similar to those seen in Figure 13. There is no CT process before the individual m&t- BiVO_4 and pristine TiO_2 -NTAs contact, resulting in rather flat energy bands for the BiVO_4 and TiO_2 -NTAs. We present the band configurations and schematic diagram of the generation, separation, and transport processes for the photogenerated charge carrier assembling of the m&t- $\text{BiVO}_4/\text{TiO}_2$ -NTAs-5 nano-heterojunction before and after irradiation by 266 nm fs light in Figure 14b. Before light irradiation, the detailed potential energy positions of the E_F for the t- BiVO_4 alone and m- BiVO_4 were 1.27 eV and 0.73 eV (vs. NHE), respectively, which agrees with previous reports [25,112]. The CB positions of the single t- BiVO_4 and m- BiVO_4 are 0.24 eV and 0.34 eV, whereas the CB and E_F values for the TiO_2 NTAs are -0.25 eV and -0.1 eV, respectively. Hence, we can deduce the VB potential positions for the t- BiVO_4 , m- BiVO_4 , and TiO_2 -NTAs sited at 3.14 eV, 2.74 eV, and 2.9 eV, respectively, and the E_g values of the t- BiVO_4 , m- BiVO_4 , and TiO_2 NTAs are 2.9 eV, 2.4 eV, and 3.15 eV, respectively. When the close contact between m&t- BiVO_4 with a preparation time of 5 h and TiO_2 NTAs, a t- $\text{BiVO}_4/\text{m-BiVO}_4/\text{TiO}_2$ -NTAs integrated nano-heterojunction barrier is formed at the interface between the BiVO_4 and TiO_2 , owing to the alignment of their different E_F level positions, as stated above. When the thermodynamic equilibrium was established, the E_F values for the t- BiVO_4 and m- BiVO_4 shifted to become -0.1 eV, which was identical to the E_F level of the TiO_2 . Furthermore, the E_C and E_V potential positions for the t- BiVO_4 increased from 0.24 eV to -1.13 eV and from 3.14 eV to 1.77 eV, respectively, while those for the m- BiVO_4 increased from 0.34 eV to -0.49 eV and from 2.74 eV to 1.91 eV, respectively. Logically, the maximal energy difference values of the CB and VB between the t- BiVO_4 and TiO_2 -NTAs are 0.88 eV and 1.13 eV, respectively, denoted as ΔE_c and ΔE_v , respectively, which suggests the formation of an enhanced built-in electric field force on the interfaces between the m&t- $\text{BiVO}_4/\text{TiO}_2$ -NTAs-5 nano-heterojunctions compared with the isolated t- $\text{BiVO}_4/\text{m-BiVO}_4$ type-II nano-heterostructures. We present a schematic diagram of the energy-band potential position for the m&t- $\text{BiVO}_4/\text{TiO}_2$ -NTAs-10 specimen under dark conditions in Figure 14c. After the

thermodynamic equilibrium, the E_F values for t-BiVO₄ and m-BiVO₄ were -0.1 eV, which was the same as the E_F level of the TiO₂. Simultaneously, the E_C and E_V of the t-BiVO₄ increased from 0.24 eV to -1.3 eV and from 3.14 eV to 1.6 eV, respectively, whereas those of the m-BiVO₄ increased from 0.34 eV to -0.66 eV and from 2.74 eV to 1.74 eV, respectively, resulting from the E_F values for the t-BiVO₄ and m-BiVO₄, which were 1.44 eV and 0.9 eV, respectively. The ΔE_C and ΔE_V values for m&t-BiVO₄/TiO₂-NTAs-10 were 1.05 eV and 1.3 eV, respectively, which vividly demonstrates the construction of a powerful built-in electric field driven by the Coulomb repulsive force. Additionally, in Figure 14d, we exhibit the potential energy positions of the bandgap for the m&t-BiVO₄/TiO₂-NTAs-20 sample, tightly contacted and without light irradiation. The calculated E_C and E_V positions of the t-BiVO₄ were -1.19 eV and 1.71 eV, respectively, while those of the m-BiVO₄ were -0.55 eV and 1.85 eV, respectively, when the thermodynamic equilibrium was reached, originating from the E_F values of the t-BiVO₄ and m-BiVO₄, which were 1.33 eV and 0.9 eV moved towards -0.1 eV, respectively, which is in good agreement with the previous description on the variation in the work function with the V_o defect concentration [86]. As a consequence, the heterostructure alignment of m&t-BiVO₄/TiO₂-NTAs-20 with the extreme ΔE_C and ΔE_V between the t-BiVO₄ and TiO₂-NTAs are 0.94 eV and 1.19 eV, respectively. The ΔE_C and ΔE_V values increased with the increasing hydrothermally synthesized times of the BiVO₄ NPs for the m&t-BiVO₄/TiO₂-NTAs nanohybrids from 5 h to 10 h, and then decreased when the BiVO₄ deposition time was 20 h. As expected, the m&t-BiVO₄/TiO₂-NTAs-20 specimen exhibited the maximum values for the ΔE_C and ΔE_V among the as-prepared samples, implying that it is the most forceful supplement of the CT driving force, which is completely consistent with the variation trend of the V_o defect amount and the truth for the effective acceleration of the electron mobility. We illustrate and detail the typical CT pathway for t-BiVO₄/m-BiVO₄/TiO₂-NTAs nano-heterojunctions with different BiVO₄ NP hydrothermal preparation times (5 h, 10 h, and 20 h) under 266 nm light irradiation in ambient air in Figure 14b–d. In the circumstance that the exposed m&t-BiVO₄/TiO₂-NTAs nano-heterojunctions are irradiated by UVC light, the exposure of the t-BiVO₄, m-BiVO₄, and TiO₂ semiconductors to photons with energies (ca. 4.7 eV) greater than the E_g threshold of each material causes a large number of electrons to be excited from the VB to the CB. This leaves behind h^+ in the VB, which creates an e^-h^+ pair. When the UVC light impulse is cut off, the m&t-BiVO₄/TiO₂-NTAs nanosystem no longer generates photoinduced e^-h^+ pairs. Atmospheric O₂ molecules can be adsorbed and activated by the V_o vacancy sites to produce reactive oxygen species (O_2^- and OH) (i.e., $O_2 + e^-_{CB} \rightarrow O_2^-$, $O_2^- + 2e^-_{CB} + 2H^+ \rightarrow OH + OH^-$) [113], and can also serve as CT channels to deplete the excessive e^-_{CB} in the CB, which is ascribed to the E_{CB} level position of m&t-BiVO₄, which is more negative than the reduction potential of O_2/O_2^- (-0.33 eV vs. NHE). Moreover, atmospheric OH⁻ in water molecules could be oxidized by the h^+_{VB} in the VB of TiO₂ to yield OH ($OH^- + h^+_{VB} \rightarrow OH$), benefiting from the E_{VB} potential position of the TiO₂ NTAs ($+2.9$ eV vs. NHE), which is more positive than that of OH⁻/OH ($+1.99$ eV vs. NHE). The transient CT process between the t-BiVO₄/m-BiVO₄/TiO₂-NTAs nano-heterojunctions introduces adequate V_o and V_v defects, which lead to large increases in the charge carrier concentrations and strong electronic perturbations around the vacancy defects [23,113], which induce upward shifts in the E_{CB} and E_{VB} potential sites and enable a large ΔE_C and ΔE_V , which can speed up the migration of the photoexcited carriers. By combining the NTRT-PL spectra for the as-synthesized m&t-BiVO₄/TiO₂-NTAs specimens with varied BiVO₄ NP deposition amounts in Figure 11a–c, we can see that there were almost identical transient PL peaks sited at 3.1 eV, 2.9 eV, and 2.4 eV, which resulted from the direct radiative recombination transition of the photogenerated carrier NBE between the CB and VB for TiO₂, t-BiVO₄, and m-BiVO₄, respectively. Simultaneously, we could clearly discern four NTRT-PL bands, including Region I (from 2.31 eV to 2.12 eV), Region II (from 2.05 eV to 1.91 eV), Region III (from 1.83 eV to 1.77 eV), and Region IV (from 2.77 eV to 2.46 eV), which stemmed from the indirect radiative recombination transition of the self-trapped electrons with V_o and V_v defect states in m&t-BiVO₄ and TiO₂, as depicted in Figure 9. In

the initial stage, a nanosystem is irradiated under 266 nm light ($t = 0$ ns), and plenty of e^-_{CB} are photoexcited and accumulate in the CB of BiVO_4 , with simultaneous generated holes in the VB, owing to the absorption of most of the incident photons by the surface-covered BiVO_4 NP films compared with the substrate of the TiO_2 NTAs. Reasonably, the radiative peak intensities centered at 2.9 eV and in Region I increased with the evolution time increase from 0 ns to 3 ns. Because the band potentials of the m&t- $\text{BiVO}_4/\text{TiO}_2$ -NTAs nanocomposites fit the requirements necessary to form a heterojunction with a straddling gap, the E_{CB} edge potential of t- BiVO_4 are more negative than those of m- BiVO_4 and TiO_2 , and the photogenerated high-energy electrons tend to transfer more freely from the CB of t- BiVO_4 toward the CB of m- BiVO_4 and TiO_2 NTAs, stimulated by the built-in electric field force. Thus, the transient PL peak intensities located at 2.4 eV, Regions II and III, increased as the recording time increased from 0 ns to 3 ns. The increasing consumption of the photoinduced e^-_{CB} in the CB of BiVO_4 , which resulted from the direct and indirect radiative recombination between the CB, vacancy defects, and h^+_{VB} in the VB during the last stage of the spectral recording time ($t = 4.5$ ns–6 ns), gave rise to the attenuated transient PL intensities sited at 2.9 eV and 2.4 eV, Regions I–III. Besides the E_{CB} potential for t- BiVO_4 , the E_{CB} edge of m- BiVO_4 also had a superior potential to that of the TiO_2 NTAs, and hence, could supply minor electron resistance pathways compared with the single m&t- BiVO_4 photoanode, representing the ΔE_c between the E_{CB} potential position for m- BiVO_4 and that for TiO_2 , and could act as a secondary built-in electric field force driven by Coulomb repulsive force, which accelerated the charge carrier transfer rate and migration from the CB of m&t- BiVO_4 to the adjacent. Rationally, the radiative peak intensities centered at 3.1 eV and in Region IV increased with the evolution time increase from 1.5 ns to 4 ns, while the transient PL peak intensities centered at 2.9 eV, 2.4 eV, Regions I–III, decreased at the NTRT-PL recording time which was 4 ns, originating from the elevated e^-_{CB} concentration of the CB in TiO_2 , and the weakened e^-_{CB} content in the CB of BiVO_4 , which was caused by the injection of photoproducted carriers from the CB of BiVO_4 to that of TiO_2 due to the formation of the m&t- $\text{BiVO}_4/\text{TiO}_2$ -NTAs nano-heterojunctions. At the end stage of the spectra recording ($t = 6$ ns), the transient PL peak emission centered at 3.1 eV and in Region IV gradually declined, mainly agreeing with the drastic decrease in the e^-_{CB} concentration in the CB of the TiO_2 NTAs through PL radiative recombination, as depicted in Figure 11a–c. The NTRT-PL intensities of the as-synthesized m&t- $\text{BiVO}_4/\text{TiO}_2$ -NTAs nano-heterojunctions increased with the increase in the hydrothermal deposition time from 5 h to 20 h, which is intimately connected to the concentration of the photogenerated charge carrier radiative recombination, which is dependent on the decorated amount of m&t- BiVO_4 NPs. However, the m&t- $\text{BiVO}_4/\text{TiO}_2$ -NTAs-10 specimen evinced the strongest transient PL intensity compared with those for all the other samples, which elucidates the concerted interaction between the deposited amount and the deposition time and V_o defect content mediated by the prepared pH value, which induced the discrepancy in the $\Delta E_c/\Delta E_v$ among the as-formed specimens, and which was identical to the 0.88 eV/1.13 eV, 1.05 eV/1.30 eV, and 0.94 eV/1.19 eV for the different BiVO_4 hydrothermal deposition contents (5 h, 10 h, and 20 h, respectively).

We recorded the PL decay profiles of the as-prepared specimens in Figure 15 by exciting the specimens with 375 nm laser pulses. We collected the PL decay trace at 678 nm (ca. 1.8 eV) for the plain BiVO_4 film sample, and we conducted the other PL-decay traces at 447 nm (ca. 2.8 eV), which originated from the e^-_{CB} trapped in the V_o defect indirect radiative recombination transition to the h^+_{VB} in BiVO_4 and TiO_2 , respectively. When irradiated by UVC light, the staggered band offset consequently induces a built-in electric field in the m&t- BiVO_4 and m&t- $\text{BiVO}_4/\text{TiO}_2$ -NTAs nano-heterojunction specimens, which drive the photogenerated electron injection into the CBs of BiVO_4 and TiO_2 . These photogenerated e^-_{CB} preferentially transfer to the V_o defect levels, which results in a substantial variation in the PL decay kinetics. By comparing the emission decay profiles for the pristine TiO_2 -NTAs, plain m&t- BiVO_4 films, and TiO_2 -NTAs decorated with different

BiVO₄ NP amounts, we can obtain the penetrating information for interpreting the fate of the charge carriers between the relevant specimens.

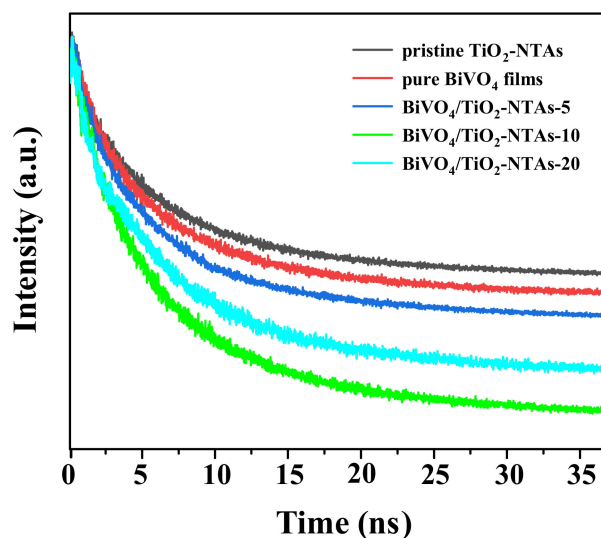


Figure 15. Time-resolved PL spectra of pure TiO₂-NTAs, plain BiVO₄ films, and m&t-BiVO₄/TiO₂-NTAs with various BiVO₄ NPs hydrothermal-deposited times, respectively.

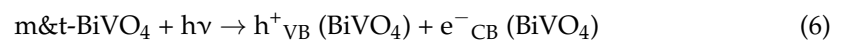
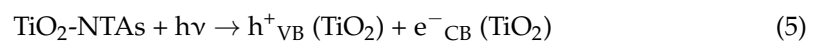
The lifetime of a carrier can be probed from the TRPL spectrum, and it complies with the biexponential rate law: $I(\tau) = A_1 \exp(-\tau/\tau_1) + A_2 \exp(-\tau/\tau_2)$ [114], where τ_1 and τ_2 are the fast and slow components, respectively, which originate from defect-induced nonradiative recombination and radiative recombination, respectively. Both A_1 and A_2 correspond to the decay amplitude [115]. We used the formula $\tau_{\text{avg}} = (A_1 \tau_1^2 + A_2 \tau_2^2) / (A_1 \tau_1 + A_2 \tau_2)$ to calculate the average lifetime of a carrier (τ_{avg}). As detailed in Table 7, the τ_{avg} values were 4.99 ns, 4.53 ns, 4.29 ns, 3.86 ns, and 4.06 ns for the pristine TiO₂-NTAs, plain m&t-BiVO₄ films, and m&t-BiVO₄/TiO₂-NTAs with BiVO₄ NP hydrothermal preparation times of 5 h, 10 h, and 20 h, respectively. The magnitude order of the τ_{avg} for the as-obtained specimens accords well with that previously reported [116,117], and it has consistently corroborated the validity of the simplified kinetics model considered for the synergistic effect between the hydrothermal deposition content and V_o defect concentration in mediating the CT of m&t-BiVO₄/TiO₂-NTAs heterojunction nano-hybrids. Evidently, all the specimens with the characteristic heterostructure indicated shortened τ_{avg} values relative to the pristine TiO₂-NTAs and single BiVO₄ films, and especially for the m&t-BiVO₄/TiO₂-NTAs sample with a deposition time of 10 h, which possessed the shortest τ_{avg} value (3.86 ns), intimately stemming from the highest band-offset values (ΔE_c and ΔE_v), which suggests that the shorter lifetime reflects the higher carrier injection efficiency [114]. Interestingly, the two dominant benefits that are expected from BiVO₄ NP incorporation (i.e., separation and fast charge transport) have compatible effects on the CT rate. We also analyzed the interfacial CT kinetics for the BiVO₄/TiO₂-NTAs type-II nano-heterojunctions, presuming that the heterojunction interfaces between BiVO₄ and TiO₂ were accountable for the observed reduced carrier lifetime. We can evaluate the CT rate constant (k_{ct}) by the following equation: $k_{\text{ct}} (* \rightarrow \text{TiO}_2) = 1/\tau_{\text{avg}} (*/\text{TiO}_2) - 1/\tau_{\text{avg}} (\text{plain TiO}_2)$, where * represents the BiVO₄, which is the alternative semiconductor forming a heterostructure. The calculated k_{ct} values were $3.27 \times 10^7 \text{ s}^{-1}$, $5.86 \times 10^7 \text{ s}^{-1}$, and $4.59 \times 10^7 \text{ s}^{-1}$ for m&t-BiVO₄/TiO₂-NTAs with diverse BiVO₄ deposition times of 5 h, 10 h, and 20 h, respectively. The variation tendencies of the k_{ct} values were proportional to the changing trends of the VB offset values, which presented the driving force to promote the photogenerated h^+_{VB} transfer from the VB of TiO₂ to the VB of the adjacent BiVO₄ because the carrier radiative lifetime of TRPL is directly dependent on the recombination lifetime of the minority carriers in nano-heterojunctions. Simultaneously, the k_{ct} value of the m&t-BiVO₄/TiO₂-NTAs-10 specimen was higher than that of the others, which indicates that the enlarged band offset (ΔE_c and ΔE_v) associated

with the V_o defect concentration induces a stronger built-in field force, which achieved the most effective charge spatial separation and active charge-transport injection of the photoinduced $e^-_{CB} - h^+_{VB}$ pairs on the different sides of the m&t-BiVO₄/TiO₂-NTAs heterojunction, and promoted a great number of the e^-_{CB} of TiO₂ and h^+_{VB} of BiVO₄ to participate in the redox reaction.

Table 7. Average lifetime of PL (τ_{avg}) for pristine TiO₂-NTAs and BiVO₄/TiO₂-NTAs nanoheterojunctions with different BiVO₄ hydrothermal-depositing times 5 h, 10 h, and 20 h, respectively.

Sample Codes	λ_{ex} (nm)	λ_{em} (eV)	τ_1 (ns)	$A_1/(A_1 + A_2)$ (%)	τ_2 (ns)	$A_2/(A_1 + A_2)$ (%)	τ_{avg} (ns)
pristine TiO ₂ -NTAs	375	2.8	2.33	54.0	6.16	46.0	4.99
plain BiVO ₄ films	375	1.8	2.38	52.8	5.56	47.2	4.53
m&t-BiVO ₄ /TiO ₂ -NTAs-5	375	2.8	2.35	60.1	5.53	39.9	4.29
m&t-BiVO ₄ /TiO ₂ -NTAs-10	375	2.8	2.21	42.8	4.47	57.2	3.86
m&t-BiVO ₄ /TiO ₂ -NTAs-20	375	2.8	2.31	56.5	5.09	43.5	4.06

We conducted photodegradation tests of the as-prepared nano-heterostructures to testify to the feasibility of the as-proposed transient CT mechanisms associated with the synergistic effect. We proposed the following chemical reactions:



We conducted the UV-visible photodegradation performance inspections for the TiO₂-NTAs-based heterostructure nanohybrids irradiated by a standard solar simulated light source. We positioned the as-prepared samples at the center of self-constructed reaction container using double-sided tape, aligning the MO dye adsorbed face upwards and towards the lamp. Initially, we performed the self-degradation test of the MO, aiming to eliminate the influence of the photobleaching effect. Thus, we present the adsorption process and photodegradation efficiency (η) results for the intrinsic self-decomposition of the MO, pristine TiO₂ NTAs, plain BiVO₄ films, and BiVO₄/TiO₂-NTAs nano-heterojunctions with different BiVO₄ NP hydrothermal deposition amounts, and with and without UV-visible lamp irradiation (photon-flux of 77.5 W/m²) for 180 min, respectively, in Figure 16. We detected the degraded MO solutions at 20 min intervals to calculate the dye concentration as per the equation [118]: $\eta = (C_i - C_f)/C_i \times 100\%$, where C_i and C_f are the initial and final concentrations of the MO solution after irradiation, respectively. The self-photodegradation of MO is not significant (less than 5%). In addition, the samples of pristine TiO₂-NTAs and pure BiVO₄ films exhibited less photodegradation activity (27% and 56%, respectively), compared with that of the BiVO₄/TiO₂-NTAs nanohybrids under UV-visible lamp irradiation, which was mainly ascribed to the inferior capability of the light absorption in the UV-visible region and the higher reduction potential position for the CB. Apparently, the m&t-BiVO₄/TiO₂-NTAs nano-heterojunctions manifested more elevated photodegradation performances for the MO dye than the single TiO₂ and BiVO₄ semiconductors due to the cooperative effect of the prolonged light-absorption scope and staggered energy-band structure of the type-II heterostructure, which can acquire more energetic carriers to participate in the oxidation-reduction reaction. Notably, the photodegradation characteristics

for the m&t-BiVO₄/TiO₂-NTAs specimens were enhanced from ca. 85% to ca. 97% with the BiVO₄ hydrothermal synthesized time increase from 5 h to 10 h, while the deposition time of the BiVO₄ further increased to 20 h, the η of which decreased to approximately 93%, which provides convincing evidence that the upgraded CT rate may be slightly more dominant than the carrier lifetime.

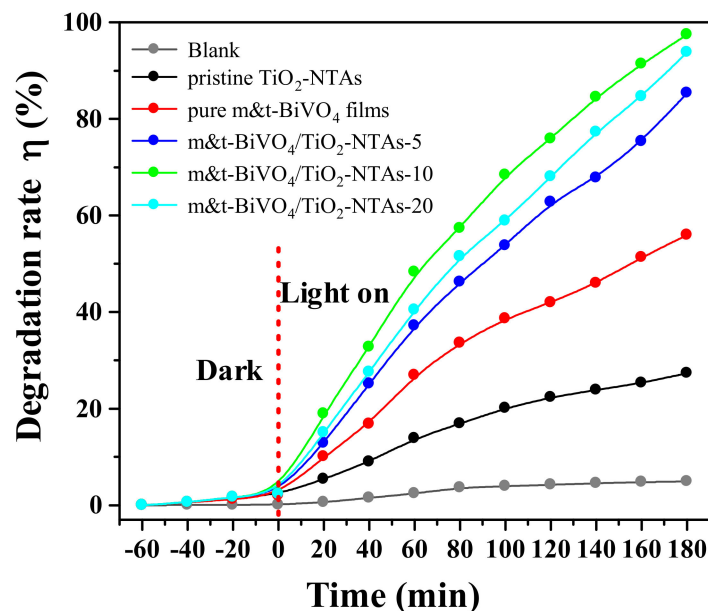


Figure 16. Adsorption process and photodegradation rate (η) of blank test, pristine TiO₂-NTAs, pure BiVO₄ films, and m&t-BiVO₄/TiO₂-NTAs with various BiVO₄ amounts (5 h, 10 h, and 20 h) under conditions of dark and UV-Visible light irradiation, respectively.

We used the pseudo-first-order kinetic model to quantitatively study the reaction dynamics. This model assumes that $\ln(C_0/C_t) = kt$ [119], where k is the reaction rate constant, C_0 is the initial concentration of the reactant, and C_t is the concentration of the reactant at time (t). In Figure 17, we explicitly show that m&t-BiVO₄/TiO₂-NTAs-10 has the maximum k value, which indicates the optimum photodegradation activity among the as-formed nano-heterojunctions.

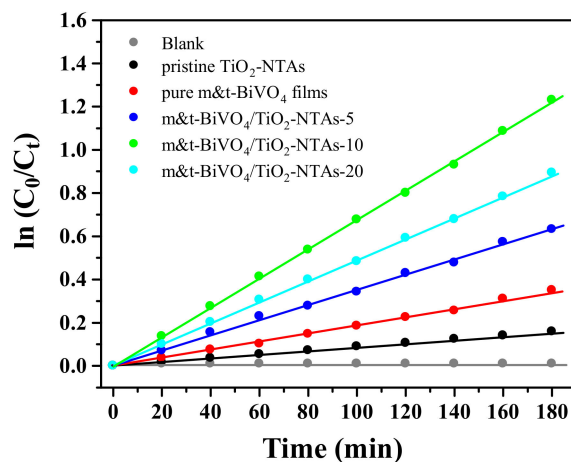


Figure 17. Pseudo-first-order kinetic analysis toward to MO degradation for blank test, pristine TiO₂-NTAs, pure BiVO₄ films, and BiVO₄/TiO₂-NTAs with different BiVO₄ deposited times under UV-Visible light irradiation, respectively.

Besides the degradation efficiency, the stability and usability of a photocatalyst are also critical factors that affect its feasibility. We successively conducted cyclic photodegradation

tests of the TiO_2 -NTAs-based nano-heterostructures under the same circumstances six times, as depicted in Figure 18.

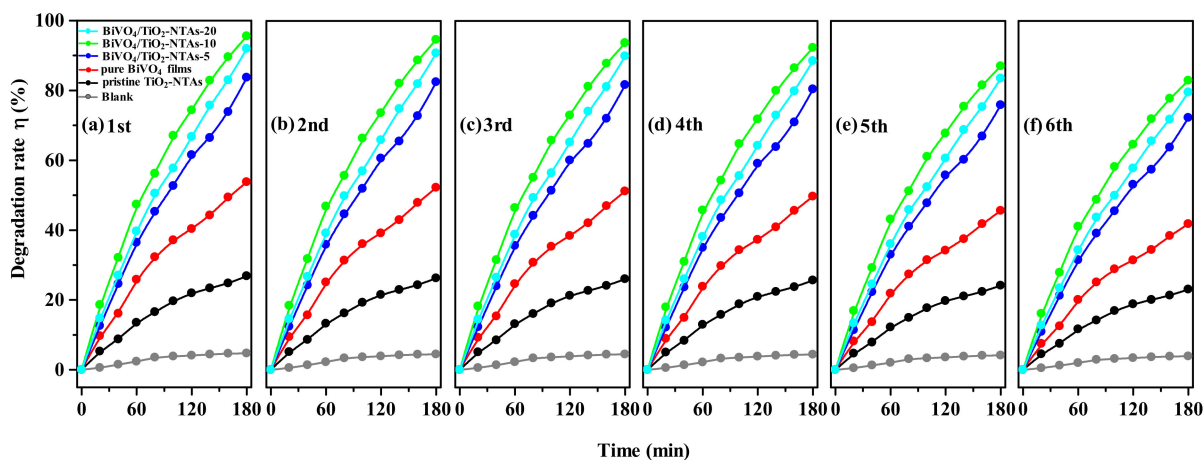


Figure 18. Cyclic photodegradation tests of the blank test, pristine TiO_2 -NTAs, pure BiVO_4 films, and $\text{BiVO}_4/\text{TiO}_2$ -NTAs with different BiVO_4 deposited amounts (5 h, 10 h, and 20 h) under UV-Visible light irradiation, (a) 1st, (b) 2nd, (c) 3rd, (d) 4th, (e) 5th, (f) 6th, respectively.

According to the results of the six cyclic tests, the degradation activities of the as-formed nanohybrids had a slight decrease, as expected, which was mainly ascribed to the inescapable weight loss, which only approached 15% for the maximal deterioration of the photodegradation performance. This highlights the fact that the as-obtained m&t- $\text{BiVO}_4/\text{TiO}_2$ -NTAs nano-heterojunctions had comparatively excellent photodegradation stabilities.

The purpose of the free-radical-trapping experiments was to determine which substances were reactive, such as h^+ , OH , and O_2^- , as well as which of them undertakes the primary role for the photodegradation towards MO dye, as exhibited in Figure 19.

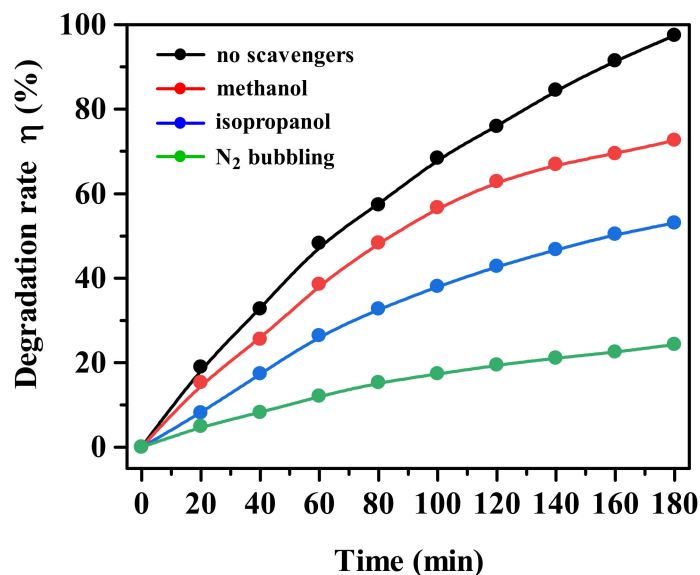


Figure 19. Photodegradation rate η of MO dye for the sample of m&t- $\text{BiVO}_4/\text{TiO}_2$ -NTAs-10 without and with the presence of various scavengers irradiated by UV-Visible light, respectively.

The η value of m&t- $\text{BiVO}_4/\text{TiO}_2$ -NTAs-10 was ca. 97% without radical scavengers, and the η values were ca. 73% and ca. 53% with methanol and IPA, respectively. Furthermore, we continuously injected the high-purity N_2 throughout the degradation reaction, with the aim of eliminating the dissolved O_2 and inhibiting the generation of O_2^- . The removal rate

for the MO was only ca. 24%, compared with the 97% under normal atmospheric conditions. Thus, both the OH and O_2^- radical groups are the collective reactive species involved in the degradation process, and O_2^- especially plays a dominant role in the reaction, which is strongly dependent on the number of V_o defects.

The oxidase-mimicking ability of $BiVO_4/TiO_2$ -NTAs nano-hybrids makes them an optimal choice of biosensing platforms for accurately determining the GSH levels. We present the GSH detection mechanism of the m&t- $BiVO_4/TiO_2$ -NTAs nano-heterojunctions in Figure 20. Under the excitation of simulated solar light, $BiVO_4$ and TiO_2 simultaneously absorb photons to generate $e^-_{CB}-h^+_{VB}$ pairs. Owing to the existence of the stepped-energy-band heterostructure, photoinduced e^-_{CB} can quickly transfer from the CB of $BiVO_4$ to the CB of TiO_2 , and then transfer to the external circuit. At the same time, the photoexcited h^+_{VB} migrate from the VB of TiO_2 to the VB of $BiVO_4$, driven by the force of the built-in electric field between $BiVO_4$ and TiO_2 . The direction of the built-in electric field is the same as that of the applied positive bias (0.5 V vs. Ag/AgCl), pointing from the TiO_2 to the $BiVO_4$. During the CT process, GSH can be oxidized to glutathione disulfide (GSSG), trapped by the holes in the VB of $BiVO_4$ and restraining the rapid recombination of $e^- - h^+$ pairs, which result in the substantial promotion of the photocurrent response compared with the transient I-t tests in Figure 8a. Therefore, the relationship between the GSH concentration and amplified photocurrent effect forms the basis of the biosensing function.

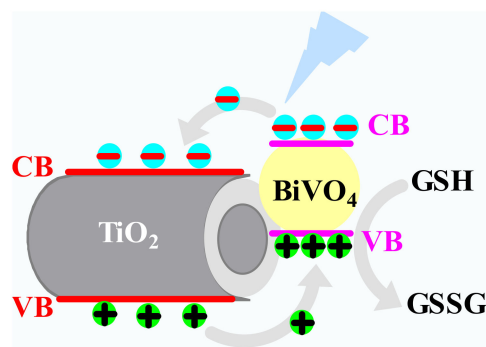


Figure 20. Mechanism diagram of the photoelectrochemical biosensing for GSH detection.

We quantitatively tested the constructed m&t- $BiVO_4/TiO_2$ -NTAs nano-heterojunctions for PEC biosensing in GSH solutions of various concentrations (0 μ M–500 μ M), and we recorded the concentration-current curves in 0.1 M PBS solution (pH 7.0) at the potential of 0.5 V (vs. Ag/AgCl) under simulated sunlight irradiation, as exhibited in Figure 21a. The photocurrent responses of the as-synthesized specimens gradually increased with the increase in the GSH concentration, and the photocurrent density of m&t- $BiVO_4/TiO_2$ -NTAs-10 was substantially higher than that of the m&t- $BiVO_4/TiO_2$ -NTAs-5 and m&t- $BiVO_4/TiO_2$ -NTAs-20 with the increase in the GSH concentration, confirming that the former has a superior photoinduced carrier CT efficiency and separation ability to the others, which is mainly due to the greater values of the ΔE_c and ΔE_v for m&t- $BiVO_4/TiO_2$ -NTAs-10 mediated by the synergistic effect. In addition, the photocurrent response of m&t- $BiVO_4/TiO_2$ -NTAs-10 had an excellent linear relationship with the GSH concentration ($R^2 = 0.9889$), with a linear range from 0 to 500 μ M, as shown in Figure 22b. This upper detection limit is more pertinent to detecting GSH in biological specimens because the cellular GSH concentration is at mM levels [120]. Simultaneously, the PEC biosensing performance for m&t- $BiVO_4/TiO_2$ -NTAs-10 showed a limit of detection (LOD) of 2.6 μ M (a signal-to-noise ratio of 3), with a sensitivity of 960 $mA\ cm^{-2}\ M^{-1}$, which was 1.92-fold and 1.38-fold greater than those for the m&t- $BiVO_4/TiO_2$ -NTAs-5 and m&t- $BiVO_4/TiO_2$ -NTAs-20 specimens, respectively.

We review the analysis performance of the GSH using m&t- $BiVO_4/TiO_2$ -NTAs heterostructure nano-hybrids in this work and other modified materials found in the literature in Table 8. The linear response range was wider than those of the colorimetric biosens-

ing, fluorescence biosensor, and other PEC methods. The m&t-BiVO₄/TiO₂ NTAs also displayed a lower detection limit for GSH compared with the fluorimetry and other PEC methods. Most important of all, the proposed BiVO₄/TiO₂-NTAs nano-heterostructure PEC biosensing approach is characterized by excellent stability and selectivity.

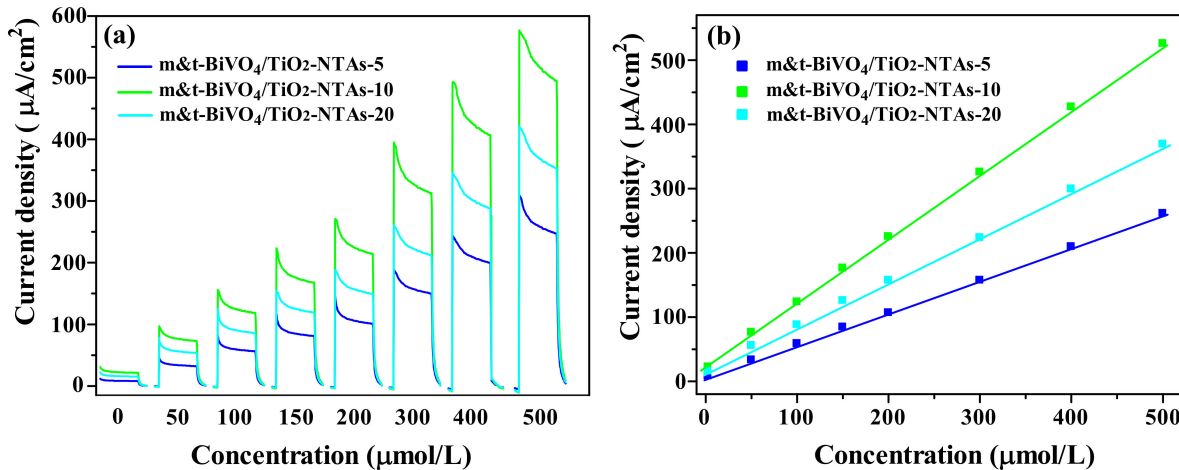


Figure 21. (a) Photocurrent performance of the m&t-BiVO₄/TiO₂-NTAs type-II heterostructure nanocomposites with various BiVO₄ NPs hydrothermal-deposited times in the presence of 0, 50, 100, 150, 200, 300, 400, and 500 μM GSH (from left to right) in 0.1 M PBS solution (pH 7.0) at the potential of 0.5 V irradiated by simulated sunlight, respectively; (b) the plots of m&t-BiVO₄/TiO₂-NTAs heterojunction nanoelectrodes with various BiVO₄ NPs deposition times 5 h, 10 h, and 20 h with linear relationship toward photocurrent density and concentration of GSH, respectively.

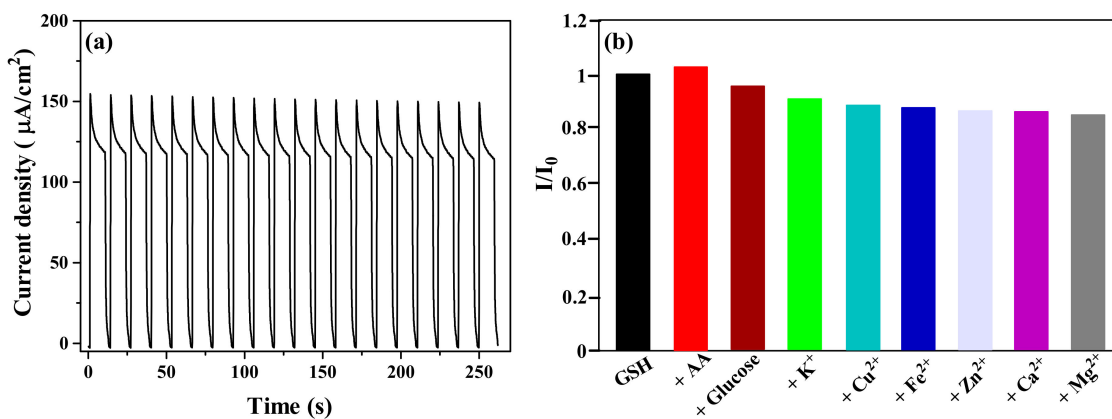


Figure 22. (a) Time-based photocurrent performance for the sample of m&t-BiVO₄/TiO₂-NTAs-10 irradiated by several cycles in 0.1 M PBS solution containing 100 μM GSH at the potential of 0.5 V (vs. Ag/AgCl) under simulated sunlight irradiation; (b) photocurrent ratio I/I_0 of the m&t-BiVO₄/TiO₂-NTAs-10 electrode in 0.1 M PBS solution containing 200 μM GSH with the successive addition of different interfering substances (the concentration of all other interfering species is 200 μM).

Table 8. Linear range and limit of detection (LOD) comparison of various methods for detecting GSH.

Sensor Type	Sensing Method	Linear Range (μM)	LOD (μM)	Ref.
BSA-AuNP@ZnCo ₂ O ₄	Colorimetric biosensing	0.5–15	0.0885	[121]
CuPd@H-C ₃ N ₄	Colorimetric biosensing	2–40	0.58	[122]
In ₂ O ₃ /In ₂ S ₃	PEC biosensing	1–100	0.82	[123]
N, S-Cdots-MnO ₂	fluorimetry	0–250	28.5	[124]
Bi ₂ S ₃ /TiO ₂ -NTAs	PEC biosensing	15–200	7	[125]
m&t-BiVO ₄ /TiO ₂ -NTAs	PEC biosensing	0–500	2.6	This work

To be effective, PEC biosensors should possess good stability and selectivity. We chose the m&t-BiVO₄/TiO₂-NTAs-10 specimen as the candidate for the stability and selectivity testing, as it has the optimal PEC activity among all the as-fabricated nanohybrids. We evaluated the photoexcited biosensing stability of the selected sample by measuring the time-based photocurrent response under several on/off irradiation cycles in a 0.1 M PBS solution containing 100 μM GSH at a potential of 0.5 V (vs. Ag/AgCl), irradiated by simulated sunlight irradiation. Within 260 s, the detection process of the nano-heterojunction had cycled 20 times, and as exhibited in Figure 22a, there was almost no decay on the photocurrent and 96.5% of its initial value was retained, which demonstrates that the BiVO₄/TiO₂-NTAs electrode had the desirable stability in the GSH detection. For probing the selectivity of the constructed nano-heterostructure photoelectrode, we adopted the ratio of the photocurrent intensity (I/I_0) to characterize the effects of a series of interfering substances on the photocurrent. I and I_0 represent the photocurrents before and after the addition of other interferents, respectively. For the characterization, we used metal ions (K⁺, Cu²⁺, Fe²⁺, Zn²⁺, Ca²⁺, and Mg²⁺), glucose, and ascorbic acid (AA). As displayed in Figure 22b, we did not observe any salient photocurrent variation with the successive addition of 200 μM AA, glucose, and other metal ions into the electrolyte containing 200 μM GSH. Among them, AA is a good electron donor and can be photocatalytically oxidized by the as-prepared nano-heterojunctions, and AA also caused the photocurrent to slightly increase, but it had little effect on the experimental results. Eventually, we verified the biosensing stability of the m&t-BiVO₄/TiO₂-NTAs photoelectrode via intermittent photocurrent response tests.

We present the graphical sensitivity vs. time relations of the as-prepared specimens at room temperature in Figure 23. The parameter sensitivity (S) for gas-sensing can be defined as follows [126]: $S = I_g/I_a$, where I_g is the experimentally recorded stable current values during the targeted gas flow, and I_a is the recorded stable current during the air gas flow. The response time (τ_{res}) is defined as the time to reach 90% of the final equilibrium value. When the NH₃ permeation reached $t = 200$ s, the S values were exponentially increased, as expected, while they were exponentially decreased when the air injection reached $t = 850$ s. Simultaneously, there were smaller S values (ca. 0.5 and 0.8) for the gas-sensing of the pristine TiO₂ NTA and pure BiVO₄ film sensors owing to their larger electronic transfer impedances and narrower light-absorption scopes, which led to lower photoexcited current responses. The S value increased from ca. 1.8 to ca. 2.4 with the increase in the BiVO₄ hydrothermal deposition times from 5 h to 10 h; however, the S value decreased to ca. 2.2 with the increase in the of BiVO₄ preparation time to 20 h, which are consistent with the abovementioned observed trends in the photodegradation and PEC biosensing. In addition, the τ_{res} values for the pristine TiO₂ NTAs and plain BiVO₄ films were 307 s and 302 s, respectively. As a comparison, the τ_{res} of the m&t-BiVO₄/TiO₂-NTAs-5 sample was about 290 s towards the sensing of NH₃ gas, while those for the m&t-BiVO₄/TiO₂-NTAs-10 and m&t-BiVO₄/TiO₂-NTAs-20 samples were around 250 s and 271 s, respectively. The gas-sensing performances of the sensitivity and response speed for the m&t-BiVO₄/TiO₂-NTAs nano-heterostructure are superior to those of the individual BiVO₄ and TiO₂ semiconductors. The specimen of m&t-BiVO₄/TiO₂-NTAs-10, especially, is the ideal platform for gas-sensing, possessing a higher sensitivity and faster response speed in comparison with those of the m&t-BiVO₄/TiO₂-NTAs-5 and m&t-BiVO₄/TiO₂-NTAs-20.

Combined with the obtained results, we propose a reasonable theory to explain the gas-sensing mechanism toward NH₃. The conductivity of nano-heterostructures is proportional to the concentration of conducting electrons. In the beginning, the atmospheric O₂ can be converted to O₂⁻, attaching to the active sites of the V_o defects in nano-heterojunctions, which leads to a reduced concentration of carriers. With the injection of NH₃ gas, reductive NH₃ molecules can react with O₂⁻ (i.e., 4NH₃ (gas) + 3 O₂⁻ (adsorption) → 6H₂O (gas) + 2N₂ (gas) + 3e⁻), liberating the electrons as free charges and increasing the conductivity of the nano-heterostructures, and the electrically neutral N₂ gas will be released back to the ambience. The increased concentration of e⁻_{CB} due to the exposure of the

hetero-nanosystem to NH_3 gas is a result of the electron-donating properties of analyte gas. Specifically, the m&t- $\text{BiVO}_4/\text{TiO}_2$ -NTAs heterostructure nanocomposites can inject redundant electrons into the CB of TiO_2 from the CB of BiVO_4 irradiated by UV–vis light, which facilitates the formation of O_2^- . The m&t- $\text{BiVO}_4/\text{TiO}_2$ -NTAs-10 sample manifested the best performances for photodegradation and gas-sensing, which are tightly associated with the O_2^- concentration, which is mainly attributed to the number of V_o defect active sites and the superior capacity of CT associated with the greater ΔE_c and ΔE_v values.

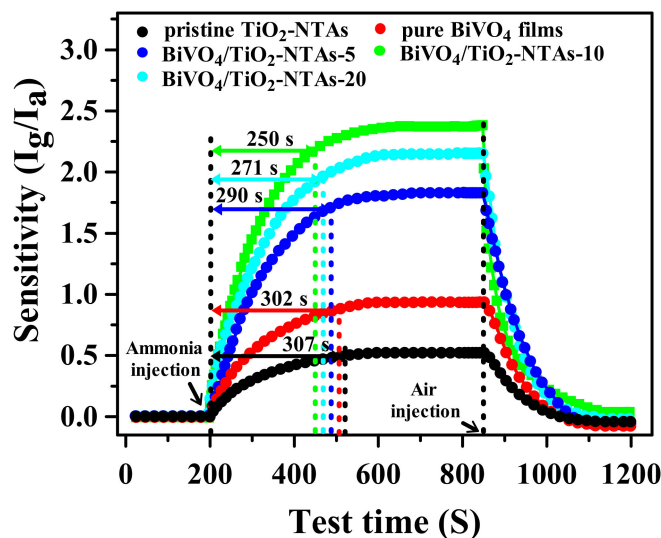


Figure 23. Sensitivity of pristine TiO_2 -NTAs, pure BiVO_4 films and m&t- $\text{BiVO}_4/\text{TiO}_2$ -NTAs nano-hybrids with different BiVO_4 NPs depositing amounts as a function of time, respectively.

4. Conclusions

In conclusion, we constructed the m&t- $\text{BiVO}_4/\text{TiO}_2$ -NTAs type-II nano-heterojunctions via m&t- BiVO_4 NPs integrated with the ordered arrangement of TiO_2 NTAs using the low-cost hydrothermal-deposition approach. The as-synthesized m&t- $\text{BiVO}_4/\text{TiO}_2$ -NTAs nano-hybrids exhibited dramatically improved photodegradation, PEC biosensing, and NH_3 gas-sensing performances compared with the single semiconductor under UV–visible irradiation, as expected, which is consistent with the variation trend of the PEC activity tests, which is mainly ascribed to the positive synergistic effect between the content ratio of the m&t- BiVO_4 related to the hydrothermal preparation time and the number of V_o defects mediated by the pH value, which induce the uplifted band offset and promote the exposed reaction active sites related to V_o defects. We verified the deduction by the probing results of the NTRT-PL and TRPL spectra, correspondingly proposing semi-qualitative and semi-quantitative analyses for the interfacial CT dynamics process, which demonstrates the promotion of the separation of the photoinduced e^-h^+ pairs and elevated charge injection efficiency for the as-obtained nano-heterojunctions. Thus, it is expectable that the m&t- $\text{BiVO}_4/\text{TiO}_2$ -NTAs nano-heterojunctions not only provide in-depth comprehension for the interfacial CT process between different photocatalysts, but also contributes new insight into the design of devices for PEC biosensing and NH_3 gas-sensing with superior performances.

Author Contributions: Conceptualization, Z.S.; methodology, Y.Z. and M.Z.; formal analysis, M.Z.; investigation, J.C. and Y.Z.; data curation, J.C.; writing—original draft, Z.S.; writing—review and editing, Z.S.; funding acquisition, Y.P. and L.S. All authors have read and agreed to the published version of the manuscript.

Funding: Supported the National Key Research and Development Program of China (Grant No. 2021YFB3802100) and Intercollegiate cooperation project of Liaoning provincial colleges and universities. (Project No. XJXM2020005).

Conflicts of Interest: The authors declare no conflict of interest.

References

1. Masoumi, Z.; Tayebi, M.; Kolaei, M.; Lee, B.-K. Unified surface modification by double heterojunction of MoS₂ nanosheets and BiVO₄ nanoparticles to enhance the photoelectrochemical water splitting of hematite photoanode. *J. Alloys Compd.* **2022**, *890*, 161802. [[CrossRef](#)]
2. He, Y.; Chen, K.; Leung, M.K.H.; Zhang, Y.; Li, L.; Li, G.; Xuan, J.; Li, J. Photocatalytic fuel cell—A review. *Chem. Eng. J.* **2022**, *428*, 131074. [[CrossRef](#)]
3. Fujishima, A.; Honda, K. Electrochemical Photolysis of Water at a Semiconductor Electrode. *Nature* **1972**, *238*, 37–38. [[CrossRef](#)]
4. Tudu, B.; Nalajala, N.; Saikia, P.; Gopinath, C.S. Cu–Ni bimetal integrated TiO₂ thin film for enhanced solar hydrogen generation. *Solar RRL* **2020**, *4*, 1900557. [[CrossRef](#)]
5. Hot, J.; Frayret, J.; Sonois-Mazars, V.; Ringot, E. From hexafluorotitanate waste to TiO₂ powder: Characterization and evaluation of the influence of synthesis parameters by the experimental design method. *Adv. Powder Technol.* **2022**, *33*, 103472. [[CrossRef](#)]
6. Han, M.; Zhang, Z.; Li, B.; Hu, X.; Wang, Z. Combined heterostructures between Bi₂S₃ nanosheets and H₂-treated TiO₂ nanorods for enhanced photoelectrochemical water splitting. *Appl. Surf. Sci.* **2022**, *598*, 153850. [[CrossRef](#)]
7. Wang, Q.; Hisatomi, T.; Katayama, M.; Takata, T.; Minegishi, T.; Kudo, A.; Yamada, T.; Domen, K. Particulate photocatalyst sheets for Z-scheme water splitting: Advantages over powder suspension and photoelectrochemical systems and future challenges. *Faraday Discuss.* **2017**, *197*, 491–504. [[CrossRef](#)] [[PubMed](#)]
8. Gopinath, C.S.; Nalajala, N. A scalable and thin film approach for solar hydrogen generation: A review on enhanced photocatalytic water splitting. *J. Mater. Chem. A* **2021**, *9*, 1353–1371. [[CrossRef](#)]
9. Fan, L.; Liang, G.; Zhang, C.; Fan, L.; Yan, W.; Guo, Y.; Shuang, S.; Bi, Y.; Li, F.; Dong, C. Visible-light-driven photoelectrochemical sensing platform based on BiOI nanoflowers/TiO₂ nanotubes for detection of atrazine in environmental samples. *J. Hazard. Mater.* **2021**, *409*, 124894. [[CrossRef](#)]
10. Fan, L.; Zhang, C.; Liang, G.; Yan, W.; Guo, Y.; Bi, Y.; Dong, C. Highly sensitive photoelectrochemical aptasensor based on MoS₂ quantum dots/TiO₂ nanotubes for detection of atrazine. *Sens. Actuators B Chem.* **2021**, *334*, 129652. [[CrossRef](#)]
11. Sayahi, H.; Aghapoor, K.; Mohsenzadeh, F.; Morad, M.M.; Darabi, H.R. TiO₂ nanorods integrated with titania nanoparticles: Large specific surface area 1D nanostructures for improved efficiency of dye-sensitized solar cells (DSSCs). *Sol. Energy* **2021**, *215*, 311–320. [[CrossRef](#)]
12. Kong, Y.; Sun, M.; Hong, X.; Wang, Y.; Umar, A. The co-modification of MoS₂ and CdS on TiO₂ nanotube array for improved photoelectrochemical properties. *Ionics* **2021**, *27*, 4371–4381. [[CrossRef](#)]
13. Arifin, K.; Yunus, R.M.; Minggu, L.J.; Kassim, M.B. Improvement of TiO₂ nanotubes for photoelectrochemical water splitting: Review. *Int. J. Hydrog. Energy* **2021**, *46*, 4998–5024. [[CrossRef](#)]
14. Xie, X.; Li, L.; Ye, S.; Zhang, Q.; Chen, X.; Huang, X. Photocatalytic degradation of ethylene by TiO₂ nanotubes/ reduced graphene oxide prepared by gamma irradiation. *Radiat. Phys. Chem.* **2020**, *169*, 108776. [[CrossRef](#)]
15. Basavarajappa, P.S.; Patil, S.B.; Ganganagappa, N.; Reddy, K.R.; Raghu, A.V.; Reddy, C.V. Recent progress in metal-doped TiO₂, non-metal doped/codoped TiO₂ and TiO₂ nanostructured hybrids for enhanced photocatalysis. *Int. J. Hydrog. Energy* **2019**, *45*, 7764–7778. [[CrossRef](#)]
16. Divyasri, Y.V.; Reddy, N.L.; Lee, K.; Sakar, M.; Rao, V.N.; Venkatramu, V.; Shankar, M.V.; Reddy, N.C.G. Optimization of N doping in TiO₂ nanotubes for the enhanced solar light mediated photocatalytic H₂ production and dye degradation. *Environ. Pollut.* **2021**, *269*, 116170. [[CrossRef](#)] [[PubMed](#)]
17. Solly, M.M.; Ramasamy, M.; Poobalan, R.K.; Ramanathan, R. Spin-Coated Bismuth Vanadate Thin Film as an Alternative Electron Transport Layer for Light-Emitting Diode Application. *Phys. Status Solidi* **2021**, *218*, 2000735. [[CrossRef](#)]
18. Liu, Y.; Liu, C.; Shi, C.; Sun, W.; Lin, X.; Shi, W.; Hong, Y. Carbon-based quantum dots (QDs) modified ms/tz-BiVO₄ heterojunction with enhanced photocatalytic performance for water purification. *J. Alloys Compd.* **2021**, *881*, 160437. [[CrossRef](#)]
19. Zou, Y.; Lu, M.; Jiang, Z.; Xu, L.; Liu, C.; Zhang, L.; Chen, Y. Hydrothermal synthesis of Zn-doped BiVO₄ with mixed crystal phase for enhanced photocatalytic activity. *Opt. Mater.* **2021**, *119*, 111398. [[CrossRef](#)]
20. Yang, J.W.; Park, I.J.; Lee, S.A.; Lee, M.G.; Lee, T.H.; Park, H.; Kim, C.; Park, J.; Moon, J.; Kim, J.Y.; et al. Near-complete charge separation in tailored BiVO₄-based heterostructure photoanodes toward artificial leaf. *Appl. Catal. B Environ.* **2021**, *293*, 120217. [[CrossRef](#)]
21. Bano, K.; Mittal, S.K.; Singh, P.P.; Kaushal, S. Sunlight driven photocatalytic degradation of organic pollutants using MnV₂O₆/BiVO₄ heterojunction: Mechanistic perception and degradation pathways. *Nanoscale Adv.* **2021**, *3*, 6446–6458. [[CrossRef](#)]
22. Meng, Q.; Zhang, B.; Yang, H.; Liu, C.; Li, Y.; Kravchenko, A.; Sheng, X.; Fan, L.; Li, F.; Sun, L. Remarkable synergy of borate and interfacial hole transporter on BiVO₄ photoanodes for photoelectrochemical water oxidation. *Mater. Adv.* **2021**, *2*, 4323–4332. [[CrossRef](#)]
23. Wang, J.; Guo, L.; Xu, L.; Zeng, P.; Li, R.; Peng, T. Z-scheme photocatalyst based on porphyrin derivative decorated few-layer BiVO₄ nanosheets for efficient visible-light-driven overall water splitting. *Nano Res.* **2021**, *14*, 1294–1304. [[CrossRef](#)]
24. Zhan, H.; Zhou, Q.; Li, M.; Zhou, R.; Mao, Y.; Wang, P. Photocatalytic O₂ activation and reactive oxygen species evolution by surface B–N bond for organic pollutants degradation. *Appl. Catal. B Environ.* **2022**, *310*, 121329. [[CrossRef](#)]

25. Tian, H.; Wu, H.; Fang, Y.; Li, R.; Huang, Y. Hydrothermal synthesis of m-BiVO₄/t-BiVO₄ heterostructure for organic pollutants degradation: Insight into the photocatalytic mechanism of exposed facets from crystalline phase controlling. *J. Hazard. Mater.* **2020**, *399*, 123159. [[CrossRef](#)] [[PubMed](#)]
26. Liu, Y.; Deng, P.; Wu, R.; Geioushy, R.A.; Li, Y.; Liu, Y.; Zhou, F.; Li, H.; Sun, C. BiVO₄/TiO₂ heterojunction with rich oxygen vacancies for enhanced electrocatalytic nitrogen reduction reaction. *Front. Phys.* **2021**, *16*, 53503. [[CrossRef](#)]
27. Fang, M.; Cai, Q.; Qin, Q.; Hong, W.; Liu, W. Mo-doping induced crystal orientation reconstruction and oxygen vacancy on BiVO₄ homojunction for enhanced solar-driven water splitting. *Chem. Eng. J.* **2021**, *421*, 127796. [[CrossRef](#)]
28. Chen, S.; Huang, D.; Xu, P.; Xue, W.; Lei, L.; Chen, Y.; Zhou, C.; Deng, R.; Wang, W. Topological transformation of bismuth vanadate into bismuth oxychloride: Band-gap engineering of ultrathin nanosheets with oxygen vacancies for efficient molecular oxygen activation. *Chem. Eng. J.* **2021**, *420*, 127573. [[CrossRef](#)]
29. Chen, H.; Li, J.; Yang, W.; Balaghi, S.E.; Triana, C.A.; Mavrokefalos, C.K.; Patzke, G.R. The Role of Surface States on Reduced TiO₂@BiVO₄ Photoanodes: Enhanced Water Oxidation Performance through Improved Charge Transfer. *ACS Catal.* **2021**, *11*, 7637–7646. [[CrossRef](#)]
30. Kumar, J.V.; Kavitha, G.; Arulmozhi, R.; Arul, V.; Abirami, N. Cyan color-emitting nitrogen-functionalized carbon nanodots (NFCNDs) from *Indigofera tinctoria* and their catalytic reduction of organic dyes and fluorescent ink applications. *RSC Adv.* **2021**, *11*, 27745–27756. [[CrossRef](#)]
31. Tayyebi, A.; Soltani, T.; Hong, H.; Lee, B.-K. Improved photocatalytic and photoelectrochemical performance of monoclinic bismuth vanadate by surface defect states (Bi_{1-x}VO₄). *J. Colloid Interface Sci.* **2018**, *514*, 565–575. [[CrossRef](#)] [[PubMed](#)]
32. Kang, Z.; Lv, X.; Sun, Z.; Wang, S.; Zheng, Y.-Z.; Tao, X. Borate and iron hydroxide co-modified BiVO₄ photoanodes for high-performance photoelectrochemical water oxidation. *Chem. Eng. J.* **2021**, *421*, 129819. [[CrossRef](#)]
33. Lian, X.; Zhang, J.; Zhan, Y.; Zhang, Y.; Yang, S.; Chen, Z.; Dong, Y.; Fang, W.; Yi, X. Engineering BiVO₄@Bi₂S₃ heterojunction by cosharing bismuth atoms toward boosted photocatalytic Cr(VI) reduction. *J. Hazard. Mater.* **2021**, *406*, 124705. [[CrossRef](#)] [[PubMed](#)]
34. Shao, Z.; Zhang, Y.; Yang, X.; Zhong, M. Au-Mediated Charge Transfer Process of Ternary Cu₂O/Au/TiO₂-NAs Nanoheterostructures for Improved Photoelectrochemical Performance. *ACS Omega* **2020**, *5*, 7503–7518. [[CrossRef](#)]
35. Shao, Z.; Liu, W.; Zhang, Y.; Yang, X.; Zhong, M. Insights on interfacial charge transfer across MoS₂/TiO₂-NTAs nanoheterostructures for enhanced photodegradation and biosensing&gas-sensing performance. *J. Mol. Struct.* **2021**, *1244*, 131240. [[CrossRef](#)]
36. Fan, L.; Liang, G.; Yan, W.; Guo, Y.; Bi, Y.; Dong, C. A highly sensitive photoelectrochemical aptasensor based on BiVO₄ nanoparticles-TiO₂ nanotubes for detection of PCB72. *Talanta* **2021**, *233*, 122551. [[CrossRef](#)]
37. Perini, J.A.L.; Tavella, F.; Neto, E.P.F.; Zanoni, M.V.B.; Ribeiro, S.J.L.; Giusti, D.; Centi, G.; Perathoner, S.; Ampelli, C. Role of nanostructure in the behaviour of BiVO₄-TiO₂ nanotube photoanodes for solar water splitting in relation to operational conditions. *Sol. Energy Mater. Sol. Cells* **2021**, *223*, 110980. [[CrossRef](#)]
38. Mohamed, N.A.; Arzaee, N.A.; Noh, M.F.M.; Ismail, A.F.; Safaei, J.; Sagu, J.S.; Johan, M.R.; Teridi, M.A.M. Electrodeposition of BiVO₄ with needle-like flower architecture for high performance photoelectrochemical splitting of water. *Ceram. Int.* **2021**, *47*, 24227–24239. [[CrossRef](#)]
39. Xu, X.; Lin, H.; Xiao, P.; Zhu, J.; Bi, H.; Carabineiro, S.A.C. Construction of Ag-bridged Z-scheme LaFe_{0.5}Co_{0.5}O₃/Ag₁₀/graphitic carbon nitride heterojunctions for photo-fenton degradation of tetracycline hydrochloride: Interfacial electron effect and reaction mechanism. *Adv. Mater. Interfaces* **2022**, *9*, 2101902. [[CrossRef](#)]
40. Hunge, Y.M.; Uchida, A.; Tominaga, Y.; Fujii, Y.; Yadav, A.A.; Kang, S.-W.; Suzuki, N.; Shitanda, I.; Kondo, T.; Itagaki, M.; et al. Visible Light-Assisted Photocatalysis Using Spherical-Shaped BiVO₄ Photocatalyst. *Catalysts* **2021**, *11*, 460. [[CrossRef](#)]
41. Wang, W.; Han, Q.; Zhu, Z.; Zhang, L.; Zhong, S.; Liu, B. Enhanced photocatalytic degradation performance of organic contaminants by heterojunction photocatalyst BiVO₄/TiO₂/RGO and its compatibility on four different tetracycline antibiotics. *Adv. Powder Technol.* **2019**, *30*, 1882–1896. [[CrossRef](#)]
42. Noor, M.; Sharmin, F.; Al Mamun, M.; Hasan, S.; Hakim, M.; Basith, M. Effect of Gd and Y co-doping in BiVO₄ photocatalyst for enhanced degradation of methylene blue dye. *J. Alloys Compd.* **2022**, *895*, 162639. [[CrossRef](#)]
43. Wang, A.; Wu, Q.; Han, C.; Yang, H.; Xue, X. Significant influences of crystal structures on photocatalytic removal of NO_x by TiO₂. *J. Photochem. Photobiol. A Chem.* **2021**, *407*, 113020. [[CrossRef](#)]
44. Fan, P.; Zhang, S.-T.; Xu, J.; Zang, J.; Samart, C.; Zhang, T.; Tan, H.; Salamon, D.; Zhang, H.; Liu, G. Relaxor/antiferroelectric composites: A solution to achieve high energy storage performance in lead-free dielectric ceramics. *J. Mater. Chem. C* **2020**, *8*, 5681–5691. [[CrossRef](#)]
45. Baral, B.; Reddy, K.H.; Parida, K.M. Construction of m-BiVO₄/t-BiVO₄ isotype heterojunction for enhanced photocatalytic degradation of norfloxacin and oxygen evolution reaction. *J. Colloid Interface Sci.* **2019**, *554*, 278–295. [[CrossRef](#)] [[PubMed](#)]
46. Cao, X.; Gu, Y.; Tian, H.; Fang, Y.; Johnson, D.; Ren, Z.; Chen, C.; Huang, Y. Microemulsion synthesis of ms/tz-BiVO₄ composites: The effect of pH on crystal structure and photocatalytic performance. *Ceram. Int.* **2020**, *46*, 20788–20797. [[CrossRef](#)]
47. Hajra, P.; Kundu, S.; Maity, A.; Bhattacharya, C. Facile photoelectrochemical water oxidation on Co²⁺-adsorbed BiVO₄ thin films synthesized from aqueous solutions. *Chem. Eng. J.* **2019**, *374*, 1221–1230. [[CrossRef](#)]
48. Zheng, Y.; Shi, J.; Xu, H.; Jin, X.; Ou, Y.; Wang, Y.; Li, C. The bifunctional Lewis acid site improved reactive oxygen species production: A detailed study of surface acid site modulation of TiO₂ using ethanol and Br⁻. *Catal. Sci. Technol.* **2022**, *12*, 565–571. [[CrossRef](#)]

49. Akshay, V.; Arun, B.; Mukesh, M.; Chanda, A.; Vasundhara, M. Tailoring the NIR range optical absorption, band-gap narrowing and ferromagnetic response in defect modulated TiO₂ nanocrystals by varying the annealing conditions. *Vacuum* **2021**, *184*, 109955. [[CrossRef](#)]
50. Omrani, N.; Nezamzadeh-Ejehieh, A. Photodegradation of sulfasalazine over Cu₂O-BiVO₄-WO₃ nano-composite: Characterization and experimental design. *Int. J. Hydrog. Energy* **2020**, *45*, 19144–19162. [[CrossRef](#)]
51. Razi, R.; Sheibani, S. Photocatalytic activity enhancement by composition control of mechano-thermally synthesized BiVO₄-Cu₂O nanocomposite. *Ceram. Int.* **2021**, *47*, 29795–29806. [[CrossRef](#)]
52. Zhao, S.; Chen, C.; Ding, J.; Yang, S.; Zang, Y.; Ren, N. One-pot hydrothermal fabrication of BiVO₄/Fe₃O₄/rGO composite photocatalyst for the simulated solar light-driven degradation of Rhodamine B. *Front. Environ. Sci. Eng.* **2021**, *16*, 36. [[CrossRef](#)]
53. Wang, L.; Cheng, B.; Zhang, L.; Yu, J. In situ irradiated XPS investigation on S-scheme TiO₂@ZnIn₂S₄ photocatalyst for efficient photocatalytic CO₂ reduction. *Small* **2021**, *17*, 2103447. [[CrossRef](#)]
54. Wang, Q.; Xiao, L.; Liu, X.; Sun, X.; Wang, J.; Du, H. Special Z-scheme Cu₃P/TiO₂ hetero-junction for efficient photocatalytic hydrogen evolution from water. *J. Alloys Compd.* **2022**, *894*, 162331. [[CrossRef](#)]
55. Wu, L.; Guo, C.; Feng, R.; Zhang, H.; Shi, N.; Li, Y.; Su, H.; Cui, X.; Song, F. Co-doping of P(V) and Ti(III) in leaf-architected TiO₂ for enhanced visible light harvesting and solar photocatalysis. *J. Am. Ceram. Soc.* **2021**, *104*, 5719–5732. [[CrossRef](#)]
56. Kim, M.; Yun, T.G.; Noh, J.; Song, Z.; Kim, H.; Kang, M.; Pyun, J. Laser-Induced Surface Reconstruction of Nanoporous Au-Modified TiO₂ Nanowires for In Situ Performance Enhancement in Desorption and Ionization Mass Spectrometry. *Adv. Funct. Mater.* **2021**, *31*, 2102475. [[CrossRef](#)]
57. Jiang, Z.; Qi, R.; Huang, Z.; Shangguan, W.; Wong, R.J.; Lee, A. Impact of methanol photomediated surface defects on photocatalytic H₂ production over Pt/TiO₂. *Energy Environ. Mater.* **2020**, *3*, 202–208. [[CrossRef](#)]
58. Chen, J.; Fu, Y.; Sun, F.; Hu, Z.; Wang, X.; Zhang, T.; Zhang, F.; Wu, X.; Chen, H.; Cheng, G.; et al. Oxygen vacancies and phase tuning of self-supported black TiO_{2-x} nanotube arrays for enhanced sodium storage. *Chem. Eng. J.* **2020**, *400*, 125784. [[CrossRef](#)]
59. Zhao, H.; Zalfani, M.; Li, C.-F.; Liu, J.; Hu, Z.-Y.; Mahdouani, M.; Bourguiga, R.; Li, Y.; Su, B.-L. Cascade electronic band structured zinc oxide/bismuth vanadate/three-dimensional ordered macroporous titanium dioxide ternary nanocomposites for enhanced visible light photocatalysis. *J. Colloid Interface Sci.* **2019**, *539*, 585–597. [[CrossRef](#)]
60. Zhong, H.; Gao, G.; Wang, X.; Wu, H.; Shen, S.; Zuo, W.; Cai, G.; Wei, G.; Shi, Y.; Fu, D.; et al. Ion irradiation inducing oxygen vacancy-rich NiO/NiFe₂O₄ Heterostructure for enhanced electrocatalytic water splitting. *Small* **2021**, *17*, 2103501. [[CrossRef](#)]
61. Zhao, X.; Wang, D.; Liu, S.; Li, Z.; Meng, J.; Ran, Y.; Zhang, Y.; Li, L. Bi₂S₃ nanoparticles densely grown on electrospun-carbon-nanofibers as low-cost counter electrode for liquid-state solar cells. *Mater. Res. Bull.* **2020**, *125*, 110800. [[CrossRef](#)]
62. Shaheer, A.M.; Thangavel, N.; Rajan, R.; Abraham, D.A.; Vinoth, R.; Devi, K.S.; Shankar, M.; Neppolian, B. Sonochemical assisted impregnation of Bi₂WO₆ on TiO₂ nanorod to form Z-scheme heterojunction for enhanced photocatalytic H₂ production. *Adv. Powder Technol.* **2021**, *32*, 4734–4743. [[CrossRef](#)]
63. Jiang, W.; An, Y.; Wang, Z.; Wang, M.; Bao, X.; Zheng, L.; Cheng, H.; Wang, P.; Liu, Y.; Zheng, Z.; et al. Stress-induced BiVO₄ photoanode for enhanced photoelectrochemical performance. *Appl. Catal. B Environ.* **2022**, *304*, 121012. [[CrossRef](#)]
64. Zhang, Z.; Huang, J.; Fang, Y.; Zhang, M.; Liu, K.; Dong, B. A Nonmetal Plasmonic Z-Scheme Photocatalyst with UV- to NIR-Driven Photocatalytic Protons Reduction. *Adv. Mater.* **2017**, *29*, 1606688. [[CrossRef](#)]
65. Li, L.; Mao, M.; She, X.; Yi, J.; He, M.; Pan, L.; Chen, Z.; Xu, H.; Li, H. Direct Z-scheme photocatalyst for efficient water pollutant degradation: A case study of 2D g-C₃N₄/BiVO₄. *Mater. Chem. Phys.* **2020**, *241*, 122308. [[CrossRef](#)]
66. Shi, L.; Lu, C.; Chen, L.; Zhang, Q.; Li, Y.; Zhang, T.; Hao, X. Piezocatalytic performance of Na_{0.5}Bi_{0.5}TiO₃ nanoparticles for degradation of organic pollutants. *J. Alloys Compd.* **2022**, *895*, 162591. [[CrossRef](#)]
67. Zhu, Z.; Hwang, Y.T.; Liang, H.C.; Wu, R.J. Prepared Pd/MgO/BiVO₄ composite for photoreduction of CO₂ to CH₄. *J. Chin. Chem. Soc.* **2021**, *68*, 1897–1907. [[CrossRef](#)]
68. Soomro, R.A.; Jawaid, S.; Kalawar, N.H.; Tunesi, M.; Karakuş, S.; Kilislioglu, A.; Willander, M. In-situ engineered mxene-TiO₂/BiVO₄ hybrid as an efficient photoelectrochemical platform for sensitive detection of soluble CD44 proteins. *Biosens. Bioelectron.* **2020**, *166*, 112439. [[CrossRef](#)] [[PubMed](#)]
69. Li, Y.; Mei, Q.; Liu, Z.; Hu, X.; Zhou, Z.; Huang, J.; Bai, B.; Liu, H.; Ding, F.; Wang, Q. Fluorine-doped iron oxyhydroxide cocatalyst: Promotion on the WO₃ photoanode conducted photoelectrochemical water splitting. *Appl. Catal. B Environ.* **2022**, *304*, 120995. [[CrossRef](#)]
70. Tian, Z.; Zhang, P.; Qin, P.; Sun, D.; Zhang, S.; Guo, X.; Zhao, W.; Zhao, D.; Huang, F. Novel black BiVO₄/TiO_{2-x} photoanode with enhanced photon absorption and charge separation for efficient and stable solar water splitting. *Adv. Energy Mater.* **2019**, *9*, 1901287. [[CrossRef](#)]
71. Liu, J.; Chen, W.; Sun, Q.; Zhang, Y.; Li, X.; Wang, J.; Wang, C.; Yu, Y.; Wang, L.; Yu, X. Oxygen vacancies enhanced WO₃/BiVO₄ photoanodes modified by cobalt phosphate for efficient photoelectrochemical water splitting. *ACS Appl. Energy Mater.* **2022**, *4*, 2864–2872. [[CrossRef](#)]
72. Liu, Y.; Xiao, X.; Liu, X.; Cui, L.L.; Gong, Y. Aluminium vanadate with unsaturated coordinated V centers and oxygen vacancies: Surface migration and partial phase transformation mechanism in high performance zinc-ion batteries. *J. Mater. Chem. A* **2021**, *10*, 912–927. [[CrossRef](#)]
73. Kang, H.; Ko, M.; Choi, H.; Lee, W.; Singh, R.; Kumar, M.; Seo, H. Surface hydrogenation of vanadium dioxide nanobeam to manipulate insulator-to-metal transition using hydrogen plasma. *J. Asian Ceram. Soc.* **2021**, *9*, 1310–1319. [[CrossRef](#)]

74. Bian, B.; Shi, L.; Katuri, K.P.; Xu, J.; Wang, P.; Saikaly, P.E. Efficient solar-to-acetate conversion from CO₂ through microbial electrosynthesis coupled with stable photoanode. *Appl. Energy* **2020**, *278*, 115684. [[CrossRef](#)]
75. Duan, Z.; Zhao, X.; Chen, L. BiVO₄/Cu_{0.4}V₂O₅ composites as a novel Z-scheme photocatalyst for visible-light-driven CO₂ conversion. *J. Environ. Chem. Eng.* **2021**, *9*, 104628. [[CrossRef](#)]
76. Wang, L.J.; Bai, J.Y.; Zhang, Y.J.; Mao, F.; Liu, Y.; Yuan, H.; Liu, P.F.; Yang, H.G. Controllable synthesis of conical BiVO₄ for photocatalytic water oxidation. *J. Mater. Chem. A* **2020**, *8*, 2331–2335. [[CrossRef](#)]
77. Yang, Z.; Saeki, D.; Takagi, R.; Matsuyama, H. Improved anti-biofouling performance of polyamide reverse osmosis membranes modified with a polyampholyte with effective carboxyl anion and quaternary ammonium cation ratio. *J. Membr. Sci.* **2021**, *595*, 117529. [[CrossRef](#)]
78. Li, Y.; Li, X.; Wang, X.-T.; Jian, L.-J.; Abdallah, N.I.M.; Dong, X.-F.; Wang, C.-W. P-n Heterostructured design of decahedral NiS/BiVO₄ with efficient charge separation for enhanced photodegradation of organic dyes. *Colloids Surf. A Physicochem. Eng. Asp.* **2021**, *608*, 125565. [[CrossRef](#)]
79. Qiao, X.; Xu, Y.; Yang, K.; Li, C.; Wang, H.; Jia, L. Laser-generated BiVO₄ colloidal particles with tailoring size and native oxygen defect for highly efficient gas sensing. *J. Hazard. Mater.* **2020**, *392*, 122471. [[CrossRef](#)]
80. Zhou, T.; Wang, J.; Zhang, Y.; Zhou, C.; Bai, J.; Li, J.; Zhou, B. Oxygen vacancy-abundant carbon quantum dots as superfast hole transport channel for vastly improving surface charge transfer efficiency of BiVO₄ photoanode. *Chem. Eng. J.* **2022**, *431*, 133414. [[CrossRef](#)]
81. Li, Y.; Liu, T.; Cheng, Z.; Peng, Y.; Yang, S.; Zhang, Y. Facile synthesis of high crystallinity and oxygen vacancies rich bismuth oxybromide upconversion nanosheets by air-annealing for UV–Vis–NIR broad spectrum driven Bisphenol A degradation. *Chem. Eng. J.* **2021**, *421*, 127868. [[CrossRef](#)]
82. Prathvi; Bhandarkar, S.A.; Kompa, A.; Kekuda, D.; Murari, M.S.; Telenkov, M.P.; Nagraja, K.K.; Mohan Rao, K. Spectroscopic, structural and morphological properties of spin coated Zn:TiO₂ thin films. *Surf. Interfaces* **2021**, *23*, 100910. [[CrossRef](#)]
83. Ye, S.; Xu, Y.; Huang, L.; Lai, W.; Deng, L.; Lin, Z.; Peng, H.; Zhou, X.; Xie, G. MWCNT/BiVO₄ photocatalyst for inactivation performance and mechanism of *Shigella flexneri* HL, antibiotic-resistant pathogen. *Chem. Eng. J.* **2021**, *424*, 130415. [[CrossRef](#)]
84. Liang, M.; Zhang, J.; Ramalingam, K.; Wei, Q.; Hui, K.S.; Aung, S.H.; Hui, K.N.; Chen, F. Stable and efficient self-sustained photoelectrochemical desalination based on CdS QDs/BiVO₄ heterostructure. *Chem. Eng. J.* **2022**, *429*, 132168. [[CrossRef](#)]
85. Mansour, S.; Akkari, R.; Ben Chaabene, S.; Saïd Zina, M. Effect of surface site defects on photocatalytic properties of BiVO₄/TiO₂ heterojunction for enhanced methylene blue degradation. *Adv. Mater. Sci. Eng.* **2020**, *2020*, 6505301. [[CrossRef](#)]
86. Wang, W.; Strohschein, P.J.; Lee, D.; Zhou, C.; Kawasaki, J.K.; Choi, K.S.; Liu, M.; Galli, G. The role of surface oxygen vacancies in BiVO₄. *Chem. Mater.* **2020**, *32*, 2899–2909. [[CrossRef](#)]
87. Xu, X.; Xu, Y.; Xu, F.; Jiang, G.; Jian, J.; Yu, H.; Zhang, E.; Shchukin, D.; Kaskel, S.; Wang, H. Black BiVO₄: Size tailored synthesis, rich oxygen vacancies, and sodium storage performance. *J. Mater. Chem. A* **2020**, *8*, 1636–1645. [[CrossRef](#)]
88. Pan, J.; Wang, B.H.; Wang, J.B.; Ding, H.Z.; Zhou, W.; Liu, X.; Zhang, J.R.; Guo, J.K.; Jiang, L.L.; Yin, S.F. Activity and stability boosting of oxygen-vacancy-rich BiVO₄ photoanode by NiFe-MOFs thin layer for water oxidation. *Angew. Chem. Int. Ed.* **2021**, *60*, 1433–1440. [[CrossRef](#)]
89. Han, Q.; Wu, C.; Jiao, H.; Xu, R.; Wang, Y.; Xie, J.; Guo, Q.; Tang, J. Rational design of high-concentration Ti³⁺ in porous carbon-doped TiO₂ nanosheets for efficient photocatalytic ammonia synthesis. *Adv. Mater.* **2021**, *33*, 2008180. [[CrossRef](#)]
90. Chen, Q.; Wang, H.; Wang, C.; Guan, R.; Duan, R.; Fang, Y.; Hu, X. Activation of molecular oxygen in selectively photocatalytic organic conversion upon defective TiO₂ nanosheets with boosted separation of charge carriers. *Appl. Catal. B Environ.* **2020**, *262*, 118258. [[CrossRef](#)]
91. Tu, L.; Hou, Y.; Yuan, G.; Yu, Z.; Qin, S.; Yan, Y.; Zhu, H.; Lin, H.; Chen, Y.; Wang, S. Bio-photoelectrochemical system constructed with BiVO₄/RGO photocathode for 2,4-dichlorophenol degradation: BiVO₄/RGO optimization, degradation performance and mechanism. *J. Hazard. Mater.* **2020**, *389*, 121917. [[CrossRef](#)] [[PubMed](#)]
92. Gomes, L.E.; Nogueira, A.C.; da Silva, M.F.; Praça, L.F.; Maia, L.J.Q.; Gonçalves, R.V.; Ullah, S.; Khan, S.; Wender, H. Enhanced photocatalytic activity of BiVO₄/Pt/PtO_x photocatalyst: The role of Pt oxidation state. *Appl. Surf. Sci.* **2021**, *567*, 150773. [[CrossRef](#)]
93. Tran-Phu, T.; Fusco, Z.; Di Bernardo, I.; Lipton-Duffin, J.; Toe, C.Y.; Daiyan, R.; Gengenbach, T.; Lin, C.-H.; Bo, R.; Nguyen, H.T.; et al. Understanding the Role of Vanadium Vacancies in BiVO₄ for Efficient Photoelectrochemical Water Oxidation. *Chem. Mater.* **2021**, *33*, 3553–3565. [[CrossRef](#)]
94. Xu, J.; Bian, Z.; Xin, X.; Chen, A.; Wang, H. Size dependence of nanosheet BiVO₄ with oxygen vacancies and exposed {0 0 1} facets on the photodegradation of oxytetracycline. *Chem. Eng. J.* **2018**, *337*, 684–696. [[CrossRef](#)]
95. Hafeez, H.Y.; Lakhera, S.K.; Ashokkumar, M.; Neppolian, B. Ultrasound assisted synthesis of reduced graphene oxide (rGO) supported InVO₄-TiO₂ nanocomposite for efficient hydrogen production. *Ultrason. Sonochem.* **2019**, *53*, 1–10. [[CrossRef](#)] [[PubMed](#)]
96. Shao, Z.-F.; Yang, Y.-Q.; Liu, S.-T.; Wang, Q. Transient competition between photocatalysis and carrier recombination in TiO₂ nanotube film loaded with Au nanoparticles. *Chin. Phys. B* **2014**, *23*, 096102. [[CrossRef](#)]
97. Lamers, M.; Fiechter, S.; Friedrich, D.; Abdi, F.F.; van de Krol, R. Formation and suppression of defects during heat treatment of BiVO₄ photoanodes for solar water splitting. *J. Mater. Chem. A* **2018**, *6*, 18694–18700. [[CrossRef](#)]
98. Wang, S.; Wang, X.; Liu, B.; Guo, Z.; Ostrikov, K.; Wang, L.; Huang, W. Vacancy defect engineering of BiVO₄ photoanodes for photoelectrochemical water splitting. *Nanoscale* **2021**, *13*, 17989–18009. [[CrossRef](#)] [[PubMed](#)]

99. Che, G.; Wang, D.; Wang, C.; Yu, F.; Li, D.; Suzuki, N.; Terashima, C.; Fujishima, A.; Liu, Y.; Zhang, X. Solution plasma boosts facet-dependent photoactivity of decahedral BiVO₄. *Chem. Eng. J.* **2020**, *397*, 125381. [[CrossRef](#)]
100. Arenas-Hernandez, A.; Zúñiga-Islas, C.; Torres-Jacome, A.; Mendoza-Cervantes, J.C. Self-organized and self-assembled TiO₂ nanosheets and nanobowls on TiO₂ nanocavities by electrochemical anodization and their properties. *Nano Express* **2020**, *1*, 010054. [[CrossRef](#)]
101. Zhou, C.; Sanders-Bellis, Z.; Smart, T.J.; Zhang, W.; Zhang, L.; Ping, Y.; Liu, M. Interstitial Lithium Doping in BiVO₄ Thin Film Photoanode for Enhanced Solar Water Splitting Activity. *Chem. Mater.* **2020**, *32*, 6401–6409. [[CrossRef](#)]
102. Peng, Y.; Du, M.; Zou, X.; Jia, G.; Permatasari Santoso, S.; Peng, X.; Niu, W.; Yuan, M.; Hsu, H.-Y. Suppressing photoinduced charge recombination at the BiVO₄/NiOOH junction by sandwiching an oxygen vacancy layer for efficient photoelectrochemical water oxidation. *J. Colloid Interface Sci.* **2022**, *608*, 1116–1125. [[CrossRef](#)]
103. Lin, X.; Xia, S.; Zhang, L.; Zhang, Y.; Sun, S.; Chen, Y.; Chen, S.; Ding, B.; Yu, J.; Yan, J. Fabrication of flexible mesoporous black Nb₂O₅ nanofiber films for visible-light-driven photocatalytic CO₂ reduction into CH₄. *Adv. Mater.* **2022**, *34*, 2200756. [[CrossRef](#)] [[PubMed](#)]
104. Sun, F.; Qi, H.; Xie, Y.; Xu, D.; Yu, W.; Ma, Q.; Yang, Y.; Yu, H.; Dong, X. Self-standing Janus nanofiber heterostructure photocatalyst with hydrogen production and degradation of methylene blue. *J. Am. Ceram. Soc.* **2022**, *105*, 1428–1441. [[CrossRef](#)]
105. Sadeghzadeh-Attar, A. Boosting the photocatalytic ability of hybrid BiVO₄-TiO₂ heterostructure nanocomposites for H₂ production by reduced graphene oxide (rGO). *J. Taiwan Inst. Chem. Eng.* **2020**, *111*, 325–336. [[CrossRef](#)]
106. Zheng, X.; Li, Y.; You, W.; Lei, G.; Cao, Y.; Zhang, Y.; Jiang, L. Construction of Fe-doped TiO_{2-x} ultrathin nanosheets with rich oxygen vacancies for highly efficient oxidation of H₂S. *Chem. Eng. J.* **2022**, *430*, 132917. [[CrossRef](#)]
107. Ghobadi, T.G.U.; Ghobadi, A.; Soydan, M.C.; Vishlaghi, M.B.; Kaya, S.; Karadas, F.; Ozbay, E. Strong Light-Matter Interactions in Au Plasmonic Nanoantennas Coupled with Prussian Blue Catalyst on BiVO₄ for Photoelectrochemical Water Splitting. *ChemSusChem* **2020**, *13*, 2577–2588. [[CrossRef](#)] [[PubMed](#)]
108. Chen, F.-Y.; Zhang, X.; Tang, Y.-B.; Wang, X.-G.; Shu, K.-K. Facile and rapid synthesis of a novel spindle-like heterojunction BiVO₄ showing enhanced visible-light-driven photoactivity. *RSC Adv.* **2020**, *10*, 5234–5240. [[CrossRef](#)] [[PubMed](#)]
109. Zhang, W.; Wang, Y.; Wang, Y.; Liang, Y.; Dong, F. Highly efficient photocatalytic NO removal and in situ DRIFTS investigation on SrSn(OH)₆. *Chin. Chem. Lett.* **2022**, *33*, 1259–1262. [[CrossRef](#)]
110. Dai, D.; Liang, X.; Zhang, B.; Wang, Y.; Wu, Q.; Bao, X.; Wang, Z.; Zheng, Z.; Cheng, H.; Dai, Y.; et al. Strain Adjustment Realizes the Photocatalytic Overall Water Splitting on Tetragonal Zircon BiVO₄. *Adv. Sci.* **2022**, *9*, 2105299. [[CrossRef](#)] [[PubMed](#)]
111. Wang, S.; He, T.; Chen, P.; Du, A.; Ostrikov, K.; Huang, W.; Wang, L. In Situ Formation of Oxygen Vacancies Achieving Near-Complete Charge Separation in Planar BiVO₄ Photoanodes. *Adv. Mater.* **2020**, *32*, 2001385. [[CrossRef](#)]
112. Zhao, W.; Zhang, J.; Zhu, F.; Mu, F.; Zhang, L.; Dai, B.; Xu, J.; Zhu, A.; Sun, C.; Leung, D.Y.C. Study the photocatalytic mechanism of the novel Ag/p-Ag₂O/n-BiVO₄ plasmonic photocatalyst for the simultaneous removal of BPA and chromium(VI). *Chem. Eng. J.* **2019**, *361*, 1352–1362. [[CrossRef](#)]
113. Wang, S.; Zhu, J.; Li, T.; Ge, F.; Zhang, Z.; Zhu, R.; Xie, H.; Xu, Y. Oxygen vacancy-mediated CuCoFe/Tartrate-LDH catalyst directly activates oxygen to produce superoxide radicals: Transformation of active species and implication for nitrobenzene Degradation. *Environ. Sci. Technol.* **2022**, *56*, 7924–7934. [[CrossRef](#)]
114. Prasad, U.; Young, J.L.; Johnson, J.C.; McGott, D.L.; Gu, H.; Garfunkel, E.; Kannan, A.M. Enhancing interfacial charge transfer in a WO₃/BiVO₄ photoanode heterojunction through gallium and tungsten co-doping and a sulfur modified Bi₂O₃ interfacial layer. *J. Mater. Chem. A* **2021**, *9*, 16137–16149. [[CrossRef](#)]
115. Zhu, J.; Liu, Y.; He, B.; Zhang, W.; Cui, L.; Wang, S.; Chen, H.; Duan, Y.; Tang, Q. Efficient interface engineering of N,N'-Dicyclohexylcarbodiimide for stable HTMs-free CsPbBr₃ perovskite solar cells with 10.16%-efficiency. *Chem. Eng. J.* **2022**, *428*, 131950. [[CrossRef](#)]
116. Gaikwad, M.A.; Suryawanshi, U.P.; Ghorpade, U.V.; Jang, J.S.; Suryawanshi, M.P.; Kim, J.H. Emerging surface, bulk, and interface engineering strategies on BiVO₄ for photoelectrochemical water splitting. *Small* **2022**, *18*, 2105084. [[CrossRef](#)] [[PubMed](#)]
117. Xu, M.; Zhu, Y.; Yang, J.; Li, W.; Sun, C.; Cui, Y.; Liu, L.; Zhao, H.; Liang, B. Enhanced interfacial electronic transfer of BiVO₄ coupled with 2D g-C₃N₄ for visible-light photocatalytic performance. *J. Am. Ceram. Soc.* **2021**, *104*, 3004–3018. [[CrossRef](#)]
118. Vinothkumar, K.; Jyothi, M.S.; Lavanya, C.; Sakar, M.; Valiyaveetil, S.; Balakrishna, R.G. Strongly co-ordinated MOF-PSF matrix for selective adsorption, separation and photodegradation of dyes. *Chem. Eng. J.* **2022**, *428*, 132561. [[CrossRef](#)]
119. Zheng, Y.; Wang, L.; Zhang, L.; Zhang, H.; Zhu, W. One-pot hydrothermal synthesis of hierarchical porous manganese silicate microspheres as excellent Fenton-like catalysts for organic dyes degradation. *Nano Res.* **2021**, *15*, 2977–2986. [[CrossRef](#)]
120. Feng, S.; Gong, S.; Zheng, Z.; Feng, G. Smart dual-response probe reveals an increase of GSH level and viscosity in Cisplatin-induced apoptosis and provides dual-channel imaging for tumor. *Sens. Actuators B Chem.* **2022**, *351*, 130940. [[CrossRef](#)]
121. Chen, M.; Wu, L.; Ye, H.; Liang, N.; Zhao, L. Biocompatible BSA-AuNP@ZnCo₂O₄ nanosheets with oxidase-like activity: Colorimetric biosensing and antitumor activity. *Microchem. J.* **2022**, *175*, 107208. [[CrossRef](#)]
122. Tang, W.; An, Y.; Chen, J.; Row, K.H. Multienzyme mimetic activities of holey CuPd@H-C₃N₄ for visual colorimetric and ultrasensitive fluorometric discriminative detection of glutathione and glucose in physiological fluids. *Talanta* **2022**, *241*, 123221. [[CrossRef](#)] [[PubMed](#)]
123. Liu, D.; Bai, X.; Sun, J.; Zhao, D.; Hong, C.; Jia, N. Hollow In₂O₃/In₂S₃ nanocolumn-assisted molecularly imprinted photoelectrochemical sensor for glutathione detection. *Sens. Actuators B Chem.* **2022**, *359*, 131542. [[CrossRef](#)]

124. Sohal, N.; Maity, B.; Basu, S. Morphology Effect of One-Dimensional MnO₂ Nanostructures on Heteroatom-Doped Carbon Dot-Based Biosensors for Selective Detection of Glutathione. *ACS Appl. Bio Mater.* **2022**, *5*, 2355–2364. [[CrossRef](#)] [[PubMed](#)]
125. Wang, M.; Zhan, Y.; Wang, H.; Zhang, C.; Li, G.; Zou, L. A photoelectrochemical sensor for glutathione based on Bi₂S₃-modified TiO₂ nanotube arrays. *New J. Chem.* **2022**, *46*, 8162–8170. [[CrossRef](#)]
126. Cai, L.X.; Miao, G.Y.; Li, G.; Chen, L.; Meng, F.L.; Guo, Z. A temperature-modulated gas sensor based on CdO-decorated porous ZnO Nanobelts for the recognizable detection of ethanol, propanol, and isopropanol. *IEEE Sens. J.* **2021**, *21*, 25590–25596. [[CrossRef](#)]